High-Latitude Over-the-Horizon Radar Applications

By

Timothy E. Theurer, B.S., M.S.

A Dissertation Submitted in Partial Fulfillment of the Requirements

for the Degree of

Doctor of Philosophy

in

Engineering

University of Alaska Fairbanks

May 2020

APPROVED:

Dr. William Bristow, Committee Chair
Dr. Denise Thorsen, Committee Member
Dr. Joseph Hawkins, Committee Member
Dr. Brenton Watkins, Committee Member
Dr. Richard Wies, Chair
    Department of Computer & Electrical Engineering
Dr. William Schnabel, Dean
    College of Engineering & Mines
Dr. Michael Castellini, *Dean of the Graduate School*

Abstract

Over-the-horizon radar (OTHR) systems that operate at high-latitudes often must contend with multipath and pronounced diffusive scattering effects produced by the anisotropic, birefringent, and heterogeneous nature of the ionosphere. In this thesis, radar performance at high-latitudes is quantified and several applications for either mitigating the deleterious effects of multipath and diffusive scattering or deriving information about the state of the ionosphere are proposed. The first application is inspired by adaptive optics techniques in other fields and involves the coherent summation of the received plane wave spectrum in order to improve angular resolution and array gain. The second application involves deriving ionospheric $\vec{E} \times \vec{B}$ drift from applying spatial correlation analysis to ground clutter echoes. The third application is the development of a new spatial adaptive processing technique designed specifically to preserve the Doppler spectrum of angle-Doppler coupled clutter like that observed at high-latitudes.

Table of Contents

List of Tables

Acknowledgments

1   Introduction

High-frequency (HF) over-the-horizon-radar (OTHR) systems use the ionosphere as a reflecting layer to illuminate targets beyond the geometric horizon [*Skolnik*, 2008]. As illustrated in the ray trace diagram in Figure 1.1, an OTHR radiates an angular spectrum of plane waves that enter the ionosphere at oblique angles, are continuously refracted within the ionosphere, and exit at angles approximated by Snell's law. Although dependent on design and operating frequency, an OTHR typically illuminates ranges from 1000-3000 km and an azimuth sector anywhere from $60° - 360°$ which provides a total coverage area on the order of millions of square kilometers [*Fabrizio*, 2013]. However, the advantage in coverage area that OTHR enjoys over line-of-sight (LOS) radars operating at higher frequency bands comes with a number of challenges introduced by the propagation medium itself.
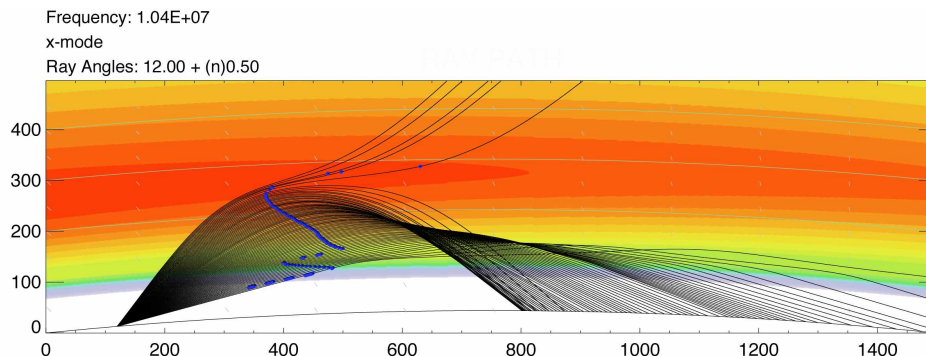
Figure 1.1: Ray trajectories through a hypothetical ionosphere.

The ionosphere is a birefringent, anisotropic, and heterogeneous propagation medium. Each of these characteristics is evident in the Appleton-Hartree expression for the index of refraction in a cold, collisionless plasma given by [*Budden*, 1985],

$$n^2 = 1 - \frac{X}{1 - \frac{Y^2 \sin^2\theta}{2(1-X)} \pm \left[\frac{Y^4\sin^4\theta}{4(1-X)^2} + Y^2\cos^2\theta\right]^2} \tag{1.1}$$

where each of the parameters in (1.1) is given in turn by,

$$X = \frac{\omega_0^2}{\omega^2}$$
$$Y = \frac{\omega_H^2}{\omega^2}$$
$$\omega_0 = \sqrt{\frac{Ne^2}{\epsilon_0 m}}$$
$$\omega_H = \frac{B_0|e|}{m}$$
$$\cos\theta = \vec{k} \cdot \vec{B}_0 \qquad (1.2)$$

In (1.2) ω is the wave frequency, ω_0 and ω_H are referred to as the electron plasma frequency and electron gyro frequency respectively, and θ is the angle between the Earth's background magnetic field $\vec{B}_0$ and the wave vector $\vec{k}$. The plasma frequency ω_0 depends on electron density N in addition to the physical constants of electron charge e, electron mass m, and free space permittivity ϵ_0. The gyro frequency ω_H depends on magnetic field strength $B_0 = |\vec{B}_0|$ in addition to electron charge and mass. The birefringent characteristic of the ionosphere is evident in the presence of two solutions to (1.1) as indicated by the ($\pm$) operator in the denominator. The solution corresponding to the ($+$) sign in (1.1) is termed the ordinary mode while the solution corresponding to the ($-$) is termed the extraordinary mode. In general, a plane wave of arbitrary polarization incident on the ionosphere can be expressed in terms of the ordinary and extraordinary modes each of which will refract differently through the ionosphere. The anisotropic nature of the ionosphere is manifest in the dependence of (1.1) on the angle θ between the wave vector $\vec{k}$ and the Earth's magnetic field $\vec{B}_0$. Finally, the heterogeneous property of the ionosphere can be seen from the dependence of (1.1) on electron density N through the plasma frequency ω_0. The electron density N is in general a function of position and time, i.e. $N = N(x, y, z, t)$ whose large scale variations are related to refractive effects and whose small scale variations produce diffractive effects [*Budden*, 1985].

The birefringent, anisotropic, and heterogeneous nature of the ionosphere produces two effects of concern to radar operators. These effects include multipath and diffuse scattering. Multipath is the presence of multiple propagation paths between a target and radar. In the ionosphere, multipath may exist due to the presence of reflections from multiple ionospheric layers, multiple reflections from a single layer, and the presence of ordinary and extraordinary modes. Diffuse scattering refers to the scattering of energy in the angular spectrum. Typically, radars operate under the assumption that the received echo from a target consists of a single plane wave whose wave vector $\vec{k}$ depends on the geometry between the radar and target. However, the heterogeneous nature of the ionosphere has the effect of spreading a single plane wave into a small number of plane waves that are closely resolved in angle. The net result of multipath and diffuse scattering is that the received signal consists of a time-varying spectrum of plane waves.

In this thesis we investigate the consequences of propagation in the high-latitude ionosphere for OTHR. The investigation results in the proposal of several applications for mitigating undesirable effects from a target detection standpoint as well as deriving information of interest about the state of the ionosphere. The first section of this thesis, Chapter 2, involves quantifying radar performance given a received target signal that consists of a time-varying spectrum of plane waves. Specifically, OTHR systems are often composed of antenna arrays and so the presence of a target signal that consists of a spectrum of plane waves rather than a single plane wave has significant ramifications for angular resolution and array gain. In addition, this section proposes a correction algorithm inspired by adaptive optics techniques in other fields for the coherent summation of the received plane wave spectrum to improve angular resolution and achievable array gain. In Chapter 3 of this thesis the presence of angle-Doppler coupling in ground clutter echoes is investigated. Diffraction analysis is applied to demonstrate that the observed angle-Doppler coupling is the product of an ionospheric drift transverse to the look direction of the radar. A method of estimating the ionospheric drift from spatial correlation analysis is provided as well as experimental drift

measurements. Finally, in Chapter 4 a new spatial adaptive processing (SAP) technique is proposed. OTHR systems must be capable of detecting targets in an environment that contains radio frequency interference (RFI) from other users of the HF band in addition to high power clutter echoes due either to backscatter from the surface of the Earth or to Bragg scatter from ionospheric density irregularities. One approach to mitigating RFI and clutter is a cascaded approach of first eliminating RFI through SAP and subsequently mitigating clutter through Doppler processing. However, SAP must be applied in such a fashion that the clutter signal is not inadvertently smeared throughout the Doppler spectrum. The SAP method proposed in this thesis is designed to preserve the Doppler spectrum of angle-Doppler coupled clutter with characteristics based on measurements made in Chapter 3. Chapter 2 and Chapter 3 of this thesis have been published in *Radio Science* and Chapter 4 has been published in *IEEE Transactions on Aerospace and Electronic Systems*. Conclusions and topics for future work are presented in Chapter 5.

2 Scintillation Correction in Phased Array High-Frequency Radar

2.1 Introduction

The field of adaptive optics (AO) was originally developed to mitigate atmospheric turbulence induced optical distortion viewed by ground based telescopes [*Aubrun et al.*, 1987]. However, AO methods have since been applied to imaging in other fields such as ultrasonic [*Ng et al.*, 1997], retinal [*Liang et al.*, 1997], and radio [*Steinberg*, 1981] which face the same fundamental problem of correcting wavefront aberrations in the imaging system. In any imaging system, aberrations in the incident wavefront hamper the ability of the receive aperture to coherently combine the incoming signal or alternatively to angularly resolve the source of the signal.

In this paper we investigate the application of AO techniques to improving the performance of the Super Dual Auroral High Frequency Radar (SuperDARN) phased array system [*Greenwald et al.*, 1985]. Diffraction and scattering during propagation through the ionosphere results in wavefronts incident on the radar whose amplitude and phase fluctuate over the physical extent of the array. An example of this scintillation is illustrated in Figure (2.1), which compares the magnitude, phase, and angular spectrum of ideal and measured wavefronts across the 16 element array. The ideal curves in Figure (2.1) represent the expected response from a spherically radiating target in the far-field of the radar, i.e. a constant amplitude, linear phase plane wave whose angular spectrum is the spatial Fourier transform of the radar aperture. The measured wavefront in Figure (2.1) is from a pulse that has propagated approximately 1500 km between two SuperDARN radars via refraction through the F-region ionosphere. The effect of fluctuations in the measured amplitude and phase across the array in (a) and (b) is spreading in the angular spectrum in (c) as compared to the ideal case. Beyond the obvious reduction in angular resolution, the spreading in the angular spectrum reduces the peak value of the main lobe that is equivalent to the signal obtained after geometric beamforming at the given angle of incidence. As the amplitude

and phase perturbations across the array vary with time, beamforming yields a summation signal whose amplitude and phase also fluctuate. The scintillation in the beamformed signal is not the result of true fluctuations in intensity or phase of the wavefront illuminating the radar but due instead to variations in the phasors composing the weighted summation.
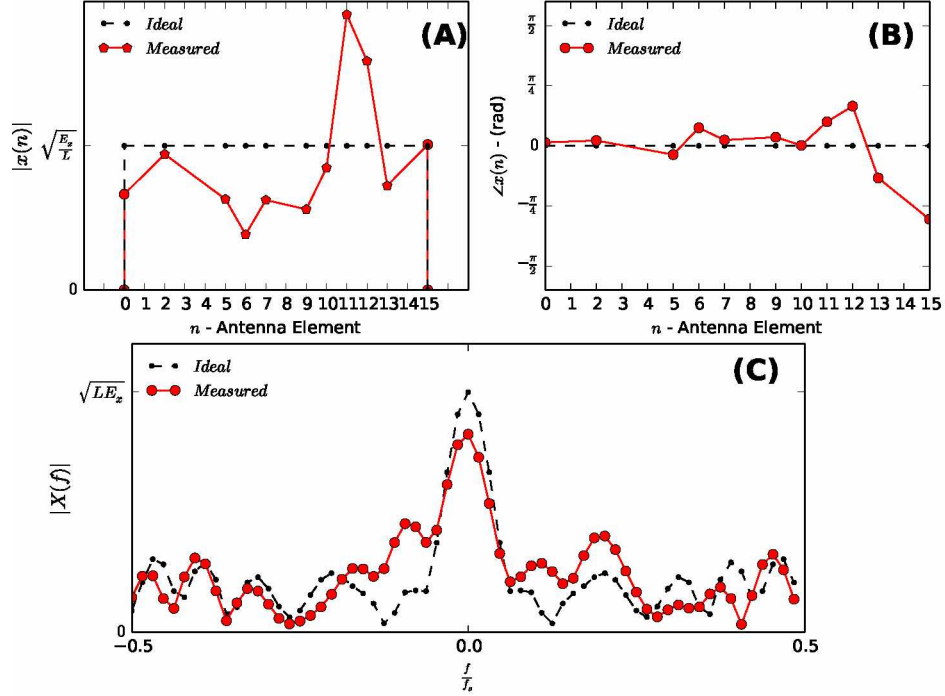
Figure 2.1: Comparison of (a) magnitude, (b) phase, and (c) angular spectrum of ideal and measured wavefront across the antenna array that illustrates scintillation. The angular spectrum in (c) is the $N = 128$ point zero-padded Fast-Fourier Transform (FFT) of the complex data in (a),(b) plotted as a function of normalized spatial frequency $\frac{f}{f_s}$ where $f_s = \frac{1}{\Delta x}$ and Δx is the antenna element spacing in meters.

The scintillation evident in Figure (2.1) is a product of the inhomogeneity in the ionosphere as the HF waves undergo diffraction and scattering during propagation [*Budden*, 1985]. These physical effects impose a limit on the length, l_{coh}, time, τ_{coh}, and bandwidth, f_{coh}, over which a propagating signal is correlated. For the ionosphere, analytical expressions have been derived [*Knepp*, 1983; *Nickisch*, 1992] and numerical simulations have been performed [*Nickisch and Franke*, 2001] to evaluate these coherence lengths which in general depend on the spatial electron density distribution, the HF wavelength, and the propaga-

tion distance. Finite l_{coh}, τ_{coh}, and f_{coh} may negatively impact radar performance through a number of mechanisms. Here specifically we are concerned with the case where l_{coh} is on the order of the array length and τ_{coh} is less than the coherent processing interval (CPI). In this situation, the amplitude and phase of wavefronts across the array are distorted and time-varying over the observation period. In addition, as the distortion of the wavefront is a function of the propagation path each range gate sampled is uniquely corrupted. Absent application of a corrective algorithm on a per range gate basis, the angular resolution and array gain achieved are reduced. Further, the beamformed signal will feature scintillation that is unrelated to true variations in intensity or phase of the incident wavefront but reflects rather variations in the distribution of the wavefront perturbations. However, provided that the perturbations across the array are slowly-varying, an adaptive AO algorithm can effectively correct and track the distorted wavefront at each range gate to approximate the theoretical radar performance.

In this paper, we begin by briefly describing the model of the received signal from a point target at the radar in the ideal case and in the case where scintillation produces a random phase profile across the array. The reduction in radar performance in terms of angular resolution and achievable array gain in the case of a random phase profile is quantified and compared to the ideal case which provides an upper bound on the performance of a correction algorithm. The implementation of an algorithm to compensate for slowly-varying scintillation effects is discussed. The algorithm presented is applied to data recorded by the Kodiak SuperDARN and improvement in radar performance is demonstrated.

2.2   Theory

The effect of scintillation is modeled here as the addition of a random phase at each antenna element in the radar aperture. The reduction in angular resolution and achievable array gain is quantified for the modeled scintillation and compared to the ideal case.

7

2.2.1 Signal Model

Let the normalized transmitted signal be expressed as,

$$s(t) = \sqrt{\frac{2}{E_g}} g(t) \cos(2\pi f_c t) \tag{2.1}$$

where $g(t)$ is the baseband waveform with energy E_g and f_c represents the carrier frequency.

Point targets in homogeneous media can be modeled as a linear, time-invariant (LTI) system with an impulse response so that the received signal is a scaled, delayed, and possibly frequency shifted version of (2.1),

$$
\begin{aligned}
r(t) &= K s(t - \tau) \\
&= K g(t - \tau) \cos(2\pi (f_c + f_d)(t - \tau)) \\
&= K g(t - \tau) \cos(2\pi (f_c + f_d)t + \phi)
\end{aligned}
\tag{2.2}
$$

In (2.2) K, τ, f_d, and ϕ represent respectively the amplitude, delay, Doppler frequency, and phase imposed on the transmitted signal by the channel. The complex lowpass representation of (2.2) is,

$$y(t) = K e^{j\phi} e^{j f_d t} g(t - \tau) \tag{2.3}$$

Given a one-dimensional linear array consisting of N elements, the lowpass waveform at the nth element of the array is related to the waveform at a reference element by,

$$y_n(t) = e^{jn\gamma} y(t) \tag{2.4}$$

where the phase factor γ is a function of incidence angle α, wavelength λ, and separation d between elements given by,

$$\gamma = \frac{2\pi d \sin(\alpha)}{\lambda} \tag{2.5}$$

The effect of propagation through an inhomogeneous medium is modeled here as the addition of a random phase profile across the radar aperture. Specifically, we assume that the form of the lowpass received waveform at a given antenna element is the same as in (2.3) but that the phase shift between elements is no longer given by the linear relationship in (2.4). Instead, the phase relationship across the array is modeled as a slowly-varying random process so that the lowpass signal at the nth element in the array is related to that at a reference element by,

$$y_n(t) = e^{j\phi_n} y(t) \tag{2.6}$$

where the random variable (RV) ϕ_n is a sample function of what we will assume is a stationary random process.

2.2.2   Radar Performance

The random phase ripple in the incident wavefront indicated by (2.6) hampers the ability of the radar to resolve a target in azimuth. Further, the ripple reduces the achieved array gain which depends on the coherent summation of the wavefront across the aperture. Here we will quantify the reduction in azimuth resolution by evaluating and comparing the Cramer-Rao Lower Bound (CRLB) for the ideal case and for a model of the random phase perturbations. The CRLB is a lower-bound on the variance of an unbiased estimator [*Peebles*, 1998] and is evaluated here to provide a benchmark for the improvement in azimuth resolution that may be obtained from a scintillation correction algorithm. In addition, the achievable array gain is evaluated for the modeled scintillation and is compared to the ideal case.

Azimuth Resolution

Note that a wavefront incident at an angle of α with respect to broadside produces a spatial frequency across the aperture given by,

$$\omega_s = \frac{\gamma}{d} = \frac{2\pi \sin(\alpha)}{\lambda} \tag{2.7}$$

9

The minimum variance in estimating ω_s given a vector of observation RV's $\hat{y} = y_0, \ldots, y_N$ dependent on ω_s is the CRLB given by [*Peebles*, 1998],

$$\sigma_{\omega_s}^2 = \frac{1}{-E\left[\frac{\partial^2 \ln\{p(\hat{y}|\omega_s)\}}{\partial \omega_s^2}\right]} \tag{2.8}$$

where $E[\cdot]$ denotes the statistical expectation, and $p(\hat{y}|\omega_s)$ is the probability of observing the set $\hat{y}$ given the spatial frequency ω_s. In the ideal case of a plane wave front across a linear array of N elements, each RV y_n has the form,

$$y_n = Ae^{j(\omega_s x_n + \phi)} + w_n \quad n = 0, \ldots, N-1 \tag{2.9}$$

where the x_n's are spaced by $\Delta x = \frac{L}{N}$. The quadrature components of 2.9 are,

$$y_n = \left(y_{ni} + w_{ni}\right) + j\left(y_{nq} + w_{nq}\right)$$

$$y_{ni} = A\cos(\omega_s x_n + \phi) + w_{ni}$$

$$y_{nq} = A\sin(\omega_s x_n + \phi) + w_{nq} \tag{2.10}$$

where w_{ni}, w_{nq} are the quadrature reciever thermal noise components each of variance σ_w^2. The joint probability density function (PDF) of the in-phase signal component conditioned on the spatial frequency ω_s is given by,

$$p(\hat{y}|\omega_s) = \prod_{n=0}^{N-1} \frac{1}{\sqrt{2\pi\sigma_w^2}} e^{\frac{-(y_{ni} - A\cos(\omega_s x_n + \phi))^2}{2\sigma_w^2}}$$

$$p(\hat{y}|\omega_s) = \frac{1}{\left(2\pi\sigma_w^2\right)^{\frac{N}{2}}} e^{\sum_{n=0}^{N-1} \frac{-(y_{ni} - A\cos(\omega_s x_n + \phi))^2}{2\sigma_w^2}} \tag{2.11}$$

From (2.11), the denominator of the CRLB can be reduced to:

$$-E\left[\frac{\partial^2 \ln\{p(\hat{y}|\omega_s)\}}{\partial \omega_s^2}\right] = \frac{A^2}{2\sigma_w^2}\left[\sum_{n=0}^{N-1} x_n^2 - \sum_{n=0}^{N-1} x_n^2 \cos(2\omega_s x_n + 2\phi)\right] \tag{2.12}$$

10

Assuming the summation over the double frequency component is small relative to the first term on the RHS of (2.12) and recognizing $\frac{A^2}{2\sigma_w^2}$ as the single antenna element SNR, the expression further simplifies to

$$-E\left[\frac{\partial^2 \ln\{p(\hat{y}|\omega_s)\}}{\partial \omega_s^2}\right] \quad = \text{SNR} \cdot \sum_{n=0}^{N-1} x_n^2$$

$$= \text{SNR} \cdot \sum_{n=0}^{N-1} ((n-\frac{N}{2})\Delta x)^2$$

$$= \text{SNR} \cdot \sum_{n=0}^{N-1} \left((n-\frac{N}{2})(\frac{L}{N})\right)^2$$

$$\simeq \text{SNR} \cdot \left(\frac{NL^2}{12}\right) \tag{2.13}$$

so that the variance in estimating spatial frequency is bounded by,

$$\sigma_{\omega_s}^2 \geq \frac{12}{\text{N} \cdot L^2 \cdot \text{SNR}} \tag{2.14}$$

Note from (2.14) that the CRLB is inversely proportional to the SNR, total aperture length, and the number of sample points in the aperture.

Now we are interested in evaluating the CRLB in the scintillated case modeled here as a random phase profile. The analytic signal at each point in the aperture is again given by (2.9) with the exception that the phase ϕ is now a random variable. For simplicity, assume each ϕ_n is an independent and identically distributed (IID) normal RV with zero mean and variance σ_ϕ^2. Ignoring the influence of thermal noise, the joint PDF of the in-phase signal component conditioned on ω_s can be found after several transformations [*Papoulis*, 1984] as,

$$p(\hat{y}|\omega_s) = \prod_{n=0}^{N-1} \frac{1}{\sqrt{2\pi\sigma_\phi^2}} \frac{2}{A\sqrt{1-\left(\frac{y_n}{A}\right)}} e^{\frac{-(\cos^{-1}\left(\frac{y_n}{A}\right)-\omega_s x_n)^2}{2\sigma_\phi^2}}$$

$$p(\hat{y}|\omega_s) = e^{-\sum_{n=0}^{N-1} \frac{(\cos^{-1}\left(\frac{y_n}{A}\right)-\omega_s x_n)^2}{2\sigma_\phi^2}} \prod_{n=0}^{N-1} \frac{1}{\sqrt{2\pi\sigma_\phi^2}} \frac{2}{A\sqrt{1-\left(\frac{y_n}{A}\right)}} \tag{2.15}$$

The denominator of the CRLB for (2.15) reduces to,

$$-E\left[\frac{\partial^2 \ln\{p(\hat{y}|\omega_s)\}}{\partial \omega_s^2}\right] = \frac{1}{\sigma_\phi^2}\sum_{n=0}^{N-1}x_n^2$$

$$-E\left[\frac{\partial^2 \ln\{p(\hat{y}|\omega_s)\}}{\partial \omega_s^2}\right] \simeq \frac{NL^2}{12\sigma_\phi^2} \qquad (2.16)$$

so that the CRLB in estimating spatial frequency is,

$$\sigma_{\omega_s}^2 \geq \frac{12\sigma_\phi^2}{N \cdot L^2} \qquad (2.17)$$

Similar to the result in (2.14), the obtained CRLB is inversely proportional to the aperture size and number of sample points. However, as a result of the random phase model and the neglect of thermal noise, the CRLB is independent of signal power and is instead proportional to the phase perturbation variance. The effect of including thermal noise would be a broadening in the width of the PDF given in (2.15) and a corresponding increase in uncertainty. The CRLB in this case would also be dependent on SNR. However, in the limiting case of infinite SNR we would arrive at (2.17).

The ratio of the scintillated CRLB in (2.17) to the ideal CRLB in (2.14) is $\sigma_\phi^2 \cdot \text{SNR}$. Assume a target with an SNR of 20 dB exists but that scintillation yields random phase perturbations in the wavefront with $\sigma_\phi = 20°$. The uncertainty in azimuth increases by a factor of $\left(\sigma_\phi^2 \cdot \text{SNR}\right) \simeq \left(0.12 \cdot 100\right) \simeq 12$ over the ideal case, clearly demonstrating the need for a correction algorithm.

Array Gain Factor

Ideally, a N element phased array yields an array gain factor of N due to the coherent addition of the desired signal versus the incoherent addition of receiver noise. The coherent

summation of the signal across the antenna array results in the instantaneous received power,

$$P = \left(\sum_{n=0}^{N-1} s_n + w_n \right)^2 \tag{2.18}$$

where s_n and w_n are the (complex) desired signal and noise at the nth receiver. Assuming thermal noise that is independent between receivers (2.18) reduces to,

$$P = \sum_{n=0}^{N-1} |s_n|^2 + \sum_{n=0}^{N-1} \sum_{m=0; m\neq n}^{N-1} s_n s_m^* + N\sigma_w^2 \tag{2.19}$$

In (2.19), the first and third terms are summations of the signal and noise powers across the array and the second term is the summation of the cross- correlated signal powers $s_n s_m^*$ between array elements. In the ideal case, beamforming yields a constant complex signal across the array so that $s_n = s_m = s$ and the sum of the first two terms in (2.19) yields the maximum possible signal power of $N^2 P_s$. If the incident wavefront contains phase aberrations, the complex numbers in the second term of (2.19) are not co-phased after beamforming and the summation of the second term yields a smaller value. The loss in array gain with respect to the ideal case is easily evaluated empirically as,

$$L_{array} = \left(NA \right)^2 - \left(\sum_{n=0}^{N-1} Ae^{j\phi_n} \right)^2 \tag{2.20}$$

given the distributions of the ϕ_n's. Figure (2.2) illustrates the empirically evaluated $E[L_{array}]$ versus σ_ϕ for IID normal ϕ_n's.

In addition to the loss in array gain that results from phase variations across the aperture, amplitude variations will also decrease the achievable array gain. Consider that the energy intercepted by a slit aperture can be expressed as,

$$\varepsilon_A = \int_0^L A^2(l)dl \tag{2.21}$$

13
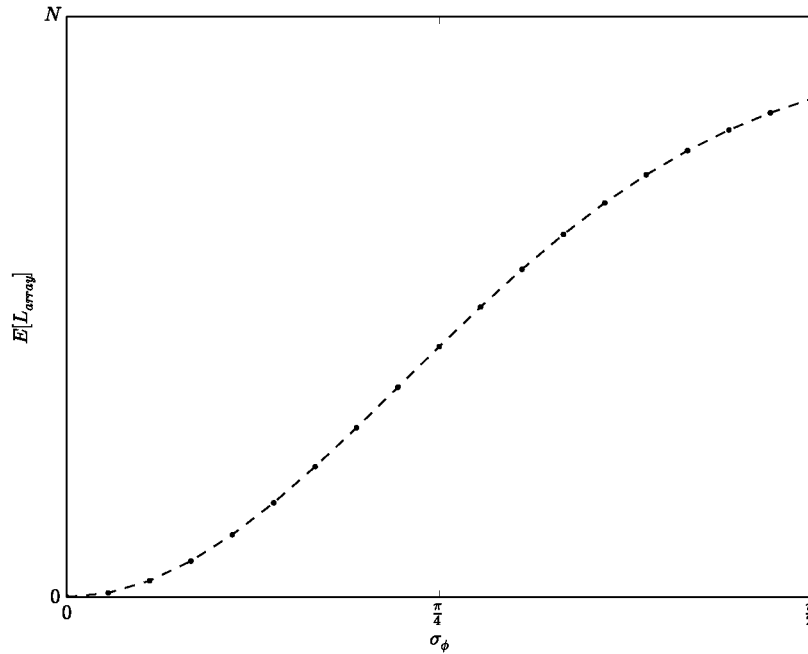
Figure 2.2: Empirically evaluated $E[L_{array}]$ versus σ_ϕ for IID normal ϕ_n's given $N = 16$ array elements.

where $A(l)$ represents the amplitude of the wavefront along the aperture. Ignoring phase variations, the summation of the wavefront along the aperture is,

$$A_c = \int_0^L A(l)dl \tag{2.22}$$

Variational calculus can be used to demonstrate that the maximum of (2.22) subject to the constraint that (2.21) remains constant occurs when $A(l)$ is constant across the aperture, i.e. when the wavefront appears as a plane wavefront as may be expected. Therefore, even when the aperture intercepts the same total energy ε_A, the amplitude of the beamformed signal is reduced in the presence of amplitude fluctuations in comparison to the ideal case.

Beyond the reduction in array gain discussed above, time variations in the wavefront disotortion will reduce the non-coherent integration gain obtained. In the case that $\tau_{coh} <$ CPI, the observed array gain G_A will fluctuate over the CPI. This implies that non-fluctuating targets (Swerling 0) with constant radar cross section (RCS) appears as fluctuating targets

14

(Swerling II/IV). Non-coherent integration gain depends on Swerling target type and can be approximated for a given point on a radar operating curve [*Shnidman*, 2002]. Although dependent on the exact point on the ROC, the minimum single sample SNR to achieve a given point on the ROC is typically obtained for Swerling 0 targets. Applied to our study, the correction algorithm should be capable of tracking changes in the wavefront distortion so that a non-fluctuating target actually appears non-fluctuating over the CPI.

Time, Range, Doppler Resolution

It is also worth noting that the improvement in SNR discussed above improves the resolution in time, range, and Doppler. Assuming that the signal is non-fluctuating over the observation period, the well known CRLB's for these resolutions are [*Peebles*, 1998],

$$\sigma_{t_0}^2 \geq \frac{1}{\text{SNR} \cdot B_{rms}^2} \tag{2.23}$$

$$\sigma_R^2 \geq \frac{c}{2\sqrt{\text{SNR}} \cdot B_{rms}} \tag{2.24}$$

$$\sigma_{\omega_d}^2 \geq \frac{1}{\text{SNR} \cdot \tau_{rms}^2} \tag{2.25}$$

where B_{rms} and τ_{rms} are the rms bandwidth and time duration of the transmitted signal.

2.3   Scintillation Correction Algorithm

Realizing the upper performance bounds presented in Section (2.2.2) requires correcting the amplitude and phase perturbations across the radar aperture for every sampled range gate. For a given range gate, co-phasing may be performed by applying a phase conjugate

filter to each antenna element. Given an array of N elements each filter is simply formed as,

$$h_{\phi,n} = e^{j(\phi_r - \phi_n)} = e^{j\Delta\phi_n} \qquad (2.26)$$

where ϕ_r is an arbitrary reference angle and ϕ_n is the angle of the element to be corrected. For a phased array radar with N antenna elements and M sampled range gates a total of (N x M) phase conjugate filters are required.

Note that application of (2.26) will force a flat phase response across the array which optimizes the angular resolution but translates the peak of the angular spectrum to zero. If we wish to optimize angular resolution but preserve the location of the peak in the angular spectrum, then the mean slope of the phase-conjugate filters in (2.26) should be removed as,

$$h_{\phi,n} = h_{\phi,n} e^{-jn\bar{\phi}} \qquad (2.27)$$

where $\bar{\phi}$ is the mean slope of the phase conjugate filters calculated in (2.26). Here, the mean slope of the phase conjugate filters is obtained from a least-squares linear fit to the unwrapped phase. Note that if the phase errors are large enough to produce an incorrect phase unnwrapping, the peak of the angular spectrum will still be translated.

Amplitude perturbations may be corrected by scaling the amplitude of the wavefront across the aperture to yield the maximum coherent summation subject to the constraint that the energy intercepted by the aperture remains constant. Suppose for a given range gate that the amplitude at the nth antenna element in the aperture is A_n and the total energy intercepted by the aperture is ε_A. The ideal amplitude at the nth element in the aperture that yields the same total energy across the aperture is $B_n = K_n A_n$ where scaling factor K_n is given by,

$$K_n = \sqrt{\frac{\varepsilon_A}{L}} \frac{1}{A_n} \qquad (2.28)$$

16

and L is the length of the slit aperture. The correction factor for the nth antenna element that compensates for both amplitude and phase distortion is,

$$h_n = K_n e^{j\Delta\phi_n} \qquad (2.29)$$

The amplitude and phase correction factors in (2.26) and (2.28) may be evaluated from the first pulse in a CPI. However, the wavefront distortion across the radar aperture will vary over the duration of the CPI. These changes may be tracked by applying the slow-time history of K_n and $\Delta\phi_n$ to a feedback loop. The conjugate filter for the nth antenna element during the mth pulse in a CPI may now be expressed as,

$$h_n(m) = \left(K_n(m) \star l_K(m)\right)e^{j\left(l_\phi(m)\star\Delta\phi_n(m)\right)} \qquad (2.30)$$

where $l_K(m)$ and $l_\phi(m)$ represent the impulse response of the feedback loops used to track amplitude and phase variations in the wavefront.

The amplitude and phase correction process described above is illustrated in the flow diagram depicted in Figure (2.3). In Figure (2.3), x_n denotes the slow-time analytic signal from a single antenna element and range gate, $L_{\phi,n}(s)$ and $L_{K,n}(s)$ represent the system transfer functions of the $\Delta\phi_n$ and K_n tracking loops, and h_n is the filter in (2.30) that performs amplitude and phase correction. Note that a phased array antenna system with N antenna elements and M sampled range gates requires (N X M) of the system blocks depicted in Figure (2.3) in order to correct range gate specific wavefront distortion across the array.

In this study we experimented with both standard second order tracking loops and linear predictive filtering for the tracking loops $L_{\phi/K}(s)$ depicted in Figure (2.3). A standard second order tracking loop has a transfer function of the form,

$$L_{\phi/K}(s) = \frac{1 + \tau_2 s}{1 + (\tau_2 + {}^1/_K)s + ({}^{\tau_1}/_K)s^2} \qquad (2.31)$$
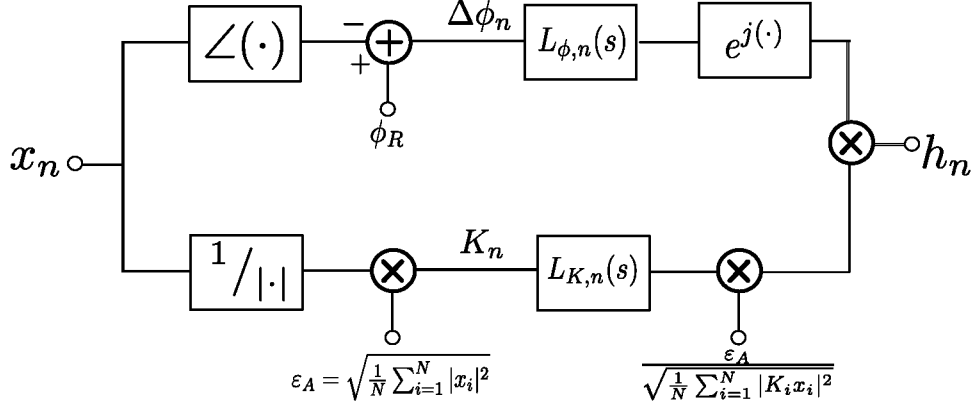
Figure 2.3: Flow diagram of wavefront correction for a single antenna element and range gate. Note that the multiplicative factors in the lower branch are required to conserve the total energy intercepted by the aperture when performing amplitude correction. For a system comprised of N antenna elements and M sampled range gates (N X M) such system blocks are required to correct range gate specific wavefront distortion across the aperture.

where $\tau_1 >> \tau_2$ [*Proakis and Salehi*, 2008]. The poles of (2.31) are controlled by the parameters K and τ_1 while the zero is controlled by τ_2 and these parameters may be varied to produce various levels of damping in the system response. A discrete IIR realization of (2.31) may be implemented by using a bilinear transformation [*Mitra*, 2010].

Linear predictive filtering is implemented here using 1-step ahead causal FIR Wiener filtering. Specifically, a Nth order linear predictive filter predicts the current sample of a discrete wide-sense-stationary (WSS) random process using a linear combination of the N most recent values [*Proakis and Salehi*, 2008]. By assuming the WSS process to be modeled is ergodic, the FIR filter tap coefficients may be found by solving the Yule-Walker equations from $N + 1$ samples of the autocorrelation of the input data sequence ($\Delta\phi_n$ or K_n) [*Proakis and Salehi*, 2008]. Predictive filtering was applied in this study by dividing the input data sequence x_n into non-overlapping frames of length L and re-evaluating the FIR tap coefficients for the tracking blocks $L_{\phi/K}(s)$ in Figure (2.3) every frame. The output response is given by re-assembling the frames using the overlap-add algorithm [*Mitra*, 2010].

Although our experimentation was limited, we found that a standard second order tracking loop generally gave comparable results to predictive filtering although the predictive filtering results were superior. The results presented here are generated using the linear pre-

dictive filtering algorithm we've described above but a more exhaustive study of optimizing the wavefront correction process has been planned for a future date.

2.4 Results

In the following section the experimental set-up and signal conditioning that was performed in this study will be detailed before presenting measurements of the observed scintillation and effect on radar performance. The performance of the scintillation correction algorithm in section (2.3) is then illustrated by comparing the measured scintillation and radar performance post-correction to the uncorrected data set.

2.4.1 Experimental Set-Up

The data set presented in this study was measured utilizing a SuperDARN radar located in Kodiak, Alaska ([57.62 N, 152.19 W]) to listen to pulses transmitted from the back lobe of a SuperDARN radar located in Inuvik, Northwest Territories ([68.42 N, 133.5 W]). The radars are separated by ~ 1500 km so that the only viable propagation method is ionospheric refraction. The main lobe of the Inuvik radar was steered so that the bearing of the back lobe was $\sim 0.7°$ from boresight at Kodiak. In the dataset presented here, Inuvik transmitted a periodic pulse sequence containing 15 pulses with a pulse repetition frequency of 50 (Hz), a pulse width of 500 (μs), and a carrier frequency of 10.5 (MHz) that was continuously re-triggered for a 15 (s) observation interval. During an observation interval, the Kodiak radar was configured to listen at the transmit frequency, recording raw sample files of length 50 (ms) consisting of the in-phase and quadrature signal at each antenna element in the 16-element array sampled in 100 (μs) steps. An 80 (ms) latency is incurred between writing raw sample files so that only ~ 120 files are recorded during a single ~ 15 second observation interval. The data presented in this study consists of five 15 (s) observation intervals recorded at the end of each minute during the period 2014/10/30 14:00:00-14:05:00 UT.

2.4.2 Signal Conditioning

The radars at Inuvik and Kodiak are not time synchronized with respect to each other and the Inuvik radar drifts in time with respect to UT. The lack of time synchronization meant the phase of the received pulses varied between raw sample files over an observation interval. The signal across the array from each received pulse was referenced to zero phase by first removing the linear phase profile due to the incidence angle of 0.7° using (2.5) and then subtracting the angle of the phasor summation $\sum_0^{N-1} e^{j\phi_n}$.

In addition to referencing each received pulse to a zero reference phase, care was taken to eliminate amplitude variations between antenna elements due to differences in receiver gains. During 25 (ms) prior to each observation period, a Rayleigh distribution was fit to the amplitude distribution of noise at each antenna element. The noise power at each antenna element was determined from the mean, μ_A, of the fitted Rayleigh distribution as,

$$\sigma_w^2 = \frac{2}{\pi} \mu_A^2 \qquad (2.32)$$

and gain correction factors evaluated by taking the ratio of the measured σ_w^2 between a given element and a reference element. In doing this we have assumed that the external thermal and atmospheric noise is additive, white, and Gaussian (AWGN) and also much greater than the receivers internal noise referred to the input [*Carlson et al.*, 2002].

The result of the pre-processing performed in this study is a $[16, M]$ matrix of complex signal samples representing the received pulse across the array for the duration of an observation interval. Each sample of the wavefront across the array has been referenced to zero-phase and scaled to compensate for receiver gain variations. The number of samples M recorded at each antenna element is on the order of 180 with a time-spacing between consecutive samples in the range of $[20, 180]$ (ms).

2.4.3 Evidence of Scintillation

Before continuing, we provide evidence that the observed phase and amplitude error distributions are broader than what would be expected from AWGN at the measured SNR levels with the conclusion that the increased width of the distributions results from scintillation. The distribution of phase fluctuations from all samples and antenna elements where the single element SNR was ≥ 15.0 (dB) is illustrated in Figure (2.4) (A). Also illustrated is the theoretical distribution of phase error for a constant phasor in AWGN which is given by,

$$p_\phi(\phi) = \frac{e^{-\frac{k^2}{2}}}{2\pi} + \frac{k\cos(\phi)}{\sqrt{2\pi}}e^{-\frac{k^2\sin^2(\phi)}{2}}\left[\frac{1}{\sqrt{2\pi}}\int_{-\infty}^{k\cos(\phi)}e^{-\frac{y^2}{2}}dy\right] \tag{2.33}$$

where k is the ratio of the constant phasor amplitude to noise amplitude equivalent to $\sqrt{SNR} \simeq 5.62$ in this case [$Goodman$, 1985]. Note that the measured distribution is substantially broader than that predicted for AWGN and a SNR of 15.0 (dB).

Amplitude scintillation is similarly demonstrated by first identifying all pulse samples where the SNR of the coherent summmation across the array is $\geq (15.0 + 10.\log_{10}(N)) = 27.0$ (dB). For this set of samples, the histogram of signal to noise amplitude $\frac{a}{\sigma_w}$ is illustrated in Figure (2.4) (B) and compared to the theoretical distribution of $\frac{a}{\sigma_w}$ for a constant phasor in AWGN which is given by,

$$\sigma_w p_A(a) = \frac{a}{\sigma_w}e^{-\frac{(\frac{a}{\sigma_w})^2+b^2}{2}}I_0(\frac{a}{\sigma_w}b) \tag{2.34}$$

where $b = \frac{s}{\sigma_w} = \sqrt{SNR} = 5.62$ and $I_0(\cdot)$ is the modified Bessel function of the first kind, zero-order [$Goodman$, 1985]. Again, the measured distribution is substantially broader than the predicted distribution for AWGN and a SNR of 15.0 (dB).
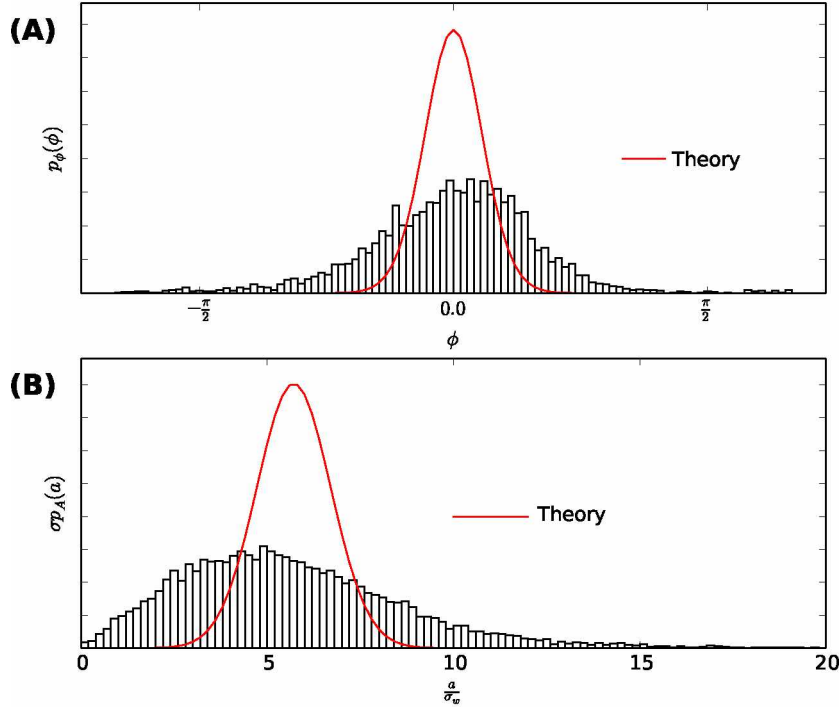
Figure 2.4: (A) Distribution of observed phase errors over all samples and antenna elements where the single element SNR was ≥ 15.0 (dB). (B) Distribution of $\frac{a}{\sigma_w}$ over all samples and antenna elements where the coherent summation SNR was $\geq (15.0 + 10 \cdot \log_{10}(N))$. The red curves in (A) and (B) illustrate the theoretical distributions of amplitude and phase of a constant phasor in the presence of AWGN alone. The broad width of the measured distributions in comparison to the theoretical curves provides evidence of scintillation.

2.4.4   Measured Scintillation & Performance Loss

The severity of the amplitude and phase fluctuations across the array were quantified during each observation interval by evaluating the amplitude scintillation index S_4 and phase standard deviation of the beamformed signal given by,

$$S_4 = \sqrt{\frac{E[A^4] - E[A^2]^2}{E[A^2]^2}} \tag{2.35}$$

and

$$\phi_{rms} = \sqrt{E[\phi^2] - E[\phi]^2} \tag{2.36}$$

Note that the beamformed signal was normalized by the energy in the wavefront ε_A as given in (2.21) to isolate amplitude fluctuations caused by wavefront distortion from those due to variations in the total power density illuminating the radar, i.e. to isolate diffractive effects from refractive effects. Figure (2.5) (A)-(C) depict a sample history of the SNR, normalized amplitude, and phase of the beamformed signal across one of the observation intervals. Scintillation is clearly illustrated during the interval by valleys in the signal amplitude history accompanied by large fluctuations in the phase history such as those near sample indices 10, 25, 50, 65, 80, 100, and 125. Annotated in Figure (2.5) (B) and (C) are the corresponding amplitude and phase scintillation metrics for the interval to provide the reader with a visual reference for these quantities.
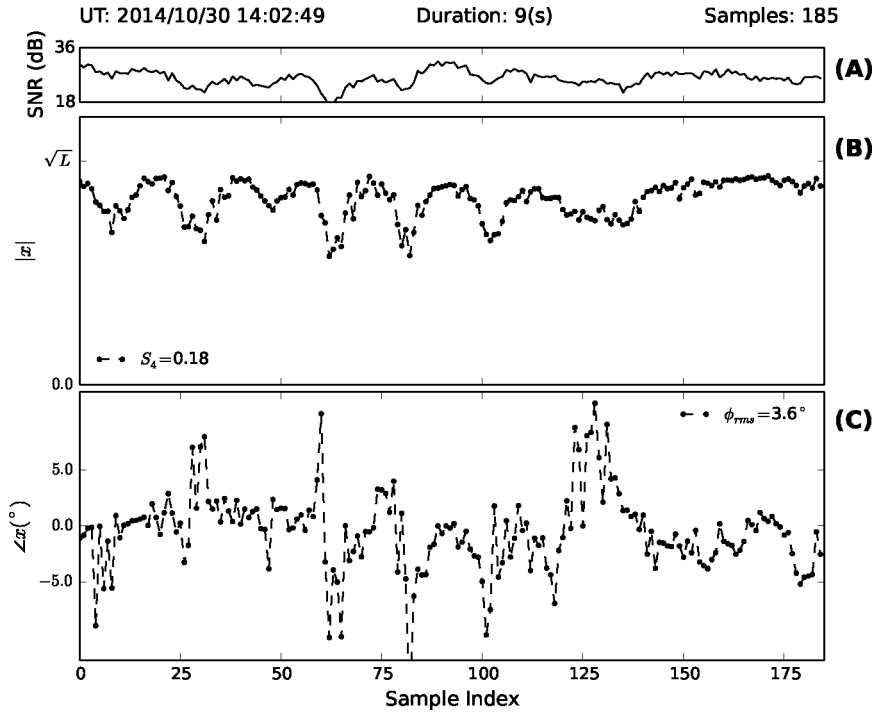
Figure 2.5: (A) SNR, (B) amplitude, (C) phase history of beamformed signal across array during given observation interval. Plot (B) generated by normalizing the signal amplitude by $\sqrt{\varepsilon_A}$ to isolate fluctuations due to wavefront distortion from fluctuations in power density illuminating the radar. Note $\sqrt{L}$ is the ideal amplitude achieved when coherently summing a unit-energy wavefront across a slit aperture of length L.

The effect of scintillation on radar performance was quantified by evaluating the un-

Period	S_4	$\phi_{rms}(°)$	$\dfrac{\sigma^2_{\omega_s - Obs}}{\sigma^2_{\omega_s - Ideal}}$	$E[L_{array}]$
1	0.33	8.22	3.50	1.09
2	0.19	9.52	20.69	0.87
3	0.19	3.63	22.32	0.83
4	0.51	9.45	29.69	1.68
5	0.35	8.07	12.61	1.41

Table 2.1: Scintillation metrics evaluated for each observation period

certainty in angular resolution with respect to the CRLB and the loss in array gain. The spatial frequency across the array was estimated from a least-squares linear fit for every sample in an observation interval. The uncertainty in the spatial frequency measurement was then quantified by comparing the variance $\sigma^2_{\omega_s}$ of the resulting distribution to the CRLB in (2.14). The expression in (2.14) was evaluated using the radar parameters and the mean single-element SNR during the given observation period. Loss in array gain due to wavefront distortion was evaluated for every sample in an observation interval as,

$$L_{array} = \frac{\sqrt{L\varepsilon_A}}{\left| \int_0^L A(l)e^{j\phi(l)}dl \right|} \qquad (2.37)$$

which is the amplitude ratio betweeen a coherently summed ideal plane wave and the actual beamformed signal.

Table (2.1) depicts the measured scintillation metrics for each of the five, 15 (s) observation intervals. The table illustrates that wavefront distortion results in amplitude scintillation that varies from weak ($S_4 < 0.3$) to moderate ($0.3 \leq S_4 < 0.6$) but phase scintillation that is consistently strong ($\phi_{rms} > 1°$). The scintillation results in angular resolution uncertainty that is on the order of a magnitude greater than the CRLB in the ideal case and a loss in array gain on the order of a decibel.

Period	S_4	$\phi_{rms}(°)$	$\frac{\sigma^2_{\omega_s-Obs}}{\sigma^2_{\omega_s-Ideal}}$	$E[L_{array}]$
1	0.15	2.97	1.17	0.22
2	0.13	2.17	4.69	0.16
3	0.04	1.20	2.16	0.04
4	0.10	3.28	2.12	0.16
5	0.16	3.46	4.22	0.25

Table 2.2: Post-correction scintillation metrics evaluated for each observation period.

2.4.5 Performance of Scintillation Correction Algorithm

A correction algorithm was implemented as discussed in section (2.3). The filters $l_\phi(m)$ and $l_K(m)$ used to track the variations in wavefront amplitude and phase at each antenna element were implemented as 2-tap linear predictive FIR filters and tap coefficients were re-evaluated every 4 samples in a given observation interval [*Proakis and Salehi*, 2008]. Further, improved results were obtained by pre-filtering the slow-time phase error history $\Delta\phi_n(m)$ using a first-order Butterworth lowpass filter. Figure (2.6) illustrates a comparison between the normalized amplitude and phase history of the uncorrected and corrected beamformed signals during the same observation interval depicted in Figure (2.5) with a reduction in scintillation clearly evident. Note in Figure (2.6) (B) that the width and depth of the valleys in the corrected amplitude history are substantially reduced in comparison to the uncorrected amplitude history and that some valleys in the uncorrected history such as those near samples 50 and 80 are no longer even discernible. Similarly, in Figure (2.6) (C) note that both the number and magnitude of significant phase fluctuations in the corrected phase history is significantly reduced in comparison to the uncorrected phase history. Table (2.2) depicts the scintillation metrics evaluated for the corrected wavefronts during each of the observation intervals.
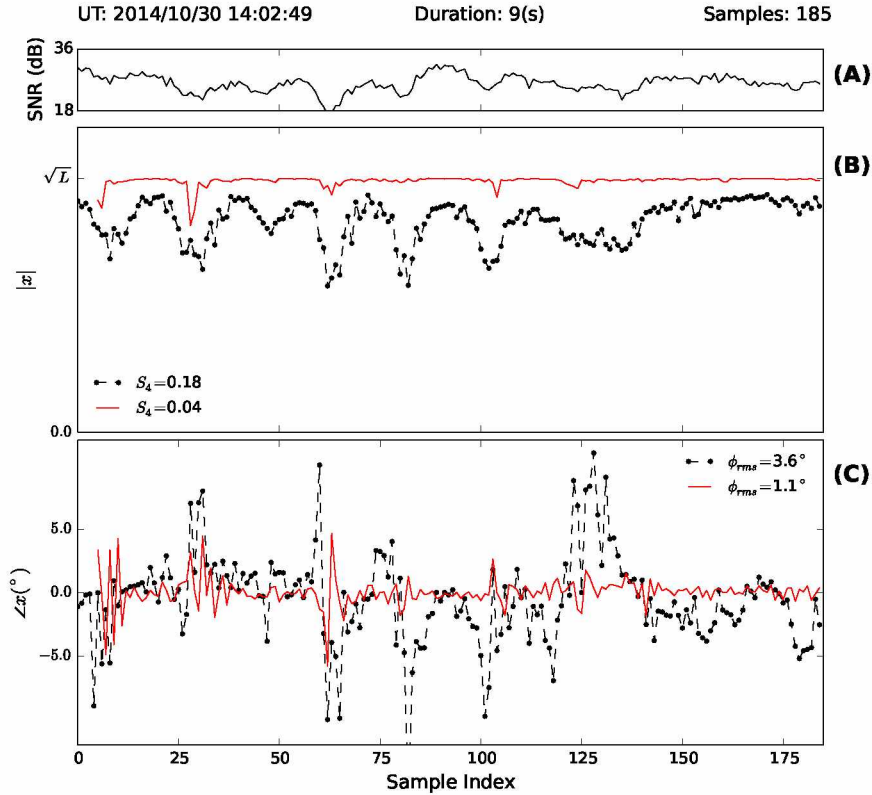
Figure 2.6: Comparison of (A) SNR, (B) amplitude, (C) phase history of measured (black) and corrected (red) beamformed signals across array during the same observation interval illustrated in Figure (2.5).

2.5 Discussion

Table (2.3) illustrates the factor by which the scintillation metrics have been reduced and the radar performance improved after wavefront correction for each of the observation intervals. During the five minute period investigated, the amplitude and phase scintillation of the beamformed signal was typically reduced by a factor in the range $[2, 5]$. The radar angular resolution showed substantially more improvement with a reduction in uncertainty of as much as an order of magnitude and no less than a factor of 3 for the least-squares estimation used. Finally, wavefront correction provided a modest improvement in array gain of at least 0.7 (dB) during the period. The results presented in Table (2.1) illustrate that diffraction during ionospheric propagation does significantly reduce radar performance for HF phased arrays by producing significant phase and amplitude fluctuations over the

Period	$\frac{S_{4-Obs}}{S_{4-Corr}}$	$\frac{\phi_{rms-Obs}}{\phi_{rms-Corr}}$	$\frac{\sigma^2_{\omega_s-Obs}}{\sigma^2_{\omega_s-Corr}}$	$E[L_{array-Obs}] - E[L_{array-Corr}]$
1	2.17	2.77	3.00	0.87
2	1.42	4.38	4.41	0.70
3	4.67	3.03	10.32	0.79
4	5.2	2.88	14.00	1.52
5	2.2	2.33	2.99	1.16

Table 2.3: Reduction factor in scintillation metrics and radar performance between measured and corrected data.

dimensions of the radar aperture. However, it is straightforward to determine phase and amplitude correction factors for each antenna element in the array by comparison of the measured wavefront with an ideal plane wave as described in section (2.3). Further, the wavefront distortion varies slowly enough in the period studied here that linear predictive filtering can effectively track the variations in amplitude and phase to yield substantially improved radar performance and reduce the scintillation observed in the beamformed signal as demonstrated in Tables (2.2)-(2.3). While the unevenly spaced sampling times of the data sets here (as described in section(2.4.2)) are not ideal for estimating the rate at which the phase and amplitude fluctuations varied over the observation period it is reasonable to assume it is slow in comparison to $^1/_{PRF} = 20$ (ms) given the success of predictive filtering.

An important note about this study is that it has been performed with point targets in mind. Specifically, the scintillation correction algorithm is based on the assumption that the target produces a planar wavefront under ideal conditions - i.e. the target emits spherical waves and is located in the far-field with respect to the radar. On the other hand, distributed targets are composed of many scattering centers. These scattering centers may produce a wavefront at the radar whose amplitude and phase fluctuate due to interference, an effect indistinguishable from scintillation. Applying the scintillation correction algorithm presented here to a clutter target for example would increase the array gain and reduce fluctuations in the coherently summed signal but at the expense of information about geometric interference effects. This may still be useful however if the objective of the study is to investigate refractive

effects as in *Bristow and Greenwald* [1995] or *Theurer and Bristow* [2012] where scintillation in the signal amplitude due to diffraction obscures the estimation of the total amount of power diverted into a given angular extent or range gate. A topic the authors are currently studying is discriminating geometric interference from scintillation which is particularly challenging for propagation via ionospheric refraction. For example, many techniques that may be used to decorrelate geometric effects between observations such as varying wavelength, look-angle, or averaging over multiple clutter cells (see *Attia and Steinberg* [1989]) also effect wave propagation through the ionosphere as can be seen from the expression for the index of refraction[*Budden* [1985]] and would produce a corresponding change in the observed scintillation.

2.6 Conclusion

Diffraction during ionospheric propagation produces wavefronts whose amplitude and phase fluctuate over dimensions comparable to those of HF phased array radars such as SuperDARN. The result of this time-varying wavefront distortion is amplitude and phase fluctuations in the beamformed signal and a reduction in radar performance in terms of angular resolution and achieved array gain. In the experiment presented here wavefront distortion produced weak to moderate amplitude scintillation and strong phase scintillation in the beamformed signal while reducing azimuth resolution by an order of magnitude and the achieved array gain by a decibel. A correction algorithm based on AO techniques was presented that yields a wavefront approximating an ideal plane wave and is capable of tracking the slow time variations observed in this experiment. Applying the correction algorithm to the measured data set significantly reduced the observed scintillation, dramatically improved angular resolution, and provided a modest improvement in array gain.

3 Ground Clutter Spatial Correlation Analysis: Transverse Ionospheric Drift Velocity

3.1 Introduction

A long established radar technique of measuring atmospheric wind velocities is to measure the motion of the diffraction pattern produced on the ground by specular reflection from variations in the index of refraction [*Mitra*, 1949; *Briggs et al.*, 1950; *Briggs*, 1968]. The form of the observed diffraction pattern is often assumed but can be explicitly related to the statistical properties of the index of refraction in the scattering medium [*Doviak et al.*, 1996; *Holloway et al.*, 1997a]. The basis of these spatial correlation analysis techniques is the simple result from diffraction theory that the angular power spectrum is unchanged by propagation between parallel planes [*Ratcliffe*, 1956]. Therefore, a measurement of the correlation of the diffraction pattern across the ground can be used to deduce properties, such as a transverse velocity, of the electric field emerging from the scattering altitude of the atmosphere. Methods based on this concept include full correlation analysis [*Briggs et al.*, 1950] and spatial correlation analysis [*Briggs*, 1968; *Holloway et al.*, 1997b; *Holdsworth*, 1999] which have been used to evaluate drifts in the troposphere, stratosphere, and mesosphere.

The principal purpose of the Super Dual Auroral Radar Network (SuperDARN) is to provide a global convection plot of the $\mathbf{E} \times \mathbf{B}$ plasma drift in the high latitude ionosphere where $\mathbf{E}$ is the ionospheric electric field and $\mathbf{B}$ is the geomagnetic field [*Greenwald et al.*, 1985]. Each radar in the network measures back scatter from field aligned electron density irregularities in the F-region and hence derives the line-of-sight component of the $\mathbf{E} \times \mathbf{B}$ drift within its field-of-view. A global convection plot can then be constructed from overlapping, independent drift measurements [*Ruohoniemi and Baker*, 1998]. In addition to back scatter from ionospheric irregularities, these HF radars also observe ground clutter from signals that reflect from the ionosphere, scatter from the ground, and return to the radar via the same path. A typically undesired data product, our objective here is to demonstrate that ground clutter returns carry information about the $\mathbf{E} \times \mathbf{B}$ plasma drift *transverse* to the

look direction of the radar and that spatial correlation analysis techniques may be used to derive this component of the drift.

Here we will use the optics term for the correlation of the electric field at two-points and two-times, which is the mutual-coherence function (MCF) defined as,

$$\Gamma(\xi, \tau) = \iint E(x, t) E^*(x + \xi, t + \tau) dx d\tau \tag{3.1}$$

where $E(x, t)$ denotes the low-pass electric field observed at (x, t), the limits of integration are $[-\infty, \infty]$, and (ξ, τ) are space and time displacements. The motivation for this study came from measurements of $|\Gamma(\xi, \tau)|$ for range cells containing oblique ground scatter observed by the Kodiak SuperDARN HF radar such as Figure (3.1). Note that the contour plot in
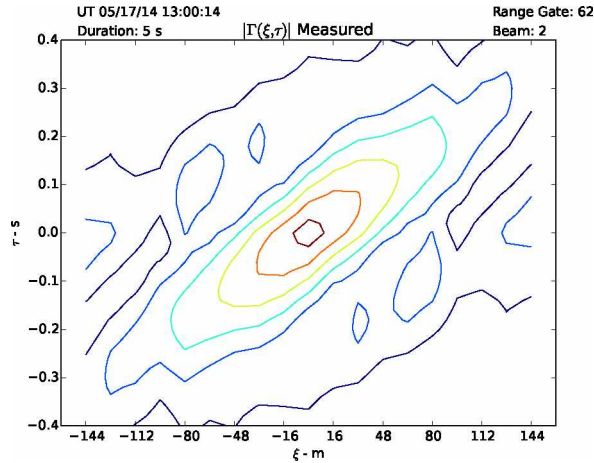
Figure 3.1: Example of measured contours of $|\Gamma(\xi, \tau)|$ for a single range gate containing ground clutter.

Figure (3.1) was generated by evaluating the discretized form of (3.1) using the time-series of received echoes at each antenna in the 16 element array over the annotated observation period for a range gate known to contain ground clutter. The most significant aspect of Figure (3.1) is that the elliptical contours are rotated in the (ξ, τ) plane which suggests that we have a relationship of the form $\Gamma(\xi, \tau) \approx \Gamma(\xi - v\tau)$. This in turn means that the spatial distribution of the backscattered electric field appears to move coherently across the radar

aperture, a result that is not as intuitive for backscatter from a fixed target such as the ground as it is for scatter from moving irregularities in the atmosphere.

In this paper we will model the ionosphere as a thin, moving diffractive screen and examine the scenario of oblique ground scatter as diffraction from the screen on the forward path, reflection from the ground, and diffraction from the screen on the backward path. We will demonstrate that the observed MCF will have the form $\Gamma(\xi - v\tau)$ where v denotes the transverse screen velocity and that the general expression for $\Gamma(\xi, \tau)$ in terms of the angular power spectrum is equivalent to what would be expected if the clutter cell was considered an incoherent optical source. Measurements of ionospheric drifts made using this technique and data from the Kodiak SuperDARN radar are presented.

3.2 Theory

The objective of this section is to demonstrate that the observed MCF of oblique ground scatter will have the form $\Gamma(\xi - v\tau)$ if the ionospheric region over which the diffraction occurs is moving with a velocity, v, transverse to the radar look direction. The geometry considered here is illustrated in Figure (3.2). Figure (3.2A) illustrates a linear array of antennas that
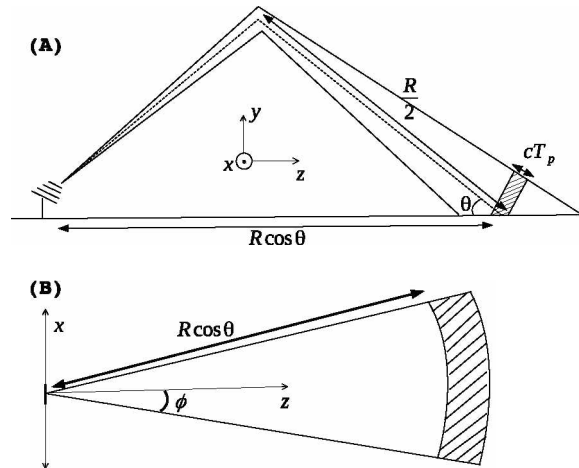
Figure 3.2: (A) illustrates a radar obliquely illuminating an area of ground. (B) illustrates overhead projection of oblique illumination

obliquely illuminates an area of ground at a distance R from the radar. The transmitted

pulse of duration T_p arrives at an incidence angle θ that we will assume here is equal to the take off angle. We will further assume that the distance R is much greater than the footprint of the pulse so that θ is approximately constant over the illuminated area. In the overhead projection of the same scenario illustrated in Figure (3.2B) the radar appears as a narrow slit aperture oriented along the x-axis that illuminates an area of ground at a radial distance $\rho = R\cos\theta$ (where $x \ll z$, i.e narrow transmit beam). For clarity we will first illustrate the basic relationship between the electric field observed in a given plane in Figure (3.2B) and the angular spectrum of waves incident on that plane. We then model the ionosphere as a thin diffractive layer inserted between the radar aperture and the illuminated area as in Figure (3.3) and use diffraction theory to evaluate the field in different planes in Figure (3.3) along the forward and reverse propagation paths to arrive at the result $\Gamma(\xi,\tau) = \Gamma(\xi - v\tau)$.
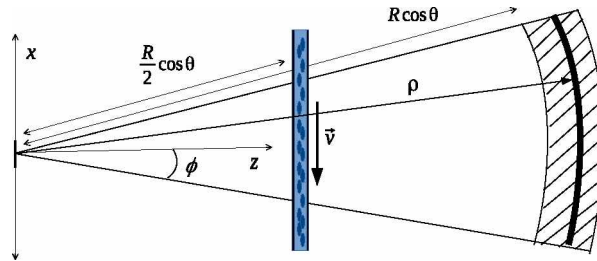
Figure 3.3: Overhead projection of oblique illumination with a diffractive screen at the midpoint of the propagation path. Note that the polar coordinates (ρ,ϕ) are related to the Cartesian Cartesian coordinates (x,z) by the relationships $\rho = \sqrt{x^2 + z^2}$ and $\phi = \tan^{-1}(x/z)$.

3.2.1 Angular Spectrum

Consider Figure (3.4) which illustrates a linearly polarized plane wave in a Cartesian coordinate system propagating away from an arbitrary (x,y) plane. If we define θ as the elevation angle with respect to the (x,z) plane and ϕ as the azimuth angle with respect to

the z-axis the plane wave may be expressed as,
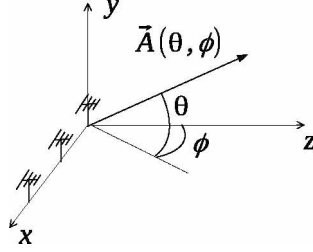
Figure 3.4: Plane wave geometry for definition of angular spectrum.

$$\vec{A} = A(\theta, \phi)e^{j(\vec{k}\cdot\vec{r}-\omega t)}$$
$$= A(\theta, \phi)e^{j\frac{2\pi}{\lambda}(x\cos\theta\sin\phi + z\cos\theta\cos\phi + y\sin\theta)}e^{-j\omega t} \tag{3.2}$$

where $A(\theta, \phi)$ is the (complex) amplitude and $\omega = 2\pi f_c$ is the center frequency of the wave. The projection of the wave in (3.2) onto the x-axis in a given (y, z) plane is,

$$E(x) = \vec{A} \cdot \hat{x}$$
$$= A(\theta, \phi)\cos\phi e^{j\frac{2\pi}{\lambda}(x\cos\theta\sin\phi + z\cos\theta\cos\phi + y\sin\theta)}e^{-j\omega t} \tag{3.3}$$

and represents the relationship between the electric field across a slit aperture along the x-axis and the spectrum of waves in (ϕ, θ) that are radiated. In the case of oblique ground scatter from a single range gate, Figure (3.2) illustrates that the signal of interest consists of a spectrum of plane waves that have a fixed elevation angle θ_0 but a spread of azimuth angles ϕ. The projection of the electric field onto the x-axis in Figure (3.4) is then the integral over

the azimuth angular spectrum for a given elevation angle θ_0 given by,

$$E(x) = e^{j(\frac{2\pi}{\lambda} \sin \theta_0 y - \omega t)} \int A(\theta_0, \phi) \cos \phi e^{j\frac{2\pi}{\lambda}(x \cos \theta_0 \sin \phi + z \cos \theta_0 \cos \phi)} d\phi$$

$$E(x) \approx \int A'(\phi) e^{jk'(x \sin \phi + z \cos \phi)} \cos \phi d\phi \qquad (3.4)$$

where we've made the substitutions $k' = \frac{2\pi}{\lambda} \cos \theta_0$ and $A'(\phi) = A(\theta_0, \phi)$ and have omitted the term $e^{j(k \sin \theta_0 y - \omega t)}$ that is independent of ϕ. Note that the limits of integration in (3.4) are $[-\frac{\pi}{2}, \frac{\pi}{2}]$ but can be made $[-\infty, \infty]$ without physically altering the problem [*Ratcliffe*, 1956]. If we make one further substitution, $S = \sin \phi$, then (3.4) has the conventional form from diffraction theory,

$$E(x) = \int F(S) e^{jk'(xS + zC)} dS \qquad (3.5)$$

where $F(S) = A'(\sin^{-1} S)$ and $C = \cos \phi$ [*Ratcliffe*, 1956]. We will denote the Fourier transform operation in (3.5) as $\mathcal{F}_f\{\cdot\}$ where the subscript f signifies that it is the relationship between the field $E(x)$ and an azimuth spectrum of waves propagating in the forward or $+(x, z)$ direction. In the event that the azimuth angular spectrum is narrow, as is the case when the transmitted beam width is small, then (3.5) can be approximated as,

$$E(x) = \int A'(\phi) e^{jk'(x\phi + z)} d\phi \qquad (3.6)$$

which is obtained from (3.5) using first-order terms of the Taylor series expansions of $(\sin \phi, \cos \phi)$ and represents a direct Fourier transform relationship between the azimuth spectrum of plane waves and the amplitude of the electric field along the x-axis.

In the event we had drawn the wave normal in the opposite direction in Figure (3.4) to represent a plane wave arriving at the given (x, y) plane we would have

$$\vec{k} = < -\cos \theta_0 \sin \phi, -\cos \theta_0 \cos \phi, -\sin \theta_0 >$$

and the corresponding change in (3.5) would be,

$$E(x) = \int F(S)e^{-jk'(xS+zC)}dS \qquad (3.7)$$

We will denote the Fourier transform operation in (3.7) as $\mathcal{F}_b\{\cdot\}$ to signify that it is the relationship between $E(x)$ and an azimuth spectrum of waves propagating in the $-(x, z)$ direction.

3.2.2 Diffracting Screen Model

Here we will briefly describe a simplified model of the diffracting screen. The problem of a normally incident plane wave propagating through an ionospheric layer containing random variations of the mean electron density N is described by *Ratcliffe*. In the specific case that the density variations, $\Delta N(x)$, have a Gaussian autocorrelation function with standard deviation N_m, *Ratcliffe* demonstrates that the angular power spectrum $|F(S)|^2$ consists of an undeviated component in addition to a side wave spectrum that is proportional to,

$$|F_{side}(S)|^2 \propto e^{-\pi^2 \xi_0^2 S^2} \qquad (3.8)$$

where ξ_0 is the scale size of the electron density deviations normalized to wavelength [*Ratcliffe*, 1956]. The ratio of power in the undeviated component of the angular spectrum to the power in the side wave spectrum is $\simeq \phi_m^{-2}$ where ϕ_m is given by,

$$\phi_m = \left(\frac{\pi^{3/4}e^2}{\epsilon_0 mc}\right)\frac{1}{f}(\xi_0 Z)^{1/2}N_m \qquad (3.9)$$

In (3.9) e is electron charge, ϵ_0 is the permittivity of free space, m is the mass of an electron, c is the speed of light, f is the wave frequency, and Z is the thickness of the layer. Note that (3.8) only holds for $\phi_m \ll 1$ [*Ratcliffe*, 1956]. If we considered the ionosphere as a series of stratified layers with increasing mean density N then the standard deviation N_m

is likely greatest at the midpoint of the propagation path where N itself is greatest and consequently most of the diffractive effects occur in this region. In this paper we assume that the ionospheric conditions are such that (3.8)-(3.9) are valid. Therefore, the effect of the diffractive screen is a transformation of the incident angular spectrum $\delta(S)$ into the scattered spectrum $|F(S)|^2$ where $|F(S)|^2$ has a dominant component at $S = 0$ and a small amount of power distributed around $S = 0$. We further assume that (3.8)-(3.9) holds for small incidence angles $S_i \ll 1$ such that the scattered angular spectrum for an incident plane wave $\delta(S - S_i)$ is $|F(S - S_i)|^2$.

The discussion above describes the properties of the magnitude of the angular spectrum, at least in an ensemble averaged sense. If the ionosphere is moving with some bulk velocity transverse to the look direction of the radar then the phase of the scattered angular spectrum also has important properties. First, consider the received signal at a discrete point on the ground as the screen moves overhead as depicted in Figure (3.5). As illustrated, the
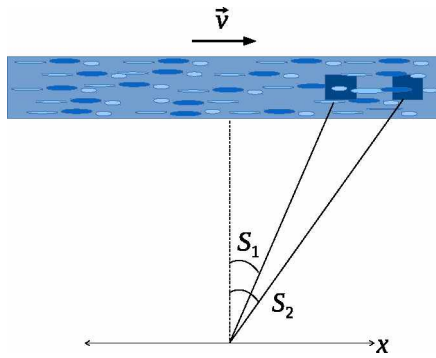
Figure 3.5: Illustration of the received signal at a point on the x-axis from a moving diffractive screen.

received signal from the direction S_i originates from a differential volume of the screen that lies along a ray at the angle S_i between the observation point and the screen. For a screen moving with horizontal velocity v, the line-of-sight velocity of the differential volume along the ray at S_i relative to the given point on the ground is vS_i. Our model of the

moving screen should therefore include a mean Doppler shift of $-k'vS_i$ for the plane wave S_i diffracted by the screen during forward propagation. Second, we note that the weak side waves scattered in direction $S \neq S_i$ are Doppler shifted by an amount relative to their displacement $S - S_i$ from the undeviated component of the scattered spectrum. To see this, note that we've described the effect of the diffracting layer as a convolution operation which transforms the incident angular spectrum $\delta(S - S_i)$ into the scattered spectrum $F(S - S_i)$. From the fundamental properties of Fourier transform theory we can express the convolution operation in the angular spectrum as a product operation in the spatial spectrum. Let $\mathcal{F}_f\{F(S)\} = f(x)$ and note that $\mathcal{F}_f\{\delta(S - S_i)\} = e^{jk'xS_i}$. Then if our screen representing the ionosphere is displaced by an amount $\Delta x = vt$, the scattered angular spectrum for an incident plane wave $\delta(S - S_i)$ is:

$$
\begin{aligned}
F(S) &= \mathcal{F}_f^{-1}\{f(x - vt)e^{jk'xS_i}\} \\
&= \mathcal{F}_f^{-1}\{f(x)e^{jk'(x+vt)S_i}\} \\
&= e^{-jk'v(S-S_i)t}\mathcal{F}_f^{-1}\{f(x)e^{jk'xS_i}\} \\
&= e^{-j\omega_d t}F(S - S_i)
\end{aligned}
\tag{3.10}
$$

which is simply the original scattered angular spectrum for a plane wave input $\delta(S - S_i)$ Doppler shifted by $\omega_d = -k'v(S - S_i)$. Considering Figure (3.5), we expect the signal scattered in direction S_i to have a Doppler spectrum, $W(\omega)$, centered at $\omega = -k'vS_i$, but with some finite width due to the contributions of weak side waves that are Doppler shifted by other amounts.

Based on the discussion above, we conclude that the scattered angular spectrum can be represented as $F(S, \omega)$. The component $F(S_i, \omega)$ of the scattered angular spectrum is dominated by the undeviated plane wave $\delta(S - Si)$ in the incident angular spectrum but contains weak side wave contributions from waves $S \neq S_i$ in the incident angular spectrum. In terms of Doppler, $F(S_i, \omega)$ is centered around $\omega_d = -k'vS_i$ but will have some finite width

due to side wave contributions shifted by other Doppler amounts. Up to this point we've discussed the effect of the diffracting screen solely in terms of the angular domain $F(S)$ while the main result we are after is an effective motion of the diffraction pattern $E(x)$ in the spatial domain. The effects in the two domains are tied together by the relationship in (3.5) (or (3.7) for $\vec{k} = -\vec{k}$). We've argued here that a moving ionosphere produces the special phase relationship $e^{-jk'vSt}$ in the angular domain and from (3.5) one can demonstrate that the corresponding effect in the spatial domain is exactly the result we are after, i.e. the diffraction pattern $E(x)$ can be expressed as $E(x - vt)$ in this case. Therefore the two effects are equivalent; if the observed diffraction pattern in a plane appears to move coherently then the angular spectrum of plane waves incident on that plane must be Doppler shifted in proportion to their incidence angle S.

3.2.3 Forward Propagation

The HF radars under consideration here transmit a broad elevation spectrum but a narrow azimuth spectrum with a half-power beamwidth of $\phi_{BW} \approx 7°$. As illustrated in Figure (3.2A) we expect the illuminated area of ground corresponding to a given range gate to have a constant elevation angle θ_0 so that we can work instead with the two dimensional geometry illustrated in Figure (3.2B) where it is understood that $\theta = \theta_0$ is fixed. Referring now to Figure (3.3), when the slit aperture representing the radar is excited with a field distribution $E_t(x)$, a narrow azimuth spectrum of waves $F_t(S) = \mathcal{F}_f^{-1}\{E_t(x)\}$ is emitted. Each of these component waves will propagate to the diffracting screen illustrated in Figure (3.3) experiencing a phase delay related to the given direction of propagation. Now denote the angular spectrum of waves scattered from the diffracting screen on the forward path F_{s_f}. Assuming the ionospheric conditions are such that (3.8)-(3.9) are valid, we expect the magnitude of the S component of $|F_{s_f}(S)|$ to be $\propto |F_t(S)|$ but to contain a narrow Doppler spectrum centered at $\omega_d = -k'vS$. We will approximate the Doppler spectrum as $\delta(\omega - \omega_d)$ for the moment so that we have $F_{s_f}(S, \omega) \simeq F_{s_f}(S)e^{-jk'vSt}$ and consider the consequences of

a finite Doppler width $\Delta\omega$ in section (3.2.5).

Now consider Figure (3.6) which illustrates the geometry between the field distribution emerging from the diffractive screen and the field distribution along an arc in the illuminated area where the position along the arc is denoted in polar coordinates (ρ, ϕ). The electric
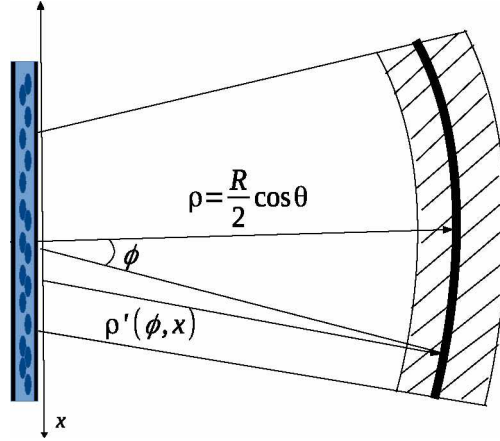
Figure 3.6: Geometry of a propagation between diffractive screen and illuminated area.

field distribution across the diffractive screen is $E_{s_f}(x) = \mathcal{F}_f\{F_{s_f}(S)\}$. Using the narrowband approximation to the Huygen's-Fresnel principle [*Goodman*, 2005] we could express the field along the arc as,

$$E_\rho(\phi) = \frac{1}{j\lambda} \int E_{s_f}(x) e^{jkr(\phi,x)} \frac{\chi(\phi)}{r(\phi,x)} dx \qquad (3.11)$$

where $r(\phi, x)$ is the phase path length between $E_{s_f}(x)$ and the point (ρ, ϕ) on the arc and $\chi(\phi)$ is an obliquity factor. If we assume that $|\phi| \ll 1$ and $|x| \ll \frac{R}{2}\cos\theta_0$ then the obliquity

factor $\chi(\phi) \approx 1$ and the phase path length may be simplified as follows from Figure (3.6),

$$
\begin{aligned}
r(\phi, x) &= \frac{\rho'(\phi, x)}{\cos \theta_0} = \frac{1}{\cos \theta_0} \sqrt{\rho^2 + x^2 - 2\rho x \cos(\frac{\pi}{2} - \phi)} \\
&= \frac{1}{\cos \theta_0} \sqrt{\rho^2 + x^2 - 2\rho x \sin \phi} \\
&\approx \frac{\rho}{\cos \theta_0} \sqrt{1 - 2\frac{x}{\rho} \sin \phi} \\
&\approx \frac{\rho}{\cos \theta_0} - \frac{x\phi}{\cos \theta_0}
\end{aligned}
\tag{3.12}
$$

Substituting these approximations into (3.11) we arrive at,

$$
\begin{aligned}
E_\rho(\phi) &\approx \frac{\cos \theta_0 e^{jk\frac{\rho}{\cos \theta_0}}}{j\lambda\rho} \int E_{s_f}(x) e^{-jkx(\frac{\phi}{\cos \theta_0})} dx \\
&\approx \frac{\cos \theta_0 e^{jk\frac{\rho}{\cos \theta_0}}}{j\lambda\rho} F_{s_f}(\frac{\phi}{\cos^2 \theta_0})
\end{aligned}
\tag{3.13}
$$

which illustrates that the amplitude of the electric field at the point (ρ, ϕ) in the illuminated area is proportional to the amplitude of the plane wave propagating in the direction $\frac{\phi}{\cos^2 \theta_0}$ away from the diffracting screen. Our conditions $|\phi| \ll 1$ and $|x| \ll \frac{R}{2} \cos \theta_0$ correspond to conditions on the width ΔS of the angular spectrum $|F_{s_f}(S)|$ emerging from the screen and the width Δx of the electric field $|E_{s_f}(x)|$ across the screen. We've already noted that here we are assuming that the width ΔS of $|F_{s_f}(S)|$ is approximately that of the transmitted spectrum so we have $\Delta S \approx \phi_{BW} \ll 1$. Under this same assumption the ratio $\Delta x / R \cos \theta_0 \simeq \phi_{BW}$ and so both conditions are satisfied.

3.2.4 Reverse Propagation

When the electric field $E_\rho(\phi)$ in (3.13) scatters from the ground we expect most of the energy in the signal to be specularly reflected. The direction of specular reflection depends on the relative orientiation of the surface normal at a given point and so this will in general not be in the direction of the radar. However, due to the roughness of the terrain some fraction of the signal will be scattered in all other directions. Now for a given point (ρ, ϕ)

in the illuminated area of Figure (3.6), the radar will receive that fraction of the signal that happens to be scattered back in the direction (θ_0, ϕ). We can write this fraction of the signal as $\sigma(\rho, \phi)E_\rho(\phi)$. Now at this point we can again apply the Huygen's-Fresnel principle to find the electric field arriving at the diffractive screen, E_{s_g}, in terms of those signals, $\sigma(\rho, \phi)E_\rho(\phi)$, scattered back in the direction of the radar:

$$
\begin{aligned}
E_{s_g}(\rho, x) &= \frac{1}{j\lambda} \int \sigma(\rho, \phi)E_\rho(\phi)e^{jkr(\phi,x)}\frac{\chi(\phi)}{r(\phi,x)}\,d\phi \\
&\approx -\left(\frac{\cos\theta_0}{\lambda\rho}\right)^2 e^{j2k\frac{\rho}{\cos\theta_0}} \int \sigma(\rho, \phi)F_{s_f}(\frac{\phi}{\cos^2\theta_0})e^{-jkx\frac{\phi}{\cos\theta_0}}\,d\phi \\
&\approx -\left(\frac{\cos^2\theta_0}{\lambda\rho}\right)^2 e^{j2k\frac{\rho}{\cos\theta_0}} \int \sigma(\rho, \phi\cos^2\theta_0)\ F_{s_f}(\phi)e^{-jk'x\phi}d\phi
\end{aligned}
\tag{3.14}
$$

Note that in the second line of (3.14) we've substituted the expression in (3.13) for $E_\rho(\phi)$ and also applied the same approximations for $r(\phi, x)$ and $\chi(\phi)$ given in the previous section. In the third line we've made the variable substitution $\phi = \phi\cos^2\theta_0$ and simplified. Note that the expression in (3.14) includes only the contribution to the electric field from those points along an arc of fixed radius ρ within the illuminated area. The total field incident on the diffractive screen is found by integrating over the radial extent of the illuminated area,

$$
\begin{aligned}
E_{s_g}(x) &= \int E_{s_g}(\rho, x)d\rho \\
&= \int F_{s_f}(\phi)e^{-jk'x\phi}d\phi\left\{ -\int \sigma(\rho, \phi\cos^2\theta_0)\left(\frac{\cos^2\theta_0}{\lambda\rho}\right)^2 e^{j2k\frac{\rho}{\cos\theta_0}}\,d\rho\right\} \\
&= \int \sigma'(\phi)F_{s_f}(\phi)e^{-jk'x\phi}d\phi
\end{aligned}
\tag{3.15}
$$

where $\sigma'(\phi)$ represents an effective backscatter coefficient given by the bracketed expression in the second line of (3.15). Note that this bracketed expression is a definite integral over the radial extent of the illuminated area which depends on the width of the transmitted pulse and the incidence angle θ_0. While we haven't explicitly included it in (3.13)-(3.15), the wave $F_{s_f}(\phi)$ contains a factor $e^{-jk'v\phi t}$ where v is the transverse velocity of the screen

41

as discussed in section (3.2.2)-(3.2.3). However, it is important to note that after reflection from the ground there are two Doppler effects we must account for. The first is a change in the sign of the Doppler shift as the term $-k'vS_i$ discussed in sections (3.2.2)-(3.2.3) is the shift observed by the radar. The wave at angle S_i observed (and reflected) by the ground has a corresponding Doppler shift of $+k'vS_i$ because of the reversal in orientation of the receiver and source terms in the Doppler equation. Second, we note that the S_i wave will gain an additional Doppler shift of $k'vS_i$ due to reflection from the ground. To see this, refer to Figure (3.5) and note that the two way phase path between a point (ρ, ϕ) in the illuminated area and a differential volume in the direction S_i is changing at the rate of $2k'vS_i$. Taking this into account we substitute $F_{s_f}(\phi) = F_{s_f}(\phi)e^{j2k'v\phi t}$ into (3.15) to obtain:

$$
\begin{aligned}
E_{s_g}(x) &= \int \sigma'(\phi) \left\{ F_{s_f}(\phi)e^{j2k'v\phi t} \right\} e^{-jk'x\phi} d\phi \\
&= \int \sigma'(\phi) F_{s_f}(\phi) e^{-jk'(x-2vt)\phi} d\phi \\
&= E_{s_g}(x - 2vt)
\end{aligned}
\tag{3.16}
$$

which illustrates that the electric field in the plane of the screen propagates along the x-direction with twice the apparent velocity of the screen itself. This is an important distinction as it implies we do not see a second Doppler shift. Specifically, from (3.7) a relationship of the form in (3.16) means that the component wave $\delta(S - S_i)$ incident on the diffractive screen during back propagation has a Doppler shift of $-2\omega_d = 2k'vS_i$. Diffraction from the screen a second time will produce a Doppler shift of $(-2\omega_d) + \omega_d = -\omega_d = k'vS_i$. Denote the angular spectrum of waves diffracted by the screen on back propagation as $F_{s_b}(S)$. Again using (3.7), note that if $F_{s_b}(S)$ has the phase relationship $e^{jk'vS}$ then the scattered electric field distribution $E_{s_b}(x) = \mathcal{F}_b\{F_{s_b}(S)\}$ will have the property $E_{s_b}(x) = E_{s_b}(x - vt)$ where v is the transverse velocity of the screen.

At this point, consider the MCF $\Gamma_{s_b}(\xi)$ of the electric field emerging from the screen as defined in (3.1). Using the Wiener-Khintchine theorem [*Goodman*, 1985] and the Fourier

integral in (3.7), the following Fourier relationship can be shown to exist between the MCF $\Gamma(\xi)$ across any plane and the corresponding angular power spectrum,

$$\Gamma(\xi) = \int |F(S)|^2 e^{-jk'\xi S} dS \tag{3.17}$$

As the wave $F_{s_b}(S)$ propagates from the screen back towards the radar only the phase of the wave will change so that $|F_{s_b}(S)|^2$ incident on the radar remains the same. Therefore, if the MCF of the electric field across the diffractive screen, $\Gamma_{s_b}(\xi, \tau)$, has the property that $\Gamma_{s_b}(\xi, \tau) = \Gamma_{s_b}(\xi - v\tau)$ then the MCF across the radar aperture, $\Gamma_r(\xi, \tau)$, will also have the property $\Gamma_r(\xi, \tau) = \Gamma_r(\xi - v\tau)$ which is what we set out to demonstrate.

3.2.5 Observed Mutual Coherence Function

A more general expression for the MCF than (3.1) that allows for time variations in the diffraction pattern is,

$$\Gamma(\xi, \tau) = \iint E(x, t) E^*(x + \xi, t + \tau) dx dt \tag{3.18}$$

where the limits of integration are again $[-\infty, \infty]$. The Wiener-Khintchine theorem extended to two-variables then yields the following relationship for the received MCF,

$$\Gamma(\xi, \tau) = \iint |F(S, \omega)|^2 e^{-jk'\xi S} e^{j\omega\tau} dS d\omega \tag{3.19}$$

where $|F(S, \omega)|^2$ represents the distribution of power in the (S, ω) plane. In sections (3.2.3)-(3.2.4), we assumed that $F(S, \omega) = F(S)\delta(\omega)$ so that after allowing for an angular specific

Doppler shift produced by the diffractive screen (3.19) simplifies to,

$$\Gamma(\xi, \tau) = \iint |F(S)|^2 \delta(\omega - \omega_d(S)) e^{-jk'\xi S} e^{j\omega\tau} dS d\omega$$

$$= \int |F(S)|^2 e^{-jk'\xi S} dS \int \delta(\omega - k'vS) e^{j\omega\tau} d\omega$$

$$= \int |F(S)|^2 e^{jk'v\tau S} e^{-jk'\xi S} dS$$

$$= \int |F(S)|^2 e^{-jk'(\xi - v\tau)S} dS \tag{3.20}$$

However, the motion of the diffractive screen and time variations in the ground scatter coefficient, or the incidence angle θ_0 (which effects the ground scatter coefficient) produce spreading in the Doppler spectrum of $|F(S,\omega)|^2$. Here we will assume that the Doppler spread is independent of azimuth angle S so that $|F(S,\omega)|^2$ is separable into the product $|F(S)|^2 |W(\omega)|^2$ in which case we would arrive at the following expression for the received mutual coherence function,

$$\Gamma(\xi, \tau) = \iint |F(S)|^2 |W(\omega - \omega_d(S))|^2 e^{-jk'\xi S} e^{j\omega\tau} dS d\omega$$

$$= \int |F(S)|^2 e^{-jk'\xi S} dS \int |W(\omega - k'vS)|^2 e^{j\omega\tau} d\omega$$

$$= A(\tau) \int |F(S)|^2 e^{jk'v\tau S} e^{-jk'\xi S} dS$$

$$= A(\tau) \int |F(S)|^2 e^{-jk'(\xi - v\tau)S} dS \tag{3.21}$$

where $A(\tau)$ is the Fourier transform of the Doppler power spectrum $|W(\omega)|^2$. Equation (3.21) represents the general form of the MCF we expect to observe in terms of the received angular power spectrum $|F(S)|^2$ and an arbitrary Doppler spectrum $|W(\omega)|^2$ whose inverse is $A(\tau)$. To arrive at this expression we've assumed the ionosphere is moving with a transverse velocity v and spreads the angular power spectrum only a small amount on both forward and reverse propagation as discussed in sections (3.2.2)-(3.2.4).

It is also worth noting that if the illuminated area itself appears to be moving with

respect to the radar then (3.21) will require modification. Specifically, the velocity of the illuminated area could be decomposed into perpendicular and transverse components. The perpendicular component will produce a Doppler shift independent of look angle that would be observed in (and could be determined from a linear fit to) $\angle\Gamma(0,\tau)$. The transverse component of the velocity of the illuminated area would produce the same effect that the screen produces which is an angular specific Doppler shift. We would expect the received MCF to be of the form $\Gamma(\xi - v'\tau)$ where v' is the sum of the transverse velocities of the screen and the illuminated area. In general we don't expect ground clutter to have a significant velocity relative to the radar. The size of the illuminated area on the ground is of the order of hundreds of square kilometers so it is difficult to imagine there being a net motion in any direction and it is specifically this property (negligible Doppler velocity) which is used to identify a particular range gate as ground clutter. One specific exception is back scatter from the ocean; the results analyzed here are for terrain back scatter so this case won't be pursued further.

In general we don't have any a priori knowledge about the forms of $A(\tau)$ and $|F(S)|^2$ in (3.21). However, note from (3.21) that the shape of the $|\Gamma(\xi, 0)|$ cross-section depends only on $|F(S)|^2$ and not $A(\tau)$. Measured cross-sections of $|\Gamma(\xi, 0)|$ typically appear to have either a decaying exponential or Gaussian form. In the event that $|\Gamma(\xi, 0)|$ is well represented by a decaying exponential then the received angular spectrum must have a Lorentzian form such as,

$$|F(S)|^2 = \frac{2\beta}{\beta^2 + S^2} \tag{3.22}$$

On the other hand, if $|\Gamma(\xi, 0)|$ is Gaussian then the angular spectrum will have the form,

$$|F(S)|^2 = e^{-\beta S^2} \tag{3.23}$$

Regardless of the form of the angular spectrum, $A(\tau)$ was found to be accurately represented

by a Gaussian such as,

$$A(\tau) = e^{-\alpha\tau^2} \tag{3.24}$$

In the case that the received angular spectrum is Lorentzian, the observed MCF can be found from subsitituing (3.22) and (3.24) into (3.21) to find,

$$\Gamma(\xi,\tau) = e^{-k'\beta|\xi-v\tau|}e^{-\alpha\tau^2} \tag{3.25}$$

Note from (3.25) that the value of $k'\beta$ can be determined from a linear fit to $\ln|\Gamma(\xi,0)|$ and the value of α from a quadratic fit to $\ln|\Gamma(0,\tau)|$. The value of drift velocity v in expression (3.25) can be estimated by noting that the peak of the $|\Gamma(\xi,\tau=\tau_c|$ cross-section in the ξ dimension occurs at the point $\xi_{max} = v\tau_c$ where τ_c is an arbitrary constant. An illustration of the MCF in (3.25) for increasing drift velocity v is depicted in Figure (3.7) and clearly depicts a rotation that is proportional to drift velocity.
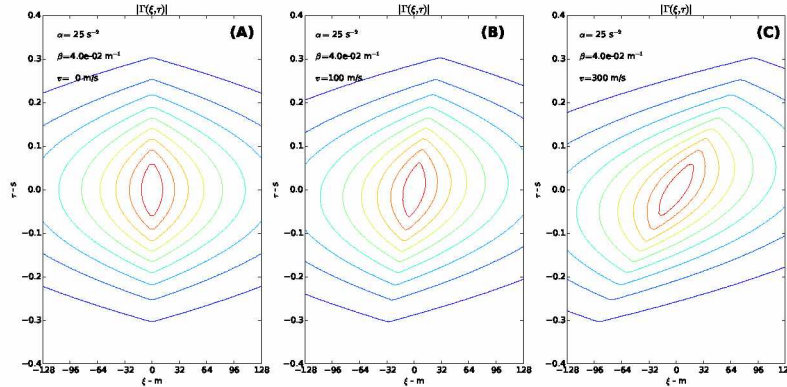
Figure 3.7: Contours of $|\Gamma(\xi,\tau)|$ for a Lorentzian angular angular spectrum that illustrate rotation for increasing values of drift velocity v.

In the case that the received angular spectrum is Gaussian the observed MCF can be found from substituting (3.23) and (3.24) into (3.21) to arrive at,

$$\Gamma(\xi,\tau) = e^{-\frac{k'^2}{4\beta}(\xi-v\tau)^2}e^{-\alpha\tau^2} \tag{3.26}$$

46

From (3.26), the contour of amplitude D can be expressed in a general quadratic form as,

$$A\xi^2 + B\xi\tau + C\tau^2 + \ln D = 0 \tag{3.27}$$

where,

$$A = \frac{k'^2}{4\beta}$$
$$B = \frac{-k'^2}{2\beta}v$$
$$C = \alpha + \frac{k'^2}{4\beta}v^2 \tag{3.28}$$

Noting from (3.28) that $B^2 - 4AC < 0$ for all (positive) values of (α, β) we will always have elliptical contours. After some analysis of (3.28), we can identify three effects of an increasing transverse velocity v for a given contour level. These three effects include a rotation in the (ξ, τ) plane, an increase in the diameter of the major principal axis, and a decrease in the diameter of the minor principal axis. These effects are depicted in Figure (3.8) and (3.9) for the annotated values of (α, β). Figure (3.8)(A)-(C) illustrates contour plots of $|\Gamma(\xi, \tau)|$ for increasing values of v while Figure (3.9)(A)-(C) illustrate the rotation angle θ_r and diameters of the principle axes of the $|\Gamma| = 0.5$ contour as the transverse velocity is varied over the range $[5, 500]$ (m/s). As discussed later in section (3.3), we will estimate velocity in this paper by noting that regardless of whether the observed MCF is of the form in (3.25) or (3.26) that the peak value of the $|\Gamma(\xi, \tau = \tau_c)|$ cross-section occurs at $\xi = v\tau_c$.

3.2.6 Relationship to Van-Cittert Zernike Theorem

In this section we note that the expression in (3.21) is equivalent to a form of the Van-Cittert Zernike theorem from optics [*Goodman*, 1985]. To illustrate this property, note that from Figure (3.3) we could express the received electric field in the *absence* of a diffractive screen using the Huygen's-Fresnel principle and the same approximations as in section (3.2.3)
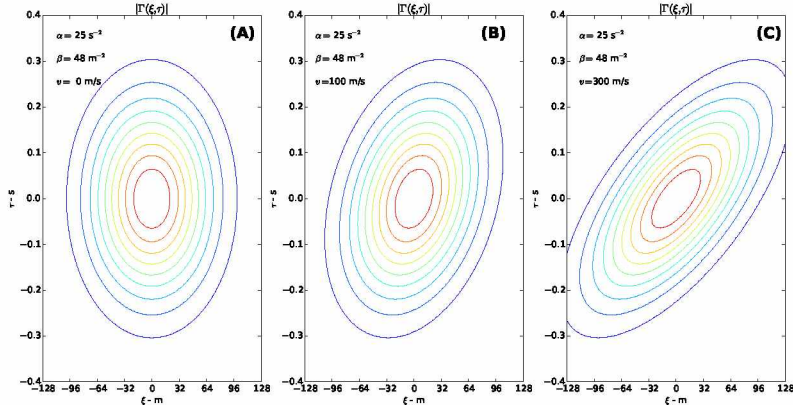
Figure 3.8: Contours of $|\Gamma(\xi,\tau)|$ for a Gaussian angular spectrum. The effect of an increasing drift velocity v is illustrated by a rotation and stretching/compression of major/minor principal axes.
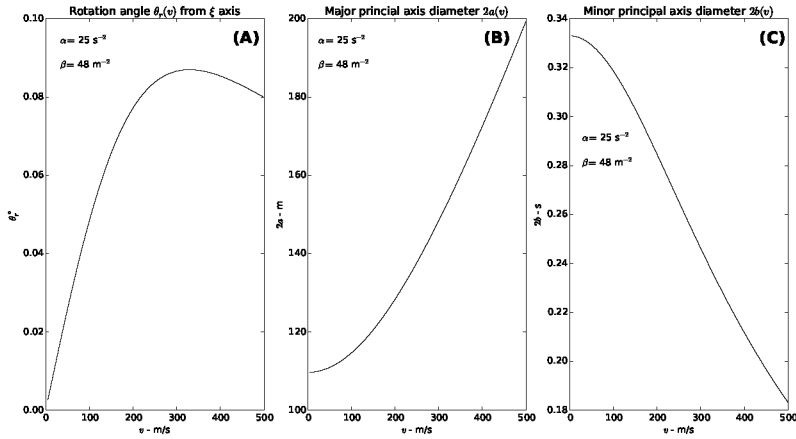
Figure 3.9: (A) illustates plot of rotation angle θ_r of elliptical contours of $|\Gamma(\xi,\tau)|$ as a function of drift velocity v. (B) and (C) illustrate the diameters of the major/ minor principal axes of the $|\Gamma(\xi,\tau)| = 0.5$ contour as a function of drift velocity v.

as,

$$E_r(x) \approx \int E_\rho(\phi) e^{-j\frac{k}{\cos\theta_0}x\phi} d\phi \qquad (3.29)$$

where $E_\rho(\phi)$ is the electric field in the illuminated area at point (ρ, ϕ). Note that the expression in (3.29) is a scaled form of (3.7) where in this case the incident angular spectrum of waves $A(\phi)$ can be expresssed in terms of the field distribution across the illuminated area

48

$E_\rho(\phi)$. From the Weiner-Khintchine Theorem the observed MCF is then,

$$\Gamma_r(\xi) \approx \int |E_\rho(\phi)|^2 e^{-j\frac{k}{\cos\theta}\xi\phi} d\phi \qquad (3.30)$$

Consider now the case that $E_\rho(\phi)$ is an *incoherent* source such that the value of $E_\rho(\phi)$ and $E_\rho(\phi + \Delta\phi)$ vary independently with time. The MCF is defined in this case as the ensemble averaged value,

$$\Gamma_r(\xi) = < E_r(x)E_r^*(x) > \qquad (3.31)$$

where $< \cdot >$ denotes the ensemble averaging operation. If we evaluate (3.31) using (3.29) and the incoherence property $< E_\rho(\phi_2)E_\rho^*(\phi_1) > = \delta(\phi_2 - \phi_1)$ we would again arrive at (3.30) demonstating that (3.30) is a form of the well-known Van-Cittert Zernike theorem from optics.

In (3.30), $\Gamma_r(\xi)$ is determined solely by the intensity distribution of the electric field in the illuminated area. Ignoring the scattering coefficent of the ground, the intensity distribution $|E_\rho(\phi)|^2$ will extend over an angular width $\phi_{BW} \approx \frac{\lambda}{L}$ where L is the spatial extent of the array. From (3.30) and the inverse spreading property of Fourier transforms the received field will be correlated over a distance of $(\lambda\cos\theta_0)\frac{L}{\lambda} = L\cos_{\theta_0}$. From the fact that (3.21) and (3.30) are equivalent in the absence of diffraction we find that $|F(S)|^2 = |E_\rho(\phi\cos^2\theta_0)|^2$ so that the angular power spectrum in (3.21) is a scaled version of the radar azimuth intensity pattern. Now in the presence of diffraction we expect the width of $|F(S)|^2$ to broaden at least slightly on each passage through the screen so we have $|F(S)|^2 > |E_\rho(\phi\cos^2\theta_0)|^2$. From (3.21) this in turn means that width of $|\Gamma_r(\xi)|$ will always be less than the ideal width of $L\cos\theta_0$. The similarity between (3.21) and (3.30) illustrates that oblique ground scatter can be thought of as an incoherent source whose angular width varies with the amount of diffraction that occurs during propagation through the ionosphere.

3.3   Algorithm

Our sole objective in this dissertation section is to evaluate a transverse velocity v from the measured MCF of the electric field across the radar aperture. We noted in the previous section that measured MCF's appear to be well modeled by either (3.25) or (3.26). A simple method of evaluating v regardless of which form of MCF is observed is to note that both these functions have the property that for a fixed time delay τ the peak of the cross-section $|\Gamma(\xi, \tau)|$ occurs along the ξ dimension at,

$$\xi_{max}(\tau) = v\tau \tag{3.32}$$

Using (3.32), we should be able to determine v by simply recording the spatial separation at which the peak value of the MCF occurs for every time lag. However, a limitation of this technique results from the discrete sampling of the (ξ, τ) plane. Let (ξ_s, τ_s) denote the discrete space and time delay sampling intervals due to the spacing of the antenna elements in the aperture and the pulse repetition frequency (PRF) the radar is operating at. Equations (3.32) can be re-written in terms of the sampling frequencies $f_\xi = \frac{1}{\xi_s}$ and $f_\tau = \frac{1}{\tau_s}$ as,

$$\xi_{max}(\tau) = v\tau$$
$$\frac{n}{f_\xi} = v\frac{m}{f_\tau}$$
$$n_{max} = v\frac{f_\xi}{f_\tau}m$$
$$n_{max} = \lfloor v\frac{f_\xi}{f_\tau}m + \frac{1}{2}\rfloor \tag{3.33}$$

where $\lfloor \cdot \rfloor$ denotes truncation to the nearest integer. The effect of the quantization in (3.33) is easily visible in measurement as illustrated in Figure (3.10) which depicts n_{max} evaluated from cross sections of the contour plot illustrated in Figure (3.1). Note that from (3.33) the
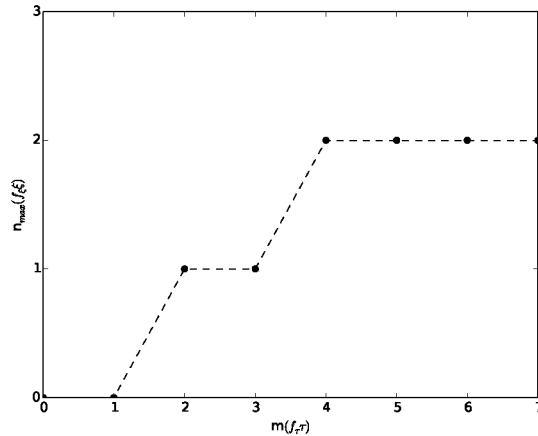
Figure 3.10: Example of quantization of (3.32) due to discrete sampling of (ξ, τ) plane. Plot generated from MCF illustrated in Figure (3.1).

range of velocities that get mapped to the same integer tuple (n,m) is,

$$v_{\mathrm{nm}} \in \frac{f_\tau}{f_\xi} \frac{1}{\mathrm{m}} [\frac{2\mathrm{n}-1}{2}, \frac{2\mathrm{n}+1}{2}] \tag{3.34}$$

and represents the uncertainty in an estimate of v from a single measurement of $(\mathrm{n}_{max}, \mathrm{m})$. In practice, we have some number N of measured integer tuples of $(\mathrm{n}_{max}, \mathrm{m})$ as illustrated in Figure (3.10). The true value of v must lie within the corresponding intersection of all N distributions given by the expression in (3.34), i.e. the largest velocity range for which all distributions completely overlap. Let $p_{\mathrm{n}}(v)$ denote the distribution obtained by finding the intersection of N distributions given by (3.34). In this paper the mean value of $p_{\mathrm{n}}(v)$ is taken as an estimate of v and the width of the distribution as the uncertainty in the estimate.

3.4   Measurements of Ionospheric Drifts at Kodiak

Measurements of ionospheric drifts evaluated from data recorded by the Kodiak Super-DARN during two short time intervals on 17 May 2014 are presented here. The radar operation is discussed below before presenting the drift measurements.

51

3.4.1 Radar Operation and Signal Conditioning

The Kodiak SuperDARN radar consists of a collinear array of 16 log periodic antenna spaced by 15.24 m. The phased array has a narrow azimuth beamwidth of $\sim 7°$ at 10 MHz but a broad elevation beamwidth. The geographic coordinates of the radar are $[57.62°, -152.19°]$ with boresite oriented 30° from North. During normal operation the radar scans through 16 beam directions separated by 3.24°, collecting measurements from a single beam direction for a period of 7 s. During the observation periods presented here the radar ran a special operating mode in which a $N = 15$ pulse sequence was transmitted with a fixed PRF of $f_\tau = 50$ Hz in a single beam direction with a fixed transmit frequency. A range resolution of 15 km was obtained by transmitting phase coded (5-bit Barker) pulses of duration $T_p = 500$ μs and sampling the received signal at $f_s = 10$ kHz. The raw in-phase (I) and quadrature (Q) low pass analytic received signal was recorded at each antenna element in the radar array.

Prior to evaluating the MCF for a particular pulse sequence and range gate, the phase coding and beamforming during transmit were removed from the raw I/Q time series at each antenna by convolving with the Barker phase code and adding a phase shift specific to the beam direction and antenna element. Note that the addition of a phase shift to remove the effects of beamforming has no bearing on the $|\Gamma(\xi, \tau)|$ and simply projects the actual radar geometry into that depicted in Figure (3.3) where the radar is perpendicular to the illuminated area. The MCF in (3.1) was evaluated in discrete form as,

$$\Gamma(n, m) = \frac{1}{(L-n)(N-m)} \sum_{i=0}^{L-n-1} \sum_{j=0}^{N-m-1} E_i(j) E_{i+n}^*(j+m) \tag{3.35}$$

where $E_i(j)$ is the (complex) analytic signal observed at antenna element i after transmit pulse j for a given range cell, L is the number of spatial samples, and N is the number of time delay samples. Here (L, N) corresponding to the number of antenna elements in the array and the number of pulses in a transmit sequence so that $L = 16$ and $N = 15$. The

value obtained in (3.35) was then coherently integrated over a period of ≈ 5 s (corresponding to 12 transmit sequences) to reduce the effect of Gaussian noise on $|\Gamma(n, m)|$. A transverse velocity v was then estimated from cross-sections of the normalized $|\Gamma(n, m)|$ as described in section (3.3).

3.4.2 Measurements

During both observation periods ground scatter was observed at ranges gates around 900 km in range. The discrete MCF was evaluated as described above and then a transverse velocity estimated according to the method given in section (3.3). Figures (3.11) and (3.12) illustrate measured and fitted MCF's at a sequence of three gates around 900 km in range from one 5 s period in both observation intervals.
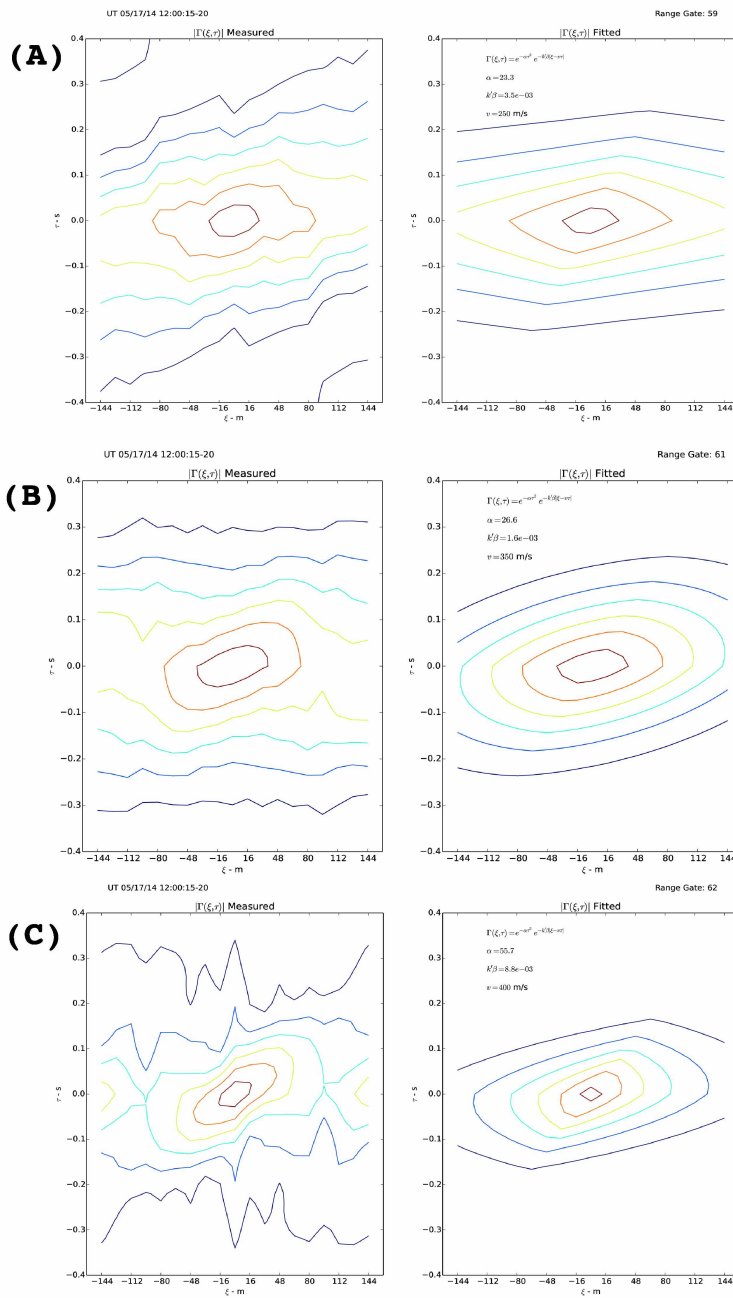
Figure 3.11: Examples of the measured (left) and fitted (right) MCF's at three different range gates where ground scatter was observed during the UT 2014 May 17 12:00:15-12:00:20 observation period. The form of the MCF and best fit parameter values are annotated on the plots on the right.
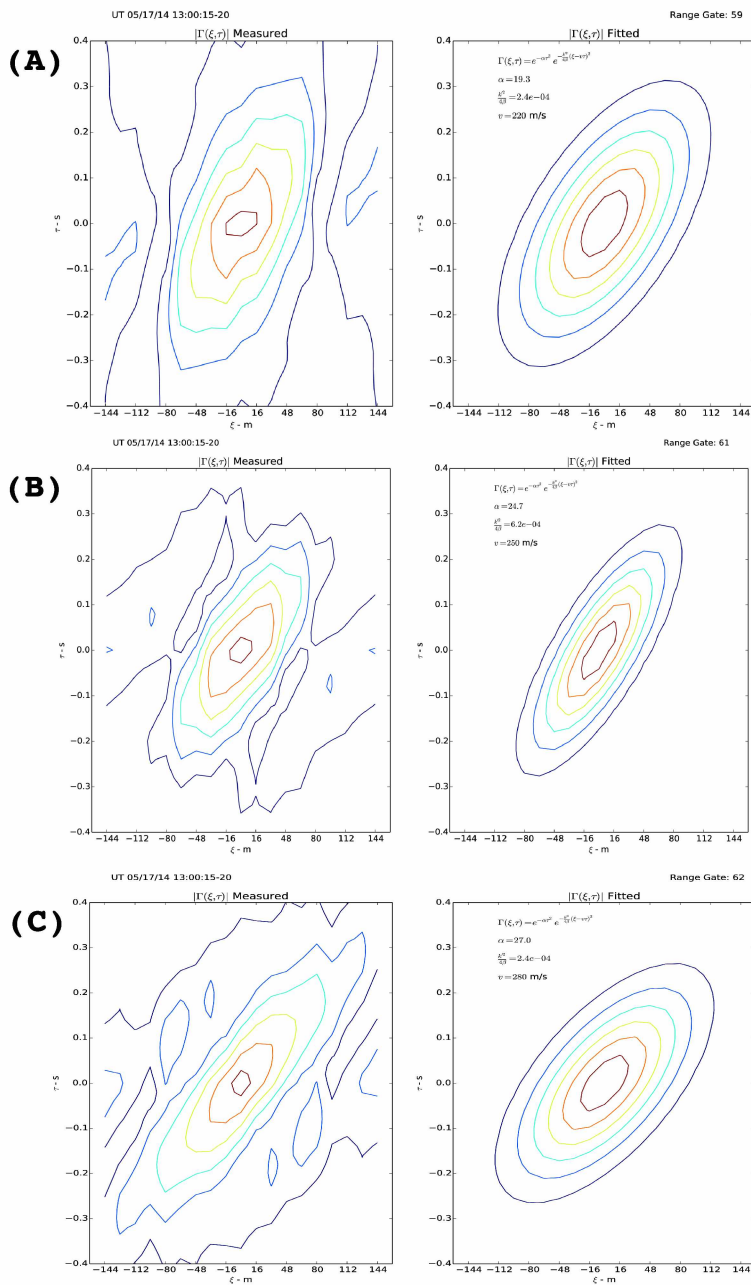
Figure 3.12: Examples of the measured (left) and fitted (right) MCF's at three different range gates where ground scatter was observed during the UT 2014 May 17 13:00:15-13:00:20 observation period. The form of the MCF and best fit parameter values are annotated on the plots on the right.

Note the form of the fitted MCF and parameter values annotated in the plots on the right hand sides of Figures (3.11) and (3.12) were determined from the $|\Gamma(\xi, 0)|$ and $|\Gamma(0, \tau)|$ cross-sections as described in section (3.2.5). As illustrated, larger velocities and an exponential ξ dependence were observed during the first period and smaller velocities with a Gaussian ξ dependence during the second period. We do not know why the ξ dependence of the MCF changed between the periods but note that both the ionosphere and consequently the illuminated area are unlikely to be exactly the same between observations. We expect that changes in the ionosphere and/or the illuminated area produced preferential scattering into certain angles so that the received angular power spectrum $|F(S)|^2$ and it's Fourier pair $|\Gamma(\xi)|$ are different between the two measurement intervals. Figure (3.13) illustrates the derived velocities at all ranges during both observation periods in the form of range-time-velocity plots.
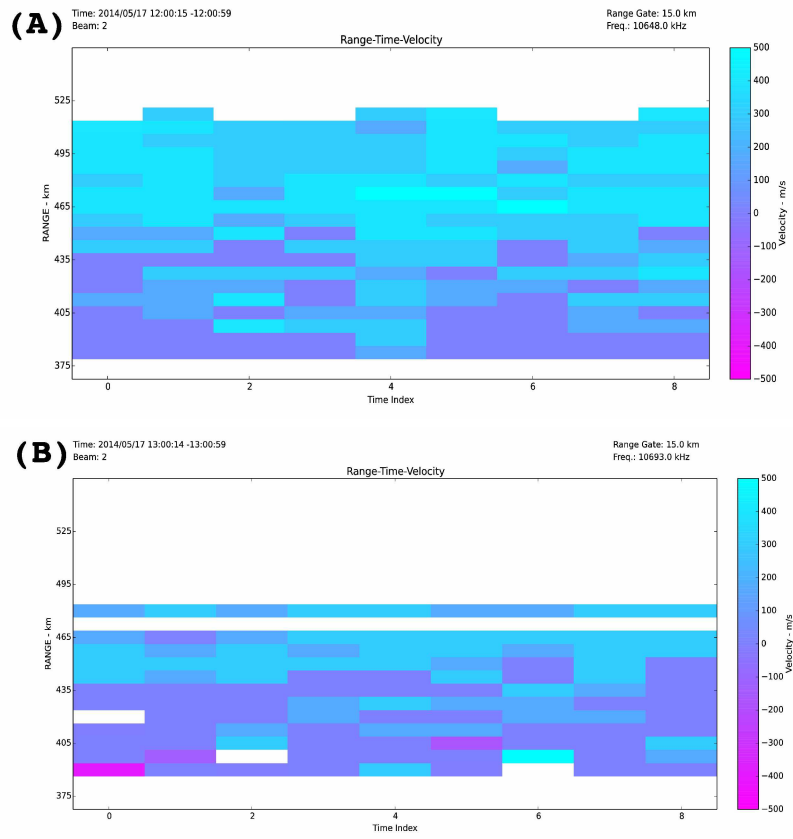
Figure 3.13: Range-time-velocity (RTV) plots during (A) UT May 17 2014 12:00:15-12:00:59 and (B) UT May 17 2014 13:00:14-13:00:59.
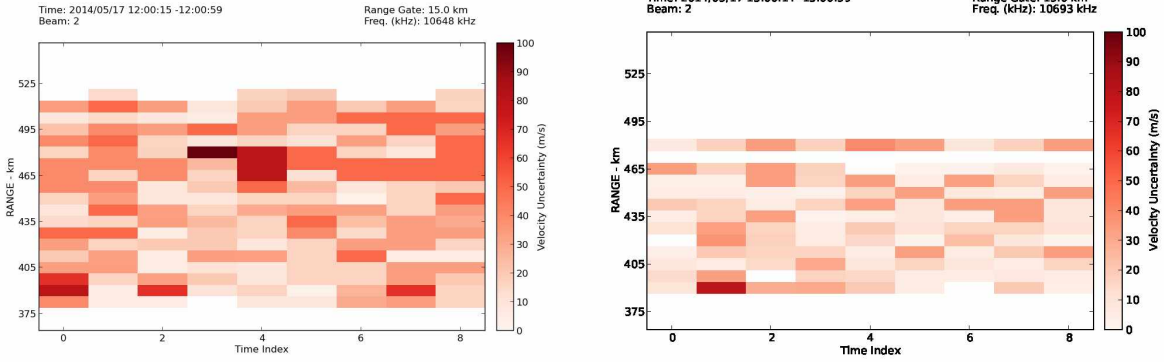
(a) Velocity uncertainty during UT May 17 2014 12:00:15-12:00:59

(b) Velocity uncertainty during UT May 17 2014 13:00:15-13:00:59

Figure 3.14: Velocity error bounds due to discretization of $|\Gamma(\xi, \tau)|$ as discussed in section 3.3.

Note in Figure (3.13) that the horizontal time axis indices occur in ~ 5 s increments and that the range corresponding to a given velocity measurement is half the range of the ground clutter cell from which the velocity was derived. The uncertainty of the velocity measurements of Figure (3.13) due to the discretization of $|\Gamma(\xi, \tau)|$ as discussed in section (3.3) is depicted in Figure (3.14). In general, Figure (3.14) demonstrates that the velocity uncertainty is of the order ± 50 m/s.

Finally, Figure (3.15) illustrates geographic plots of the derived drift vectors averaged over the entire ~ 45 s observation periods. In addition to the Kodiak derived drift measurements, Figure (3.15) depicts drifts measured by digisondes in Alaska at Gakona ($[62.38°, -145.0°]$) and Eielson AFB ($[64.66°, -147.07°]$)[*Reinisch and Galkin*, 2011]. The digisonde drift measurements are several hundred kilometers away from the location of our drift measurements and so do not provide an ideal comparison. As illustrated in Figure (3.15), the Eielson drift measurement had a magnitude on the order of 300 m/s during both observation periods and a West to East drift direction, both of which are consistent with the drifts derived from the Kodiak radar. On the other hand, the Gakona digisonde measured a comparitively small drift velocity magnitude on the order of ~ 30 m/s during both periods. During the first period at 12:00 UT there is a blanketing sporadic E layer evident in ionograms at Gakona. The
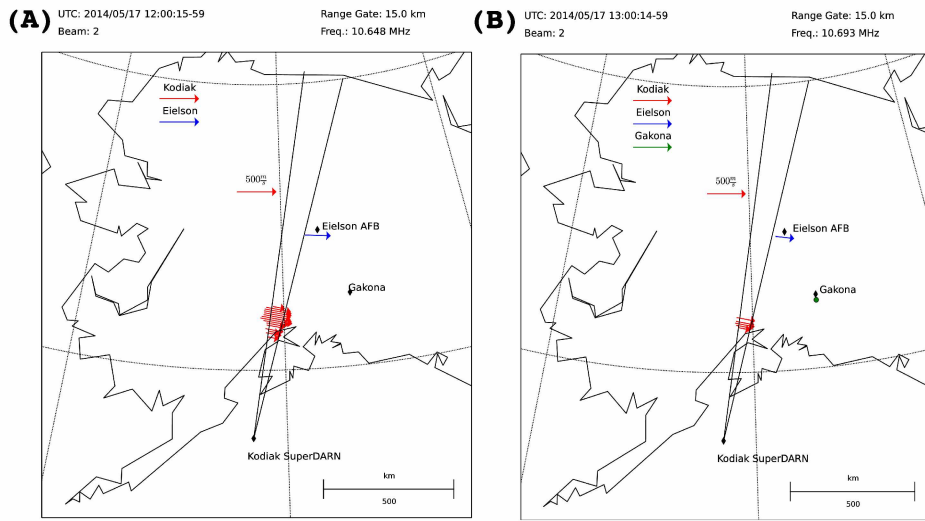
Figure 3.15: Ionospheric drifts evaluated during time periods (A) UT May 17 2014 12:00:15-12:00:59 and (B) UT May 17 2014 13:00:15-13:00:59 plotted over Alaska as measured by the Kodiak SuperDARN. The ionospheric drift measured by digisondes at Gakona and Eielson AFB is also annotated. The Eielson drift measurements in (A) and (B) were taken at 11:53:00 and 12:53:00 UT. There is no usable Gakona drift measurement in (A) due to the presence of a blanketing sporadic E layer. The Gakona drift measurement in (B) was taken at 13:04:25 UT.

drift derived by Gakona at this time is that of the sporadic E layer rather than the F region and so the discrepancy is not surprising. However, during the second observation period at 13:00 UT there is no sporadic E-layer present in ionograms and the measured drift at this point is evidently that of the F-layer. While the Gakona drift measurement at 13:00 UT is inconsistent with the drifts derived by the Kodiak radar it is also inconsistent with the drift measured at Eielson. As the location of the Gakona drift measurement is several hundred kilometers from both the Eielson and Kodiak drifts we don't believe the discrepancy is conclusive of an error in the method presented here. Another possible source of validation for the drift measurements presented here would be the SuperDARN convection model. However, only two radars (Kodiak and Christmas Valley West) have the geographic region in question within their field-of-view and neither recorded significant ionospheric back scatter during the observation periods which renders the SuperDARN convection model inconclusive.

3.5 Discussion

As noted in section (3.4.2), we currently lack conclusive evidence in the form of overlapping observations for the drift measurements presented here. We are currently in the process of collecting more data in the hope of obtaining drift measurements that overlap with either a digisonde or a region of significant ionospheric backscatter such that the SuperDARN convection model may be used for comparison. However, this same obstacle also illustrates the potential use of the method, which is to provide an additional tool to fill in the gaps in convection plots generated from overlapping measurements of line-of-sight plasma velocity. Another potential idea we are exploring is estimating the scale size of the electron density irregularities from $\Gamma(\xi, \tau)$. Specifically, as discussed in section (3.2.2) the plane wave scattered in direciton S_i contains weak side wave contributions whose Doppler shift differs from that of the undeviated component. The width $\Delta\omega$ of the Doppler spectrum should then be an indication of the angular width ΔS over which the ionosphere scatters an incident plane wave. If we were to assume a form of the side wave power spectrum $|F(S)|^2$ such as that in (3.8) we can estimate a density deviation scale size ξ_0 by noting that the width $\Delta\tau$ of $\Gamma(0, \tau)$ is inversely related $\Delta\omega$.

3.6 Conclusion

Measurements of ground scatter targets made by the Kodiak SuperDARN radar illustrate that the spatial distribution of the incident electric field often appears to move coherently across the radar aperture. Diffraction theory can be applied to demonstrate that this behavior is a product of transverse ionospheric motion between the radar and the illuminated area of ground. A general expression for the observed mutual coherence function was developed and used to derive a method of evaluating the transverse ionospheric drift. Ionospheric drifts evaluated using this technique were presented for two short observation periods at Kodiak.

4 MV-SAP: Preserving Angle-Doppler Coupled Clutter

4.1 Introduction

Sky wave over-the-horizon radar (OTHR) systems use the ionosphere as a mirror to illuminate targets beyond the horizon [*Skolnik*, 2008, Ch. 20]. These systems must be capable of detecting targets in the presence of backscatter from the surface of the Earth (either terrain or the sea) termed ground clutter and often radio frequency interference (RFI) from other users of the HF band [*Fabrizio*, 2013, Ch.4], [*Leong*, 1999]. In addition, high-latitude OTHR systems must contend with Bragg scatter from ionospheric density irregularities termed auroral clutter [*Choi et al.*, 1991; *Ravan et al.*, 2012].

An effective signal processing scheme that mitigates RFI and clutter to improve target detection requires knowledge of the characteristics of RFI and clutter in the dimensions of range, Doppler, and incidence angle. RFI in OTHR systems is typically modeled as incoherent with a uniform spectral density over the receiver bandwidth and so contaminates the entire range and Doppler domains [*Fabrizio*, 2013, Ch. 10]. In the angular domain, RFI occupies a small number of incidence angles that slowly vary over the observation period [*Fabrizio et al.*, 1998]. Ground clutter is generally broad in the angular domain and well resolved in the Doppler domain and at high-latitudes there is evidence of coupling between these dimensions [*Riddolls*, 2014; *Theurer and Bristow*, 2017]. The characteristics of auroral clutter depend on the state of the ionosphere during the period of observation [*Ravan et al.*, 2012]. However, measurements at high-latitude and models often feature a narrower angular width but broader Doppler width than ground clutter as well as coupling between the domains related to an ionospheric drift velocity transverse to the beam direction [*Riddolls*, 2014; *Ravan and Adve*, 2013]. Both auroral and ground clutter may be non-stationary in range as the echoes originate from physically distinct volumes or surfaces which may have dissimilar scattering properties. Further, the spectral characteristics of the received signal are shaped by the propagation path through the ionosphere and so echoes from different

61

range gates (different propagation paths) may be expected to be non-stationary [*Vallières et al.*, 2004].

Given the signal characteristics described above, one approach to jointly mitigating both RFI and clutter is Space-Time Adaptive Processing (STAP) in the slow-time and space dimensions [*Ward*, 1994]. The main obstacle to this approach is obtaining a sufficient amount of training data to accurately estimate the auroral and ground clutter covariance matrices which are non-stationary in range [*Ravan et al.*, 2011]. Variants of STAP such as FFA have been derived that drastically reduce the required training data and have been used to successfully mitigate auroral clutter but not all OTHR systems and/or ionospheric conditions may yield a sufficient number of statistically homogeneous clutter snapshots to apply this technique [*Saleh et al.*, 2016; *Ravan et al.*, 2011]. An alternative to the joint mitigation of RFI and clutter is a cascaded approach where RFI is first mitigated by adaptive spatial processing (SAP) and clutter subsequently by Doppler processing [*Fabrizio et al.*, 2004]. Besides avoiding the clutter training support issue, this type of processing may also be appropriate if the clutter or rather the Doppler spectrum of the clutter is itself a data product of interest as in [*Vallières et al.*, 2004].

Each stage of processing in a cascaded processing scheme must be designed with consideration of the effect of the current stage of processing on latter stages. The consideration involved in a SAP-Doppler processing scheme is best illustrated by formulating the SAP problem. Consider an OTHR that transmits N consecutive pulses at a fixed pulse-repitition-frequency (PRF) of f_t Hz and samples the downconverted, match-filtered received signal across M antennas K times each pulse interval at the rate f_r Hz. The received data during the coherent-processing-interval (CPI) can be formatted as an $M \times N \times K$ cube of complex samples corresponding to the dimensions of space, slow-time, and range (or fast-time) respectively. The spatial snapshot $\mathbf{z}_{nk} \in \mathcal{C}^{M \times 1}$ at a particular slow time sample n and range gate k can be expressed in general as,

$$\mathbf{z}_{nk} = \mathbf{t}_{nk} + \mathbf{y}_{nk} + \mathbf{i}_{nk} + \mathbf{n}_{nk}, \tag{4.1}$$

where $\mathbf{t}_{nk}$, $\mathbf{y}_{nk}$, $\mathbf{i}_{nk}$, and $\mathbf{n}_{nk}$ denote target, clutter, interference, and noise signals respectively.

Standard SAP involves generating the scalar time sequence $z[n] = \mathbf{w}^H \mathbf{z}_{nk}$ where the vector $\mathbf{w}$ is the solution to the constrained optimization problem,

$$\mathbf{w} = \operatorname*{argmin}_{\mathbf{w}} \mathbf{w}^H \mathbf{R_{ii}} \mathbf{w}$$
$$\text{subject to } \mathbf{w}^H \mathbf{t}(\theta) = 1.0, \tag{4.2}$$

where $\mathbf{R_{ii}} = \mathcal{E}\{\mathbf{i}_{nk}\mathbf{i}_{nk}^H\}$ is the ensemble averaged interference spatial covariance matrix and $\mathbf{t}(\theta)$ is the target steering vector. As described previously, the interference spatial covariance matrix $\mathbf{R_{ii}}$ varies with slow-time index n as the interference direction of arrival varies over the CPI. Our goal then is to find the *sequence* of weight vectors $\mathbf{w}_n$ that minimize the inner product $\mathbf{w}_n^H \mathbf{i}_{nk}$ $\forall$ n within a CPI. Further, the sequence $\mathbf{w}_n$ should yield a scalar clutter signal $y[n] = \mathbf{w}_n^H \mathbf{y}_{nk}$ whose Doppler spectrum is indistinguishable from that produced using the fixed weight vector $\mathbf{w}_0$ for all slow-time samples. This additional constraint is necessary to prevent smearing in the Doppler spectrum that may obscure targets during subsequent Doppler processing.

The two most promising solutions we are aware of to the problem presented above include stochastically-constrained SAP (SC-SAP) and time-varying SAP (TV-SAP) [*Abramovich et al.*, 1994, 1998; *Fabrizio et al.*, 2004]. In [*Abramovich et al.*, 1994, 1998] the authors demonstrate a general theoretical solution provided that the clutter may be accurately represented as a multivariate, autoregressive (MVAR) process [*Marple*, 1986, Ch. 15, pp. 394-409]. However, a practical implementation is stymied by a lack of knowledge of MVAR model parameters. This obstacle is sidestepped in [*Abramovich et al.*, 1994, 1998] by restricting attention to the *scalar* MVAR clutter model, a special case for which knowledge of the model

parameters is superfluous. It is this specialized solution that will be referred to here by the name SC-SAP. A scalar MVAR model implies that the clutter signal is space-time separable, a condition that has been empirically demonstrated in [*Abramovicht et al.*, 1996], [*Fabrizio*, 2013, Ch. 7] for quiet mid-latitude ionospheric conditions. However, as mentioned previously the auroral and ground clutter observed at high-latitudes may feature angle-Doppler coupling and in that case is non-separable in space-time. In the event of angle-Doppler coupling, implementing SC-SAP *does* require an accurate estimation of the MVAR model order and parameters which is a non-trivial task. Beyond this obstacle, SC-SAP requires updating the weight vector during every slow-time sample which is both computationally intensive and susceptible to error accumulation [*Fabrizio et al.*, 2004].

TV-SAP is an alternative algorithm presented in [*Fabrizio et al.*, 2004] with two distinguishing features. First, the adaptive weight vector is updated in slow-time every Q samples where Q is the CPI subinterval over which the interference is spatially stationary. Second, the clutter Doppler spectrum is preserved in TV-SAP by constraining changes in the weight vector to be orthogonal to the clutter subspace in the current CPI subinterval. The fidelity with which TV-SAP reproduces the clutter Doppler spectrum appears to depend mainly on the correct estimation of the clutter subspace rank. Further, the slower rate of weight vector updates dramatically reduces the computational burden of TV-SAP in comparison to SC-SAP [*Fabrizio et al.*, 2004]. TV-SAP doesn't explicitly rely on a scalar MVAR model but instead assumes that the clutter during any particular CPI subinterval is well modeled by a small number of steering vectors. One can analytically demonstrate that while this assumption produces excellent performance for a scalar MVAR process, it is inherently ill-suited to more general MVAR processes and results in a performance ceiling below what one might otherwise expect.

The inherent and practical obstacles of TV-SAP and SC-SAP motivate the derivation of a new SAP algorithm in this paper termed MV-SAP that incorporates key features from both. Following SC-SAP, MV-SAP contains weight vector optimization constraints that are

based on the ensemble averaged clutter properties rather than quasi-instantaneous clutter characteristics as in TV-SAP. However, MV-SAP minimizes weight vector updates to the period over which the interference is stationary in the same fashion as TV-SAP. The results in this paper demonstrate that for a coupled clutter process based on measurements made at high-latitudes MV-SAP is capable of providing better performance than TV-SAP. It should be noted that all of the SAP algorithms discussed in this paper are appropriate for mitigating RFI that occurs in the sidelobes of the radar and cannot suppress mainbeam interference. However, while not addressed in this paper MV-SAP may be extended to fast-time STAP in the same fashion as TV-STAP and SC-STAP which mitigate main beam interference using redundancy in the interference signal in the fast-time dimension that exists due to multipath [*Fabrizio*, 2013, Ch. 11], [*Abramovich et al.*, 1998].

This dissertation section is organized as follows. In Section II we present some background MVAR process theory, the problem of Doppler spreading during SAP, the performance ceiling of TV-SAP, and the theoretical basis for the new algorithm MV-SAP. Section III discusses the simulation set up used in this paper. Simulation results are presented in Section IV that verify the analysis in Section II and quantify the performance of MV-SAP. For perspective, the performance of MV-SAP is compared with TV-SAP which generally outperforms SC-SAP while avoiding the obstacles associated with that algorithm.

4.2 Theory

4.2.1 MVAR Properties

In this section we briefly detail some properties of MVAR processes important for the following discussion and refer the reader to [*Marple*, 1986, Ch. 15] for a more detailed treatment. Let $\mathbf{y}_n \in \mathcal{C}^{M \times 1}$ denote a general MVAR process described by the recursive equation,

$$\mathbf{y}_n = -\sum_{l=1}^{P} \mathbf{A}_l \mathbf{y}_{n-l} + \boldsymbol{\xi}_n, \tag{4.3}$$

where P denotes the model order, $\mathbf{A}_l$ are $M \times M$ autoregressive coefficient matrices, and $\boldsymbol{\xi}_n$ is a white noise process. $\boldsymbol{\xi}_n$ has the covariance property,

$$\mathbf{R}_m^{\xi\xi} = \mathcal{E}\{\boldsymbol{\xi}_{n+m}\boldsymbol{\xi}_n^H\} = R^{\xi\xi}\delta[m], \tag{4.4}$$

where $R^{\xi\xi}$ is Hermitian. An expression equivalent to (4.3) is the convolution,

$$\mathbf{y}_n = \sum_{k=0}^{\infty} \mathbf{H}_k \boldsymbol{\xi}_{n-k} = \mathbf{H}_n * \boldsymbol{\xi}_n, \tag{4.5}$$

where $\mathbf{H}_n$ is the multichannel impulse response matrix. The summation in (4.5) is restricted to $[0, \infty)$ because $\mathbf{H}_n$ is causal, i.e. $\mathbf{H}_n = 0\ \forall n < 0$. The relationship between (4.3) and (4.5) is illustrated by taking the multichannel z-transform of (4.3), $\mathcal{Z}\{\cdot\}$, given by,

$$\mathbf{Y}(z) = \sum_{k=-\infty}^{\infty} \mathbf{y}_k z^{-k} = \mathbf{A}^{-1}(z)\boldsymbol{\xi}(z), \tag{4.6}$$

where $\mathbf{A}^{-1}(z)$ is the inverse of the matrix,

$$\mathbf{A}(z) = \mathbf{I} + \sum_{l=1}^{P} \mathbf{A}_l z^{-l}. \tag{4.7}$$

From (4.6) and the property of convolution under the $\mathcal{Z}\{\cdot\}$ operator we note that $\mathbf{H}_n = \mathcal{Z}^{-1}\{\mathbf{A}^{-1}(z)\}$.

The relationship between $\mathbf{R}_m^{\mathbf{yy}}$ and $\mathbf{R}_m^{\xi\xi}$ is given by

$$\mathbf{R}_m^{\mathbf{yy}} = \mathbf{H}_m * \mathbf{R}_m^{\xi\xi} * \mathbf{H}_{-m}^H. \tag{4.8}$$

The power spectral density (PSD) matrix $\mathbf{P}^{\mathbf{yy}}(f)$ defined as $\mathcal{Z}\{\mathbf{R}_m^{\mathbf{yy}}\}\big|_{z=e^{-j2\pi fmT}}$ can now be expressed using the relationships in (4.4)-(4.8) as,

$$\mathbf{P^{yy}}(f) = \mathbf{H}(f)\mathbf{P}^{\xi\xi}(f)\mathbf{H}^H(f)$$

$$= \mathbf{A^{-1}}(f)R^{\xi\xi}\mathbf{A}^{-H}(f), \tag{4.9}$$

where $^{-H}$ denotes Hermitian transpose of the inverse.

In the particular case of a *scalar* MVAR process a number of simplifications can be made to the expressions above. A scalar MVAR process is one in which the coefficient matrices in (4.3) have the form $\mathbf{A}_l = \alpha_l \mathbf{I}$. In this case, (4.7) can be expressed as,

$$\mathbf{A}(z) = (1 + \sum_{l=1}^{P} \alpha_l z^{-l})\mathbf{I} = A(z)\mathbf{I} \tag{4.10}$$

so that the power spectral density simplifies to,

$$\mathbf{P^{yy}}(f) = \frac{1}{|A(f)|^2}R^{\xi\xi}. \tag{4.11}$$

The covariance sequence corresponding to (4.11) is,

$$\mathbf{R}_m^{\mathbf{yy}} = \mathcal{Z}^{-1}\{\frac{1}{A(z)A^*(1/z^*)}\}R^{\xi\xi} = r[m]R^{\xi\xi}, \tag{4.12}$$

where the space-time separability is evident in the factorization of $\mathbf{R}_m^{\mathbf{yy}}$ into the scalar function of time $r[m]$ and the constant spatial covariance matrix $R^{\xi\xi}$.

4.2.2   Doppler Spreading

At this point we turn to an analytical investigation of the problem of Doppler spreading. This investigation will provide us with the means of constraining variations in the adaptive weight vector sequence $\mathbf{w}_n$ to avoid Doppler spreading and also help illustrate key differences between scalar and general MVAR processes. Let $y[n]$ denote the scalar output sequence obtained by filtering the vector sequence $\mathbf{y}_n$ at a particular range gate with the adaptive

weight vector sequence $\mathbf{w}_n$ where both $\mathbf{y}_n$ and $\mathbf{w}_n$ are wide-sense-stationary Gaussian random processes. The correlation sequence of $y[n]$ is given by,

$$r_y[m] = \mathcal{E}\{y[n+m]y^*[n]\}$$
$$= \mathcal{E}\{\mathbf{w}_{n+m}^H \mathbf{y}_{n+m} \mathbf{y}_n^H \mathbf{w}_n\}. \tag{4.13}$$

The inner products in (4.13) can each be expanded using (4.5) as follows,

$$\mathbf{w}_n^H \mathbf{y}_n = \sum_{u=0}^{\infty} \mathbf{w}_n^H \mathbf{H}_u \boldsymbol{\xi}_{n-u}$$
$$= \sum_{u=0}^{\infty} \sum_{i=1}^{M} \sum_{j=1}^{M} \mathbf{w}_{n,i}^* \mathbf{H}_{u,ij} \boldsymbol{\xi}_{n-u,j}, \tag{4.14}$$

where the second subscript refers to an element of the given vector or matrix, i.e. $\mathbf{H}_{u,ij}$ refers to the (i,j) entry of $\mathbf{H}_u$. It follows that (4.13) can be re-written as,

$$r_y[m] = \sum_{uv=0}^{\infty} \sum_{ijkl=1}^{M} \mathbf{H}_{u,ij} \mathbf{H}_{v,kl}^H \cdot$$
$$\mathcal{E}\{\mathbf{w}_{n+m,i}^* \mathbf{w}_{n,l} \boldsymbol{\xi}_{n+m-u,j} \boldsymbol{\xi}_{n-v,k}^*\}. \tag{4.15}$$

The fourth order moment in (4.15) can be expressed as a sum of lower order moments [*Stoica and Moses*, 2005]. We assume here that $\mathbf{y}[n]$ is a zero-mean process and that the cross correlation $\mathcal{E}\{\mathbf{w}_{n,i}\boldsymbol{\xi}_{m,j}\} = 0$ for all (n,m,i,j), an assumption that follows from the fact that the weight vector changes are driven by an independent interference process. In this case, (4.15) further reduces to,

68

$$
\begin{aligned}
r_y[m] &= \sum_{uv=0}^{\infty} \sum_{ijkl=1}^{M} \mathbf{H}_{u,ij} \mathbf{H}_{v,kl}^{H} \cdot \\
&\quad \mathcal{E}\big\{\mathbf{w}_{n+m,i}^{*} \mathbf{w}_{n,l}\big\} \mathcal{E}\big\{\boldsymbol{\xi}_{n+m-u,j} \boldsymbol{\xi}_{n-v,k}^{*}\big\} \\
&= \sum_{il=1}^{M} \mathcal{E}\big\{\mathbf{w}_{n+m,i}^{*} \mathbf{w}_{n,l}\big\} \cdot \\
&\quad \sum_{uv=0}^{\infty} \sum_{jk=1}^{M} \mathbf{H}_{u,ij} \mathbf{H}_{v,kl}^{H} \mathbf{R}_{m-u+v,jk}^{\xi\xi} \\
&= \sum_{il=1}^{M} \mathcal{E}\big\{\mathbf{w}_{n+m,i}^{*} \mathbf{w}_{n,l}\big\} \mathbf{R}_{m,il}^{\mathbf{yy}} \\
&= \mathcal{E}\big\{\mathbf{w}_{n+m}^{H} \mathbf{R}_{m}^{\mathbf{yy}} \mathbf{w}_{n}\big\}.
\end{aligned}
\tag{4.16}
$$

The power spectral density corresponding to (4.16) is,

$$
\begin{aligned}
P_y(f) &= \sum_{m=-\infty}^{\infty} r_y[m] e^{-j2\pi mfT} \\
&= \sum_{m=-\infty}^{\infty} \sum_{il=1}^{M} \mathcal{E}\big\{\mathbf{w}_{n+m,i}^{*} \mathbf{w}_{n,l}\big\} \mathbf{R}_{m,il}^{\mathbf{yy}} \, e^{-j2\pi mfT} \\
&= \sum_{il=1}^{M} \sum_{m=-\infty}^{\infty} \mathbf{R}_{m,il}^{\mathbf{ww}} \mathbf{R}_{m,il}^{\mathbf{yy}} \, e^{-j2\pi mfT} \\
&= \sum_{il=1}^{M} \mathbf{P}_{il}^{\mathbf{ww}}(f) * \mathbf{P}_{il}^{\mathbf{yy}}(f).
\end{aligned}
\tag{4.17}
$$

In the special case of constant beamforming the $\mathcal{E}\{\,\cdot\,\}$ operator can be eliminated from the quadratic expression in (4.16) and the spectral density is readily seen to be $P_y(f) = \mathbf{w}^H \mathbf{P}^{\mathbf{yy}}(f)\mathbf{w}$ which is simply a weighted summation of auto and cross spectral densities. In contrast, (4.17) demonstrates that in the general case we have a summation of *convolved* auto and cross spectral terms which results in the observed Doppler spreading.

The expression in (4.16) implicitly contains the necessary condition to avoid Doppler spreading. Specifically, $\mathbf{w}_{n+m}$ and $\mathbf{w}_n$ can differ without affecting $r_y[m]$ so long as that

difference $(\mathbf{w}_{n+m} - \mathbf{w}_n)$ is orthogonal to $\mathbf{R}_m^{yy}\mathbf{w}_n$. In particular, note that if $\mathbf{y}_n$ is a scalar MVAR process, (4.16) simplifies to,

$$r_y[m] = r[m]\mathcal{E}\big\{\mathbf{w}_{n+m}^H R^{\xi\xi}\mathbf{w}_n\big\}, \tag{4.18}$$

from which it is apparent that Doppler spreading may be avoided by constraining changes in $\mathbf{w}_{n+m}$ to be orthogonal to $R^{\xi\xi}\mathbf{w}_n$. This is an alternative derivation of the TV-SAP algorithm, which may be more easily recognized by noting that the columnspace of $R^{\xi\xi}$ for a deterministic clutter signal $\mathbf{y}_n = \mathbf{V}\mathbf{p}_n$ is the same as the columnspace of the steering vector matrix $\mathbf{V}$, i.e. $R^{\xi\xi} = \mathbf{V}\mathcal{E}\big\{\mathbf{p}_n\mathbf{p}_n^H\big\}\mathbf{V}^H$.

4.2.3 Limitations of TV-SAP applied to general MVAR clutter

The TV-SAP algorithm is based on the approximation that the clutter signal over a window of Q samples is deterministic. Given this approximation, any L consecutive snapshots $\mathbf{y}_n, \mathbf{y}_{n+1}, \ldots, \mathbf{y}_{n+L}$ may be used as a basis for a clutter space of rank L. Suppose for the moment that the clutter signal is an MVAR process that is approximately unit rank over a window of Q samples. The error associated with using snapshot $\mathbf{y}_n$ as an estimate of snapshot $\mathbf{y}_{n+L}$ is,

$$\mathbf{e}_L = \mathbf{y}_{n+L} - \mathbf{y}_n. \tag{4.19}$$

The error spatial covariance matrix $\mathbf{P}^{ee}$ is consequently,

$$\mathbf{P}^{ee} = \mathcal{E}\big\{\mathbf{e}_L\mathbf{e}_L^H\big\}$$
$$= 2\mathbf{R}^{yy}[0] - \mathbf{R}^{yy}[L] - \mathbf{R}^{yy}[-L]. \tag{4.20}$$

Now for the scalar MVAR case we can substitute (4.12) to reduce (4.20) to,

70

$$\mathbf{P^{ee}} = (2r[0] - r[L] - r[-L])R^{\xi\xi} = \lambda R^{\xi\xi}, \tag{4.21}$$

where $\lambda = 2r[0] - r[L] - r[-L]$ is a scalar. As $\mathbf{P^{ee}}$ is a scalar multiple of $R_{\xi\xi}$, it necessarily has the same columnspace. The important implication of this result is that the error $\mathbf{e}_L$ will not be spread by weight vector adaptations that are constrained to be orthogonal to $R^{\xi\xi}$, i.e. TV-SAP. However, the matrices $\mathbf{R^{yy}}[m]$ are only parallel to $R^{\xi\xi}$ for all m in the scalar MVAR case. In general, the coefficient matrices $\mathbf{A}_l$ successively rotate each sample of the random process with the result that the error covariance $\mathbf{P^{ee}}$ will not be parallel to $R^{\xi\xi}$ and thus $\mathbf{e}_L$ will be modulated by the TV-SAP weight vector adaptations.

4.2.4   Multivariate SAP (MV-SAP)

Given the foregoing analysis, it is worth returning to the expression in (4.16) for an alternative method of preserving the Doppler spectrum. Note that any covariance matrix $\mathbf{R}_m^{yy}$ can be expressed in terms of the singular value decomposition,

$$\mathbf{R}_m^{yy} = \mathbf{U}_m \mathbf{\Sigma}_m \mathbf{V}_m^H. \tag{4.22}$$

Following the philosophy of TV-SAP, we note that if $\mathbf{w}_{n+m}$ is constructed such that $(\mathbf{w}_{n+m} - \mathbf{w}_n)^H \mathbf{U}_m = 0$, then $r_y[m]$ will be unaffected. However, we desire $r_y[m]$ to be unaffected for *all* lags m and it is not immediately obvious that the columnspaces of $\mathbf{U}_m$ overlap for all m. Further, $L = \text{rank}(\mathbf{U}_m)$ needs to satisfy the condition $L \ll M$ for spatial processing to be effective.

First we investigate the properties of $\mathbf{U}_m$ versus lag m. Let $\mathcal{C}\{\cdot\}$ denote columnspace. From (4.11) it is clear that $\mathcal{C}(\mathbf{P^{yy}}(f))$ is the same for all frequencies f for a scalar MVAR process. On the other hand, angle-Doppler coupling indicates a linear relationship between direction-of-arrival and Doppler frequency, i.e. $\mathcal{C}(\mathbf{P^{yy}}(f_1)) \neq \mathcal{C}(\mathbf{P^{yy}}(f_2))$. Suppose we

71

take N_f samples of $\mathbf{P^{yy}}(f)$ over the range $[-1/2T, 1/2T]$ and denote the kth sample $\hat{\mathbf{P}}^{\mathbf{yy}}[k]$. The covariance sequence $\mathbf{R}^{\mathbf{yy}}_m$ is then approximated by the discrete Fourier transform,

$$\mathbf{R}^{\mathbf{yy}}_m = \frac{1}{N_f T} \sum_{k=0}^{N_f-1} \hat{\mathbf{P}}^{\mathbf{yy}}[k] e^{j2\pi km/N_f}. \tag{4.23}$$

Suppose each matrix $\hat{\mathbf{P}}^{\mathbf{yy}}[k]$ is close to unit rank so that it may be approximated as,

$$\hat{\mathbf{P}}^{\mathbf{yy}}[k] \simeq \sigma_k \mathbf{u}_k \mathbf{v}_k^H. \tag{4.24}$$

Substituting (4.24) into (4.23) yields,

$$\mathbf{R}^{\mathbf{yy}}_m = \hat{\mathbf{U}} \hat{\mathbf{\Sigma}} \hat{\mathbf{V}}^H, \tag{4.25}$$

where,

$$\hat{\mathbf{U}} = [\mathbf{u}_0 \ \mathbf{u}_1 \cdots \mathbf{u}_{N_f-1}]$$
$$\hat{\mathbf{\Sigma}} = \text{diag}\left\{ [\sigma_0 \ \sigma_1 e^{j2\pi k/N_f} \cdots \sigma_{N_f-1} e^{j2\pi k \frac{(N_f-1)}{N_f}}] \right\}$$
$$\hat{\mathbf{V}}^H = [\mathbf{v}_0 \ \mathbf{v}_1 \cdots \mathbf{v}_{N_f-1}]^H. \tag{4.26}$$

Expressions (4.25)-(4.26) demonstrate that $\mathbf{R}^{\mathbf{yy}}_m$ can be decomposed in terms of the *same* set of left singular vectors $\hat{\mathbf{U}}$ for all lags m. If $\hat{\mathbf{P}}^{\mathbf{yy}}[k]$ is in fact greater than unit rank, $\hat{\mathbf{U}}$ will have more columns but the fundamental result is unchanged.

Let us assume for the moment that $\text{rank}\left(\hat{\mathbf{U}}\right) = L$ where $L \ll M$. In addition, following the TV-SAP algorithm we'll divide the CPI into N_Q subintervals of Q slow-time samples each where Q is the period over which the interference is stationary. The multivariate SAP (MV-SAP) algorithm can be posed as the optimization problem,

$$\mathbf{w}_q = \underset{\mathbf{w}_q}{\operatorname{argmin}}\ \mathbf{w}_q^H \mathbf{R}_q^{\mathbf{ii}} \mathbf{w}_q$$

$$\text{subject to: } \mathbf{C}\mathbf{w}_q = \mathbf{f}, \tag{4.27}$$

where,

$$\mathbf{C} = [\mathbf{t}(\theta)\ \hat{\mathbf{U}}] = [\mathbf{t}(\theta)\ \mathbf{u}_0 \cdots \mathbf{u}_{L-1}]^H$$

$$\mathbf{f} = [1.0\ \mathbf{w}_0^H \mathbf{u}_0 \cdots \mathbf{w}_0^H \mathbf{u}_{L-1}]^T. \tag{4.28}$$

In (4.27)-(4.28) $\mathbf{t}(\theta)$ represents the ideal target steering vector, $[\mathbf{u}_0 \cdots \mathbf{u}_{L-1}]$ are the dominant L left singular vectors of the clutter covariance matrices $\mathbf{R}_m^{\mathbf{yy}}$, and the subscript q denotes the qth CPI subinterval. The well known solution to optimization problems of the form in (4.27) is,

$$\mathbf{w}_q = (\mathbf{R}_q^{\mathbf{ii}})^{-1} \mathbf{C}[\mathbf{C}^H (\mathbf{R}_q^{\mathbf{ii}})^{-1} \mathbf{C}]^{-1} \mathbf{f}. \tag{4.29}$$

The only remaining piece in implementing (4.29) is obtaining the dominant left singular vectors $[\mathbf{u}_0 \cdots \mathbf{u}_{L-1}]$ of $\mathbf{R}_m^{\mathbf{yy}}$. We assume here that the interference signal is incoherent and thus contaminates all range gates so that clutter only samples for evaluating $\mathbf{R}_m^{\mathbf{yy}}$ are unavailable. We do however have access to the instantaneous interference spatial covariance matrix $\mathbf{R}_q^{\mathbf{ii}}$ during the qth subinterval, and thus a means of estimating the interference steering vector(s) using DOA algorithms such as MUSIC [*Schmidt*, 1986]. Let $\mathbf{z}_{nk}$ denote the received array snapshot at slow-time sample n and range gate k while $[\hat{\mathbf{i}}_0 \cdots \hat{\mathbf{i}}_{P-1}]$ denote the $P \ll M$ interference unit steering vectors found using MUSIC or another technique. The corresponding clutter only signal is approximately

$$\mathbf{y}_{nk} \simeq \mathbf{z}_{nk} - \sum_{l=0}^{P-1} (\mathbf{z}_{nk}^{H} \hat{\mathbf{i}}_l) \hat{\mathbf{i}}_l. \tag{4.30}$$

Once clutter only samples have been obtained over a period of time the dominant left eigenvectors $[\mathbf{u}_0 \cdots \mathbf{u}_{L-1}]$ can be obtained from the SVD of any $\mathbf{R}_m^{\mathbf{yy}}$ with the simplest choice being $\mathbf{R}_0^{\mathbf{yy}}$ estimated as

$$\hat{\mathbf{R}}_0^{\mathbf{yy}} = \frac{1}{N_c} \sum_{i=0}^{N_c-1} \mathbf{y}_{ik} \mathbf{y}_{ik}^{H}. \tag{4.31}$$

Provided we choose $N_c \gg 2M$, $\hat{\mathbf{R}}_0^{\mathbf{yy}}$ will accurately approximate the asymptotic form of $\mathbf{R}_0^{\mathbf{yy}}$ [*Reed et al.*, 1974].

In summary, MV-SAP is performed on a per range gate basis as follows,

1. During the first D CPI subintervals where $DQ \gg 2M$:

    i Perform unconstrained SAP as given in (4.2)

    ii Obtain interference steering vectors via DOA algorithm

    iii Evaluate $\mathbf{y}_{nk}$ using (4.30)

2. Approximate $\mathbf{R}_0^{\mathbf{yy}}$ from (4.31).

3. Obtain $[\mathbf{u}_0 \cdots \mathbf{u}_{L-1}]$ from SVD.

4. Peform (4.29) for all remaining CPI subintervals.

MV-SAP exacts an upfront computational cost to obtain clutter only samples but subsequently costs the same as TV-SAP.

4.3   Simulation

The problem of Doppler spreading during SAP, the limitations of TV-SAP in the presence of angle-Doppler coupled clutter, and the proposal of a new algorithm termed MV-SAP

have been presented in the previous sections. In this paper the performance of MV-SAP is quantified and compared to TV-SAP through simulation. In this section, the properties of each term of $\mathbf{z}_{nk}$ in (4.1) and how they are generated in simulation are first discussed. In the derivation of MV-SAP, the existence of $L \ll M$ left singular vectors that span the coupled clutter covariance columnspace $\mathcal{C}\left(\mathbf{R}_m^{\mathbf{yy}}\right)$ for all m was assumed. In this section, the validity of this assumption is also evaluated using simulated coupled clutter whose covariance properties are based on observations made by a high-latitude radar [*Theurer and Bristow*, 2017].

4.3.1 Noise

The noise term $\mathbf{n}_{nk}$ is a multivariate white process defined by the covariance property,

$$\mathcal{E}\left\{\mathbf{n}_{nk}\mathbf{n}_{n'k'}^H\right\} = \delta_{nn'}\delta_{kk'}\sigma^2\mathbf{I}. \tag{4.32}$$

The noise signal for a $M \times N \times K$ data cube is thus generated by drawing $M \times N \times K$ independent and identically distributed (IID) complex samples from a zero-mean Gaussian distribution of variance σ^2.

4.3.2 Target

All SAP algorithms presented here contain a constraint $\mathbf{t}(\theta)^H\mathbf{w} = 1$ that "freezes" the beam pattern in the steer direction θ. However, there are no explicit constraints to prevent pattern fluctuations in directions other than θ and so it is of interest to investigate how robust a given SAP algorithm is to target mis-match. The target used in simulation here is thus a *sidelobe* target. The target is assumed to be a deterministic signal of the form,

$$\mathbf{t}_{nk} = \mu\delta_k e^{j2\pi\frac{f_d}{f_t}n}[1 \; e^{j2\pi d\sin\theta/\lambda} \cdots e^{j2\pi d\sin\theta(M-1)/\lambda}]^T$$

$$= \mu g_k(n)\mathbf{t}(\theta). \tag{4.33}$$

Table 4.1: Target Parameters

SNR (dB)	f_d/f_t	$d\sin\theta/\lambda$
0.0	0.09	-0.13

In (4.33) μ, f_d, d, and λ correspond to target amplitude, Doppler frequency, receiver element spacing, and wavelength. The source waveform $g_k(n)$ is coherent with the radar pulse sequence so the covariance of $\mathbf{t}_{nk}$ is,

$$\mathcal{E}\left\{\mathbf{t}_{n'k'}\mathbf{t}_{nk}^H\right\} = \delta_{kk'}\mu^2 e^{j2\pi\frac{f_d}{f_t}(n'-n)}\mathbf{t}(\theta)\mathbf{t}^H(\theta). \tag{4.34}$$

Simulation target parameters are listed in Table 4.1.

4.3.3 Interference

We model $\mathbf{i}_{nk}$ using a first order Generalized Watterson Model (GWM) so that,

$$\mathbf{i}_{nk} = \sum_{m=0}^{N_m} A_m g_k(n)\mathbf{c}_m(n), \tag{4.35}$$

where A_m is the RMS amplitude, $g_k(n)$ is the source waveform, and $\mathbf{c}_m(n)$ is the channel response vector of the mth mode [Abramovicht et al., 1996]. The channel response vector is defined by the scalar MVAR recursion,

$$\mathbf{c}_m(n) = z_m\mathbf{c}_m(n-1) + \sqrt{1 - |z_m|^2}\boldsymbol{\xi}_m(n), \tag{4.36}$$

where the driving noise process $\boldsymbol{\xi}_m(n)$ has the covariance property,

76

$$\mathcal{E}\{\boldsymbol{\xi}_m(n')\boldsymbol{\xi}_m^H(n)\} = \delta_{nn'}\text{Toep}[1\ w_m \cdots w_m^{M-1}]$$

$$= \delta_{nn'}R^{\xi_m\xi_m}. \tag{4.37}$$

Note Toep[·] denotes a *Toeplitz* matrix structure [*Marple*, 1986, Ch. 3, pp. 64]. In addition to having a Toeplitz structure, $R^{\xi_m\xi_m}$ in (4.37) is Hermittian positive definite and and therefore has a Cholesky decomposition $R^{\xi_m\xi_m} = L_c L_c^H$ where L_c is a lower triangular matrix [*Marple*, 1986, Ch. 3, pp. 73] Note that $\boldsymbol{\xi}_m(n)$ may be generated as,

$$\boldsymbol{\xi}_m(n) = L_c\mathbf{n}_{nk}, \tag{4.38}$$

where $\mathbf{n}_{nk}$ is multivariate white noise described previously. Given $\boldsymbol{\xi}_m(n)$, the channel response vector $\mathbf{c}_m(n)$ is found using the vector recursion in (4.36). In (4.36)-(4.37) the parameters (z_m, w_m) are temporal and spatial poles defined in terms of mean (f_m, θ_m) and spread $(B_t(m), B_s(m))$ parameters as,

$$z_m = e^{-B_t(m)/f_t + j2\pi f_m}$$

$$w_m = e^{-B_s(m)|1-\sin\theta_m|d + j2\pi d\sin\theta_m/\lambda}. \tag{4.39}$$

We assume for simplicity that the interference is incoherent and consists of a single mode $(N_m = 1)$. The covariance of $\mathbf{i}_{nk}$ is given by,

$$\mathcal{E}\{\mathbf{i}_{n'k'}\mathbf{i}_{nk}\} = \mathcal{E}\{g_{k'}(n')g_k^*(n)\}\cdot$$

$$\sum_{m=0}^{N_m} A_m^2 \mathcal{E}\{\mathbf{c}_m(n')\mathbf{c}_m^H(n)\}$$

$$= \delta_{nn'}\delta_{kk'}A^2 z^j R^{\xi\xi}. \tag{4.40}$$

77

Table 4.2: Interference Parameters

Mode	INR (dB)	z	w	f_m	$d\sin\theta_m/\lambda$
1	30.0	$0.98e^{j0.6}$	$0.98e^{j0.9}$	-0.1	0.14

The parameters used in simulation are listed in Table 4.2. The mean and spread parameters in Table 4.2 are chosen to place the RFI in the sidelobe of the radar and yield a situation where a constrained SAP algorithm such as TV-SAP or MV-SAP provides discernible spectral sharpening over unconstrained SAP as will be illustrated in Section 4.5.

4.3.4 Coupled Clutter

Angle-Doppler coupled clutter can be generated using the recursion in (4.3). The coefficient matrices $\mathbf{A}_l$ and driving noise spatial covariance $R^{\xi\xi}$ are related to the clutter covariance sequence $\mathbf{R}_j^{yy}$ by the multichannel Yule-Walker equation [*Marple*, 1986, Ch. 15, pp. 394-400],

$$\underline{\mathbf{A}}\,\underline{\mathbf{R}} = \left(R^{\xi\xi}\ 0\cdots 0 \right), \tag{4.41}$$

where the terms in (4.41) are defined by,

$$\underline{\mathbf{A}} = \left[\mathbf{I}\ \mathbf{A}_1\ \cdots \mathbf{A}_P \right]$$

$$\underline{\mathbf{R}} = \begin{pmatrix} \mathbf{R}_0^{yy} & \mathbf{R}_1^{yy} & \cdots & \mathbf{R}_p^{yy} \\ \mathbf{R}_{-1}^{yy} & \mathbf{R}_0^{yy} & \cdots & \mathbf{R}_{p-1}^{yy} \\ \vdots & \vdots & \ddots & \vdots \\ \mathbf{R}_{-p}^{yy} & \mathbf{R}_{-p+1}^{yy} & \cdots & \mathbf{R}_0^{yy} \end{pmatrix}. \tag{4.42}$$

In [*Theurer and Bristow*, 2017] high-latitude clutter was observed that exhibits a Gaussian space-time correlation function of the form,

Table 4.3: Clutter Parameters

A	B	C	D	E	F
7.90×10^{-2}	2.45×10^{-2}	7.60×10^{-3}	1.15	0.0	3.45

$$r(i,j) = e^{Ai^2 + Bij + Cj^2 + Di + Ej + F}, \tag{4.43}$$

where indices (i,j) denote space and time lag. The relationship between (4.43) and the covariance matrices $\mathbf{R}_j^{yy}$ in (4.42) is,

$$\mathbf{R}_j^{yy} = \begin{pmatrix} r(0,j) & \cdots & r(-(M-1),j) \\ \vdots & \ddots & \vdots \\ r(M-1,j) & \cdots & r(0,j) \end{pmatrix}. \tag{4.44}$$

Simulated clutter is generated by,

1. Evaluate (4.43) for a particular set of parameters $[A - F]$

2. Evaluate $(\mathbf{A}_l, R^{\xi\xi})$ from (4.41) for some model order P

3. Evaluate the recursion in (4.3) for the desired number of slow-time samples

There exist methods for determining the model order P that best fits an observed MVAR process based on information theory [*Nuttall*, 1976]. However, the motivation here is to demonstrate the general impact of angle-Doppler coupling on SAP for which a very accurate fit to any particular function is unnecessary. Table 4.3 lists the parameters $[A - F]$ of the coupled clutter space-time correlation function in (4.43) that were used in simulation. The parameter F corresponds to a single element clutter-to-noise ratio of 15 decibels given unit variance noise.

Table 4.4: Radar Operating Parameters

d (m)	λ (m)	θ_s	f_t (Hz)	M	N	K	Q
15.0	30.0	0.0	50.0	16	8192	17	16

4.3.5   Radar Parameters

Table 4.4 contains the relevant radar operating parameters and data dimensions used in simulation. Note θ_s is the steer direction of the radar, i.e. all SAP algorithms are applied with the constraint $\mathbf{w}^H\mathbf{t}(\theta_s) = 1$. There is no significance to the chosen steering direction other than the RFI and target appear in the sidelobes which is the scenario of interest in this paper. Recall that $M \times N \times K$ represents the dimensions of the data cube over the observation period with the axes representing antenna elements, slow-time samples, and range bins respectively. In general, $K = f_r/f_t$ is much greater than the $K = 17$ range gates considered here. However, the purpose of this paper is to evaluate the proposed MV-SAP algorithm using an example of coupled clutter based on measurements made by the high-latitude OTHR in [*Theurer and Bristow*, 2017]. In this case, it is only necessary to simulate a number of range gates containing only interference and noise that is sufficient for estimating the interference covariance matrix and a single range gate that additionally contains the coupled clutter signal and possibly a sidelobe target. In sky wave OTHR systems the range gates closest to the radar contain only thermal noise and RFI as the slant ranges correspond to echoes from volumes of space that lie below the ionosphere and so are free of auroral and ground clutter. In this simulation, the first 16 range bins contain only RFI and noise and so are used to estimate the interference covariance matrix while the last range bin additionally contains the clutter signal. The parameter Q represents the slow-time subinterval window length we use for all SAP algorithms. Note that the total aperture length here is $dM = 240.0$ meters which corresponds to an (untapered) beam width on the order of $\sim 7°$. In addition, note that $N = 8192$ slow-time samples corresponds to a total observation period of $T = N/f_t = 163.84$ seconds. However, when evaluating the Doppler

power spectrum we will divide the scalar output sequence into 256 point windows. This will provide $8192/256 = 32$ samples for each frequency bin so that the mean of the distribution provides a reasonable indicator of average performance for a CPI consisting of 256 pulses which equates to an observation time of $T = 5.12$ seconds. Finally, it is assumed that the receive array is well-calibrated and the problem of array calibration will not be considered here.

4.4   Verification of Coupled Clutter Properties

The effectiveness of MV-SAP is predicated on the existence of $L \ll M$ left singular vectors that span the clutter covariance columnspace $\mathcal{C}\left(\mathbf{R}_m^{yy}\right)$ for all m. In this section, the validity of this assumption is demonstrated for the simulated coupled clutter discussed in Section 4.3.4. The matrices $(\mathbf{A}_l, R^{\xi\xi})$ of an order $P = 4$ MVAR process evaluated from (4.41) were used to generate samples of the mock clutter process. Fig. 4.1 illustrates a comparison of the ideal $|r(i,j)|$ contours and the contours produced from the sample correlation function of $N = 8192$ simulated slow-time snapshots. Fig. 4.1 clearly demonstrates that the MVAR data exhibits the desired rotated elliptical contours in the space-time plane. Fig. 4.2 illustrates the spectrum of $\mathbf{P}_{00}^{yy}(f)$ evaluated using (4.9). Note that all significant frequency components lie within the normalized frequency range $[-0.1, 0.1]$, a feature shared by all components of $\mathbf{P}^{yy}$.

(a) $|r(i,j)|$ of ideal Gaussian using parameters in Table 4.3

(b) $|r(i,j)|$ of a fitted MVAR process of order $P = 4$
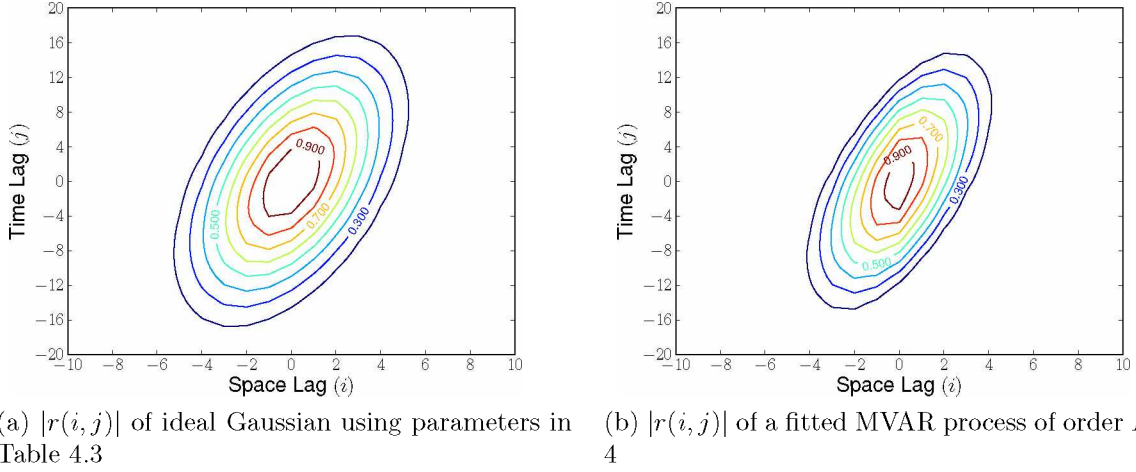
Figure 4.1: Comparison of $|r(i,j)|$ of the simulated MVAR process with the ideal Gaussian function. $|r(i,j)|$ normalized such that $|r(0,0)| = 1.0$.
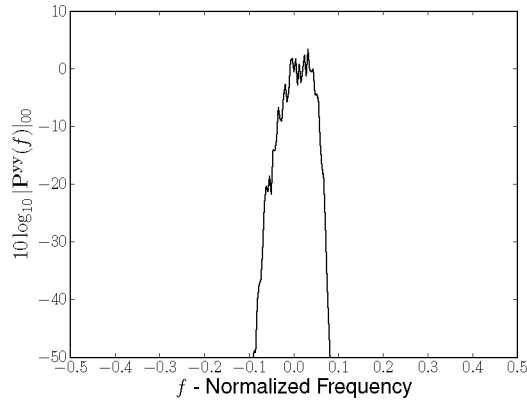
Figure 4.2: Autospectra of coupled clutter used in simulation.

First we verify that $\mathbf{P^{yy}}(f)$ is low rank and has the property that $\mathcal{C}\{\mathbf{P^{yy}}(f_1)\} \neq \mathcal{C}\{\mathbf{P^{yy}}(f_2)\}$ The normalized singular value spectrum of $\mathbf{P^{yy}}(f)$ for $f \in [-0.1, 0.1]$ is depicted in Fig. 4.3a using percentile curves. The percentile curves indicate the value below which a given percentage of singular values may be found. From examining the median percentile curve in Fig. 4.3a, one can see that $\mathbf{P^{yy}}(f)$ is close to unit rank as there is a nearly 50 decibel difference between the first and second singular values. In Fig. 4.3b we've evaluated the projection error magnitude $\|\mathbf{e_{u_f}}\|$ where $\mathbf{e_{u_f}}$ is given by,

$$\mathbf{e}_{\mathbf{u}_f} = \mathbf{u}_f - (\mathbf{u}_0^H \mathbf{u}_f)\mathbf{u}_0. \tag{4.45}$$

In (4.45) $\mathbf{u}_0$ is the largest left singular vector of $\mathbf{P^{yy}}(0)$ while $\mathbf{u}_f$ is the largest left singular vector of $\mathbf{P^{yy}}(f)$. As expected, Fig. 4.3b demonstrates that the left singular vectors of $\mathbf{P^{yy}}(f)$ are generally not parallel for $f_1 \neq f_2$.
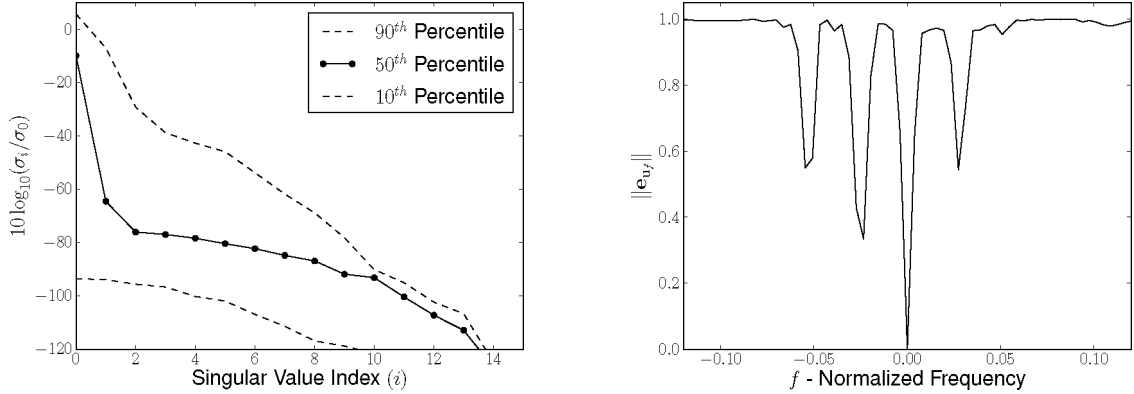
(a) Normalized singular value spectrum of $\mathbf{P^{yy}}(f)$ for $f \in (-0.1, 0.1)$. Normalization factor is largest singular value of $\mathbf{P^{yy}}(0)$.

(b) Error in projection of largest left singular vector of $\mathbf{P^{yy}}(f)$ onto largest left singular vector of $\mathbf{P^{yy}}(0)$.

Figure 4.3: Investigation of the rank and columnspace of $\mathbf{P^{yy}}(f)$.

Next we verify the properties of coupled clutter in the time domain. The normalized singular value spectrum of $\mathbf{R}_m^{\mathbf{yy}}$ for $m \in [0, 128]$ is depicted in Fig. 4.4a. Fig. 4.4a features a much more gradual decay than Fig. 4.3a. While there is no discernible "knee" in Fig. 4.4a, there are $L = 5$ singular values above -12 decibels and thus the singular vectors associated with these values account for $\sim 94\%$ of each matrix $\mathbf{R}_m^{\mathbf{yy}}$. Let $\hat{\mathbf{U}}_m = [\mathbf{u}_0 \cdots \mathbf{u}_4]$ denote the collection of $L = 5$ dominant left singular vectors for each lag m. The projection matrix $\mathbf{U_p}$ given by,

$$\mathbf{U_p} = \hat{\mathbf{U}}_0 \big(\hat{\mathbf{U}}_0^H \hat{\mathbf{U}}_0\big)^{-1} \hat{\mathbf{U}}_0^H, \tag{4.46}$$

yields the least-squares approximation of an arbitrary $M \times 1$ vector in the columnspace of

$\hat{\mathbf{U}}_0$. The error in the least-squares approximation of the left singular vector $\mathbf{u}_m$ of $\mathbf{R}_m^{\mathbf{yy}}$ is then,

$$\mathbf{e}_{\mathbf{u}_m} = \mathbf{u}_m - \mathbf{U}_{\mathbf{p}}\mathbf{u}_m. \tag{4.47}$$

Fig. 4.4b illustrates $\|\mathbf{e}_{\mathbf{u}_m}\|$ for the $L = 6$ largest left singular vectors of $\mathbf{R}_m^{\mathbf{yy}}$ for $m \in [0, 128]$. Fig. 4.4c depicts the relative power σ_i/σ_0 of each associated singular value. It is evident that the columnspace of $\hat{\mathbf{U}}_0$ spans $\hat{\mathbf{U}}_m$ to a good approximation as the occurrence of significant error magnitude in Fig. 4.4b always corresponds to negligible relative power in Fig. 4.4c. Thus the simulated coupled clutter based on the parameters in Table 4.3 satisfies the conditions necessary for MV-SAP to be effective.
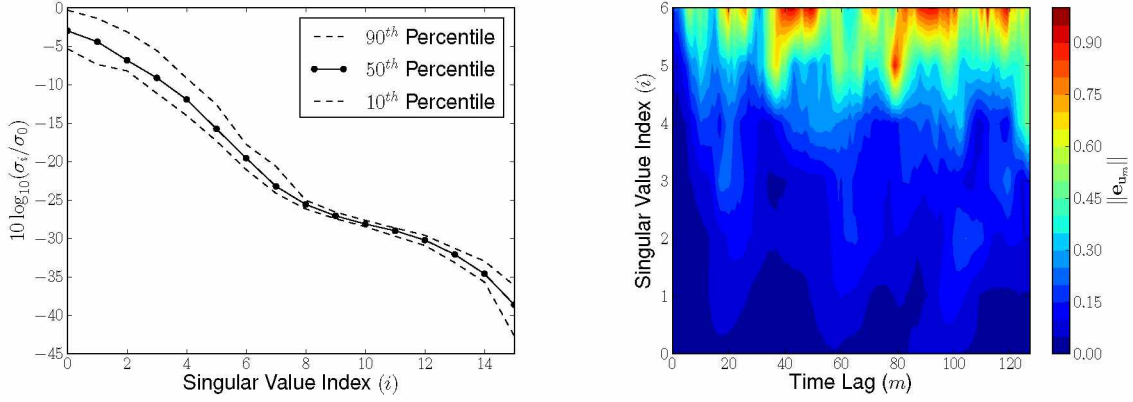
(a) Normalized singular value spectrum of $\mathbf{R}_m^{\mathbf{yy}}$. Normalization factor is largest singular value of $\mathbf{R}_0^{\mathbf{yy}}$.

(b) $\|\mathbf{e}_{\mathbf{u}_m}\|$ for $L = 6$ largest left singular vectors of $\mathbf{R}_m^{\mathbf{yy}}$.
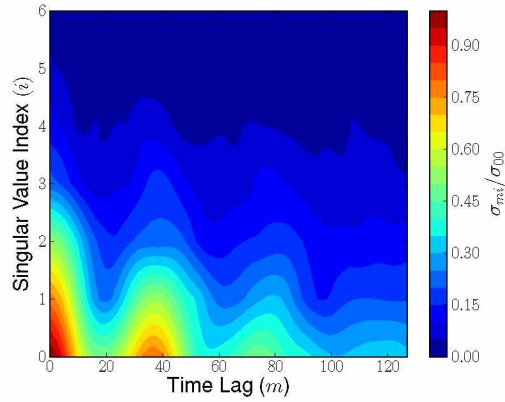
(c) Relative power σ_i/σ_0 corresponding to each left singular vector in (b).

Figure 4.4: Investigation of the columnspace and relative power of $\hat{\mathbf{U}}_m$.

4.5   Results

The performance of the TV-SAP and MV-SAP algorithms are quantified here by applying each technique to the simulated vector sequence $\mathbf{z}_{nk}$ that contains noise, clutter, and RFI to yield the scalar sequence $z[n]$. The focus of this paper is evaluating how well a given SAP algorithm preserves the Doppler spectrum of angle-Doppler coupled clutter for either subsequent Doppler processing or parameter estimation. Doppler power spectra are produced by dividing the scalar output sequence $z[n]$ into 256 point windows, evaluating the

Fast-Fourier-Transform of each window, and averaging the magnitude squared output of all windows. Let $Z_{ideal}[k]$ denote the ideal discrete clutter Doppler power spectrum obtained in the absence of RFI after spatial processing with a fixed weight vector where $k \in [0, 255]$. A measure of how well the SAP algorithm in question preserves $Z_{ideal}[k]$ is a fitting-accuracy (FA) given by,

$$\text{FA} = 1.0 - \frac{\sum_k |Z_{ideal}[k] - Z_{SAP}[k]|^2}{\sum_k Z_{ideal}^2[k]}, \tag{4.48}$$

where $Z_{SAP}[k]$ is the Doppler spectrum produced by MV/TV-SAP. The FA metric will be evaluated both over the entire normalized spectrum $f \in [-0.5, 0.5]$ ($k \in [0, 255]$) and over the smaller clutter region $f \in [-0.1, 0.1]$ ($k \in [102, 154]$) which contains all of the clutter energy. Comparing FA metrics evaluated over these two different regions will help identify tradeoffs between interference suppression and accuracy for each SAP algorithm. In this section we first illustrate a baseline Doppler spectrum that illustrates the Doppler masking produced by RFI as well as the Doppler smearing produced by applying unconstrained SAP. Next, the Doppler spectra and FA metrics of TV-SAP and MV-SAP are compared for a variety of constraints. In addition, we compare the robustness of TV-SAP and MV-SAP in the presence of a sidelobe target. Finally, to support the statistical relevance of the results in this section we illustrate the convergence of the Doppler spectrum as a function the number of windows included in the averaging process.

4.5.1   Baseline Performance

Fig. 4.5 illustrates three different Doppler spectrums that provide a baseline for our investigation. The red curve in Fig. 4.5 illustrates the power spectrum obtained from geometric beamforming with no interference suppression. The blue curve illustrates the power spectrum obtained by applying unconstrained SAP (NSC-SAP) which contains no provisions to prevent Doppler smearing. The black curve illustrates $Z_{ideal}[k]$ in (4.48), i.e. the uncontaminated Doppler spectrum obtained from processing the entire observation period

86

with the first weight vector in the NSC-SAP weight vector sequence. Note that in the ideal case the clutter is confined to the region $f \in [-0.1, 0.1]$ and the sidelobe target is visible as an impulse at $f = 0.09$. Fig. 4.5 illustrates that the interference masks all signals with SNR < 15 dB across the spectrum despite lying well outside the main lobe. Further, NSC-SAP significantly smears the ideal clutter signature across the spectrum so that the sidelobe target is no longer resolvable. The FA metric of NSC-SAP is 87.6% in the clutter region ($f \in [-0.1, 0.1]$) and 61.8% over the full spectrum.
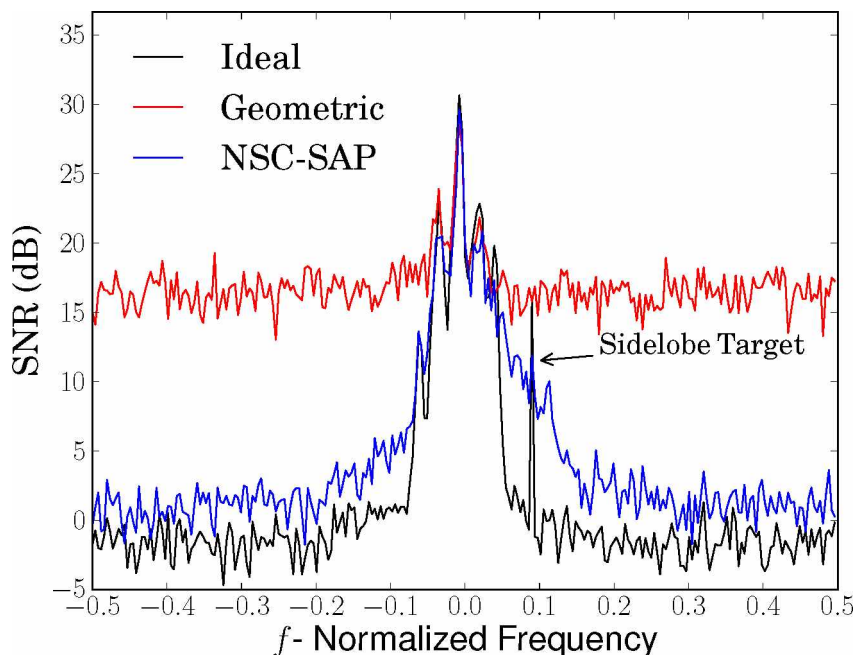
Figure 4.5: Baseline Doppler power spectrum including (i) No interference suppression, geometric beamforming, (ii) Unconstrained SAP (NSC-SAP), and (iii) Ideal (uncontaminated) clutter spectrum obtained by processing entire observation period with first weight vector in unconstrained SAP weight vector sequence.

4.5.2 TV-SAP

Fig. 4.6 contrasts the clutter Doppler spectra produced by TV-SAP with $L = 1$ (red curve) and $L = 3$ (blue curve) constraints with the ideal clutter spectrum. Note that there is no visible spectrum sharpening produced by the increased number of constraints. Table

4.5 depicts the FA metric of TV-SAP vs. number of constraints L for both the clutter region and full spectrum. In both cases the FA metric is relatively insensitive to the number of constraints with an increase of $1\% - 2\%$ between $L = 1, 3$ and a subsequent decrease. These results confirm that with respect to coupled clutter TV-SAP has a performance ceiling due to the error spreading effect discussed in Section 4.2.3 which cannot be overcome by increasing the number of constraints. Instead, it appears that increasing the number of constraints past $L = 2 - 3$ reduces interference suppression and consequently reduces the FA metric. In comparison to NSC-SAP, TV-SAP ($L = 3$) improves the FA metric by 5.4% in the clutter region and by 21.0% over the full spectrum.

Figure 4.6: Ideal and TV-SAP clutter Doppler spectra.

4.5.3 Clairvoyant MV-SAP

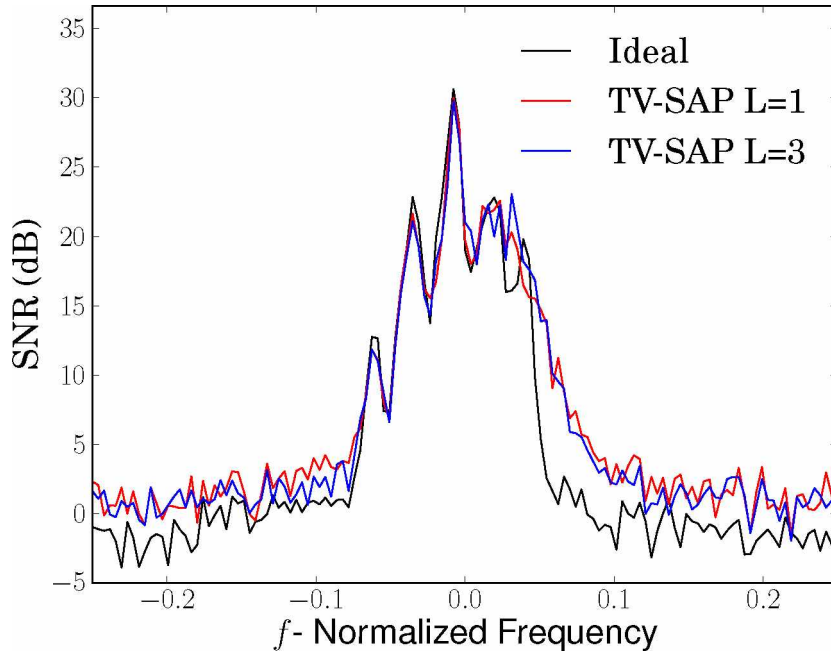As a proof of concept, we first apply the MV-SAP algorithm with clairvoyant knowledge of the left singular vectors of $\mathbf{R}_0^{\mathbf{yy}}$. Specifically, we estimate $\mathbf{R}_0^{\mathbf{yy}}$ using only the simulated ground clutter sequence $\mathbf{y}_{nk}$ uncontaminated by interference. Fig. 4.7 illustrates a compar-

Table 4.5: FA % vs. L for TV-SAP

L	$f \in [-0.1, 0.1]$	$f \in [-0.5, 0.5]$
1	92.5	80.7
2	92.7	82.5
3	93.0	82.8
4	92.9	82.3
5	92.3	80.8

ison of the ideal, TV-SAP, and MV-SAP spectrums. Note $L = 5$ left singular vectors were used to produce the MV-SAP spectrum in accordance with our estimate of the number of significant singular values in Section 4.4. In the clutter region the MV-SAP spectrum is nearly indistinguishable from the ideal spectrum and clearly outperforms TV-SAP. Table 4.6 lists the MV-SAP FA metric versus number of constraints L for both the clutter region and the full spectrum. As expected from our previous analysis, the MV-SAP FA metric is proportional to the number of left singular vectors used as constraints. At the proposed $L = 5$ constraints based on the singular value analysis, MV-SAP provides an increase in the FA metric over NSC-SAP of 11.0% in the clutter region and 24.3% over the full spectrum. MV-SAP begins to outperform TV-SAP ($L = 3$) in the clutter region starting with $L = 2$ constraints and over the whole spectrum starting with $L = 3$ constraints. While MV-SAP provides nearly twice the improvement of TV-SAP in the clutter region there is a relatively small improvement when considering the entire spectrum. Although difficult to discern in Fig. 4.7, in the unoccupied portion of the spectrum MV-SAP appears to have larger amplitude fluctuations or ripple which is responsible for the reduction in the FA metric improvement. Thus, while MV-SAP clearly improves the accuracy of the clutter Doppler signature it does so at the expense of introducing a slight ripple in the unoccupied portion of the spectrum.

Table 4.6: FA % vs. L for Clairvoyant MV-SAP

L	$f \in [-0.1, 0.1]$	$f \in [-0.5, 0.5]$
1	91.2	75.7
2	93.8	80.4
3	95.9	83.2
4	97.9	85.7
5	98.6	86.1
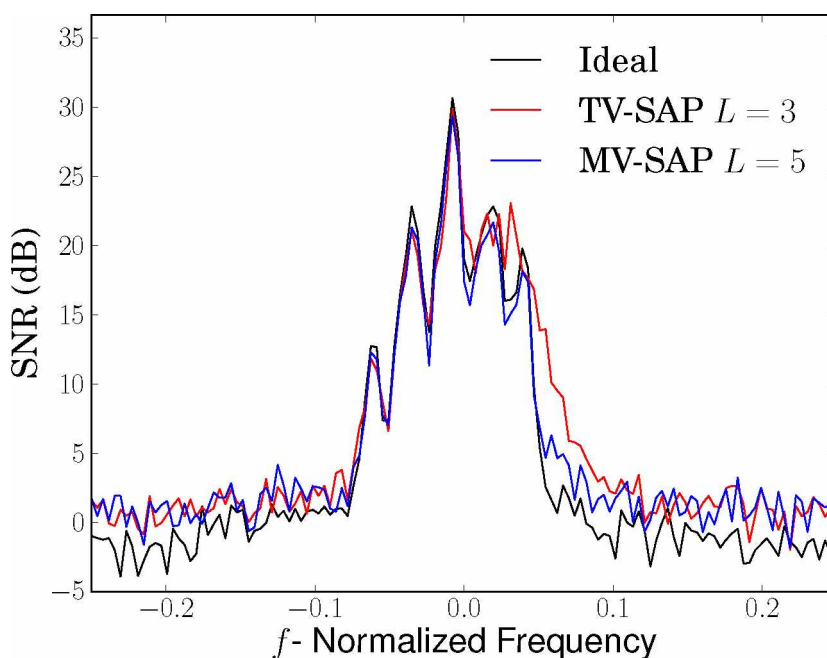
Figure 4.7: Ideal, TV-SAP, and clairvoyant MV-SAP clutter Doppler spectra.

4.5.4   MV-SAP Practical Implementation

Now we analyze the performance of MV-SAP in the event uncontaminated clutter is unavailable for estimating $\mathbf{R}_0^{\mathbf{yy}}$. One method of obtaining clutter only samples over an interval of time is to estimate the interference steering vectors using MUSIC and subtract the projection of the received signal onto the interference subspace as discussed in Section 4.2.4. In the application of MUSIC we assume here that the interference is unit rank in

each subinterval and specifically apply the Root-MUSIC algorithm [*Krim and Viberg*, 1996]. Following the procedure outlined in Section 4.2.4 we use both $N_Q = [2,8]$ CPI subintervals as a training period for estimating $\mathbf{R}_0^{\mathbf{yy}}$. Fig. 4.8 illustrates a comparison of the ideal, TV-SAP ($L = 3$), and MV-SAP ($L = 5$) spectra for $N_Q = 8$. Table 4.7 depicts the FA metric evaluated for $N_Q = [2,8]$ and $L = [1,5]$ over both spectrum regions of interest. In all cases except one ($N_Q = 8$, $L = 2$) FA performance increases with the number of constraints. However, it can be seen that increasing the training period often decreases the FA metric. These results indicate that performance is primarily limited by our ability to accurately measure the left singular vectors of $\mathbf{R}_0^{\mathbf{yy}}$ which in turn depends on the ability to obtain accurate interference steering vectors. The practical MV-SAP implementation with $N_Q = 8$, $L = 5$ yields a 5.2% and 16% increase over NSC-SAP in the clutter region and full spectrum respectively. Thus, the FA metric is essentially the same as TV-SAP ($L = 3$) in the clutter region but 5.0% worse when the entire spectrum is considered. There are two likely culprits for the performance decrease. The first is the incomplete rejection of interference when generating clutter only snapshots. If some amount of interference remains in the snapshots used to evaluate $\mathbf{R}_0^{\mathbf{yy}}$ then interference suppression will be hampered and the clutter spectrum will be skewed. The second culprit is the previously mentioned ripple introduced by MV-SAP in the unoccupied portion of the spectrum.

Table 4.7: FA % vs. L for Practical MV-SAP

L	$N_Q = 2\ f \in [-0.1, 0.1]$	$N_Q = 2\ f \in [-0.5, 0.5]$	$N_Q = 8\ f \in [-0.1, 0.1]$	$N_Q = 8\ f \in [-0.5, 0.5]$
1	86.2	67.2	87.0	67.6
2	87.7	69.6	86.8	66.9
3	89.5	72.8	88.4	69.3
4	90.2	73.6	90.3	74.1
5	92.7	76.7	92.8	77.8
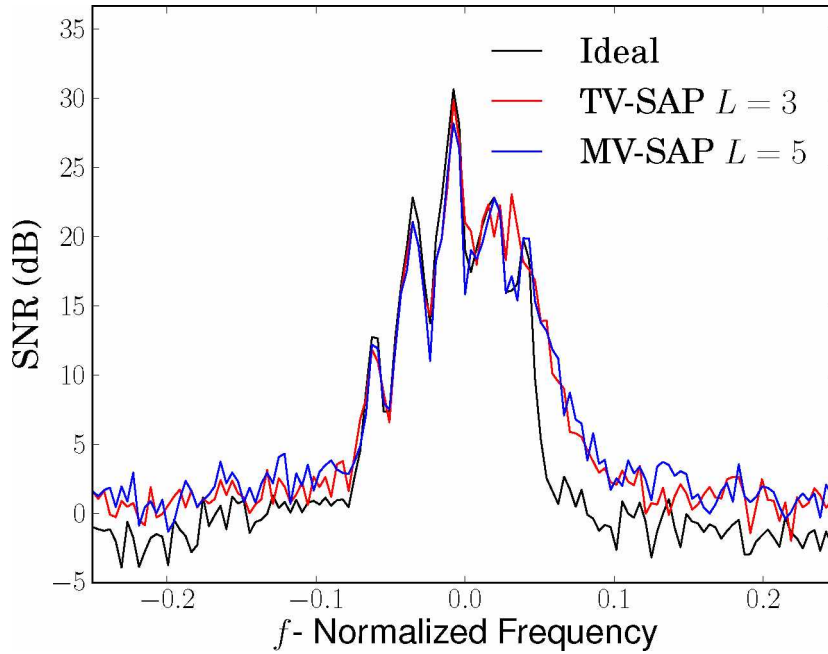
Figure 4.8: Ideal, TV-SAP, and MV-SAP ($N_Q = 8, L = 5$) clutter Doppler spectra.

4.5.5 Sidelobe Target

Finally, we investigate how well TV-SAP and MV-SAP preserve mis-matched or side-lobe targets. Fig. 4.9 illustrates a comparison of ideal, TV-SAP, and MV-SAP (Practical, $N_Q = 8$) Doppler spectra when the range gate being processed includes a sidelobe target with the characteristics listed in Table 4.1. The algorithms are applied with the number of constraints that yielded the best FA from Tables 4.5, 4.7. The FA metrics of TV-SAP and MV-SAP in Fig. 4.9 are 74.3% and 75.8% respectively. The improved FA metric

performance of MV-SAP relative to TV-SAP in this case is due to the enhanced fidelity with which the target Doppler signature is captured. Inspection of Fig. 4.9 illustrates that MV-SAP preserves the impulsive characteristic of the target signal which leads to a ~ 4 dB improvement in SNR over TV-SAP. These results demonstrate that MV-SAP effectively preserves the Doppler signature of incident signals and that although the FA metric used here provides a useful means of quantifying performance it does not give a complete picture of the sharpening afforded by a given SAP algorithm.
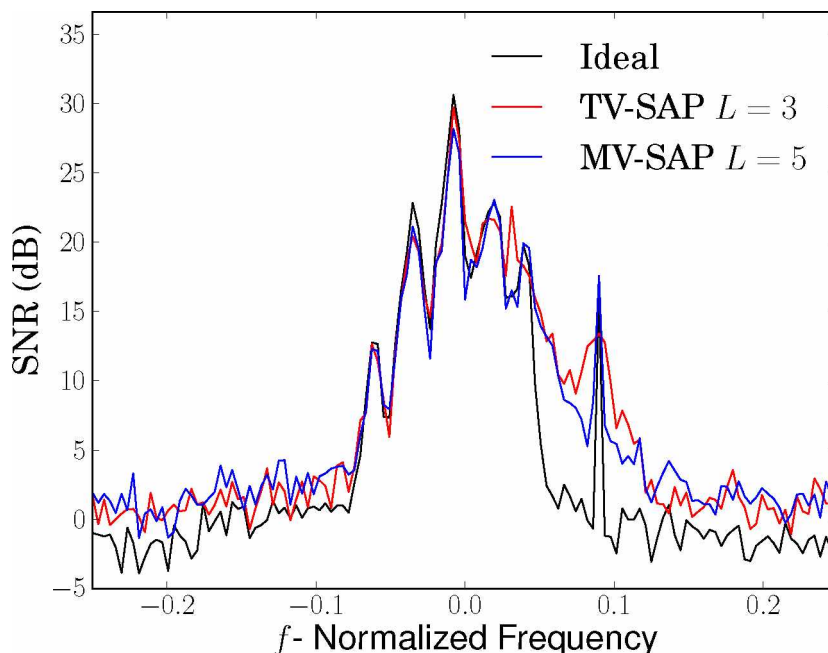
Figure 4.9: TV-SAP ($L = 3$) and MV-SAP ($N_Q = 8$, $L = 5$) Doppler spectra in the presence of a sidelobe target.

4.5.6   Doppler Spectrum Convergence

In section 4.3.5 it was noted that the Doppler spectra presented here are the result of averaging 32 windows of data each of which consist of 256 slow-time snapshots. Let $Z[k]_N$ denote the kth point in the 256 point Doppler spectrum obtained by averaging N windows of data. The difference $Z[k]_N - Z[k]_{N-1}$ should approach zero as the number of windows N increases. Fig. 4.10 depicts the difference $Z[k]_N - Z[k]_{N-1}$ at two points $k = (128, 132)$

within the clutter occupied area of the spectrum as a function of N for both TV-SAP and MV-SAP. Note that by $N \sim 20$ the difference oscillates by only a few tenths of a decibel and so the spectra presented here accurately reflect the true mean of the Doppler spectrum.
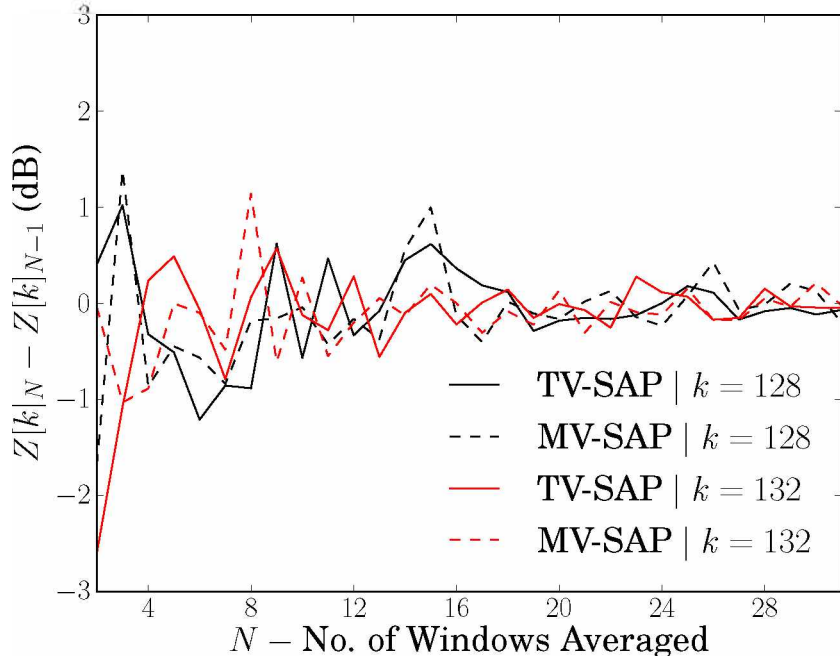
Figure 4.10: Spectrum convergence of TV-SAP ($L = 3$) and MV-SAP ($N_Q = 8, L = 5$) at frequency bins $k = [128, 132]$.

4.6   Summary and Conclusions

In the foregoing analysis, we verified analytically and through simulation that TV-SAP has an intrinsic performance ceiling when applied to coupled clutter. This intrinsic limitation of TV-SAP spurred the development of the alternative algorithm MV-SAP. The results presented demonstrated that the performance of clairvoyant MV-SAP surpasses that of TV-SAP. Specifically, clairvoyant MV-SAP appears to yield an arbitrarily good fit to the clutter Doppler signature at the expense of introducing a slight ripple in the unoccupied portion of the spectrum. The performance of a practical MV-SAP implementation matched that of TV-SAP in the clutter region and was slightly worse when the entire spectrum was considered. However, in the presence of a sidelobe target closely spaced with the clutter signal

in Doppler the practical MV-SAP implementation performed slightly better than TV-SAP. The improved performance relative to TV-SAP in this scenario can be attributed to the increase in target Doppler signature fidelity offsetting the ripple introduced by the algorithm in the unoccupied portion of the Doppler spectrum. Thus, MV-SAP appears to sharpen the Doppler signature of all incident signals present and the FA metric used here provides a useful but incomplete picture of the Doppler visibility enhancement afforded by a given SAP algorithm.

The reduced performance of the practical implementation of MV-SAP in comparison to clairvoyant MV-SAP stems from error in the estimate of $\mathbf{R}_0^{yy}$ due to incomplete rejection of interference when generating clutter only snapshots. As described previously, clutter only snapshots were generated by estimating the interference steering vector using Root-MUSIC and subtracting the projection of the received signal in the interference direction. Root-MUSIC was chosen as the DOA algorithm for its computational efficiency (in comparison to standard MUSIC) and ease of implementation [*Krim and Viberg*, 1996]. A future work will consider other DOA algorithms such as Root-WSF as well as other alterations to the practical implementation in an effort to better approximate the clairvoyant performance [*Krim and Viberg*, 1996]. Another related issue, the problem of array calibration is also deferred to a future work.

It is worth emphasizing that the results presented here are for a specific case of coupled clutter based on measurements made with a high-latitude radar during a particular time and do not represent the performance of TV-SAP and MV-SAP in all cases of angle-Doppler coupling [*Theurer and Bristow*, 2017]. In general, we expect the performance differential between TV-SAP and MV-SAP to be proportional to the amount of angle-Doppler coupling with the difference disappearing in the case of space-time separable clutter. A future work may involve quantifying the performance of MV-SAP as a function of the properties of the coupled clutter such as the major/minor axes lengths and rotation of the correlation function ellipses in the space-time plane. For coupled clutter with properties similar to that

simulated here, TV-SAP provides a reasonably accurate fit to the Doppler spectrum despite the violation of the assumption of clutter space-time separability. However, there may exist conditions in high-latitude OTHR or other signal processing applications where the spectral sharpening of MV-SAP proves to be valuable.

5 Conclusions & Future Work

5.1 Summary

In the previous chapters three different high-frequency (HF) over-the-horizon radar (OTHR) applications were developed for the unique and challenging high-latitude environment. The birefringent, anisotropic, and heterogeneous nature of the ionosphere produce multipath and diffuse scattering effects that invalidate the ordinary assumptions under which radars operate. Specifically, propagation through the ionosphere yields spreading of the target signature in space-time domain or equivalently the angle-Doppler domain. In the angular domain, spreading is observed as a target echo that consists of a narrow angular spectrum of plane waves rather than a single discrete plane wave determined by the geometry between the radar and the target. Similarly, in the Doppler domain spreading is observed as a spectrum of frequencies rather than a discete frequency determined by the velocity of the target with respect to the radar. These propagation effects significantly impact radar performance in a number of different aspects. The most obvious impact is that the angle-Doppler resolution of the radar is diminished by the spreading of energy in these domains during propagation. Another significant consideration is that signal processing techniques require accurate models of the target and interference signals. Thus, signal processing techniques require some form of adaptation to account for ionospheric propagation effects. A final consideration is that the observed propagation effects provide an indirect measurement of the state of the ionosphere which is of importance to the geophysics community.

The first application presented was a method of scintillation correction motivated by an analysis of the detrimental effects that multipath and diffuse scattering have on angular resolution and achievable array gain. The correction method presented coherently combines the spectrum of plane waves produced by ionospheric propagation and was experimentally demonstrated to improve angular resolution by an order of magnitude and increase array gain by ~ 1 decibel.

97

The second application presented here was a method of deriving $\vec{E} \times \vec{B}$ ionospheric drift measurements transverse to the steer direction of the radar. Specifically, the ionosphere was modeled as a random phase screen moving transverse to the radar steer direction and diffraction analysis was used to demonstrate that ground clutter echoes will exhibit angle-Doppler coupling due to the motion of the ionosphere. The measured mutual coherence function of the electric field was used to deduce an effective drift velocity and some experimental measurements were provided.

The final application developed was a new spatial adaptive processing technique termed MV-SAP. The new technique was motivated by the problem of preserving the Doppler spectrum of angle-Doppler coupled clutter in the context of a cascaded processing scheme where SAP is applied to mitigate RFI and Doppler processing is subsequently applied to mitigate clutter. Previously developed SAP algorithms explicitly or implicitly assume space-time separable clutter and the investigation performed here serves to quantify the error involved when that assumption is violated as well as introduce MV-SAP as an alternative. Although MV-SAP was demonstrated to provide approximately twice the spectral sharpening of existing SAP techniques, the practical implementation had a performance ceiling similar to existing methods.

5.2 Future Work

There are a number of improvements that can be made to the work presented here as well as areas of future exploration. With respect to the scintillation correction application a more rigorous analytical analysis could be performed. First, the Cramer-Rao Lower Bound (CRLB) for estimating spatial frequency is derived assuming a plane wave with independent and identically distributed Gaussian phase perturbations at each antenna. A more accurate model that would be consistent with the work performed in Chapter 3 and by other researchers in the area would be to represent the received signal as a multivariate autoregressive (MVAR) process. The probability density function necessary for evaluating the

CRLB is simply related to the spatial covariance matrix and therefore simply related to the MVAR parameters. Performing the CRLB analysis in this manner would provide a better perspective on the improvement in angular resolution afforded by the scintillation correction technique.

With regard to the evaluation of $\vec{E} \times \vec{B}$ drift measurements an alternative derivation of the mutual coherence function of angle-Doppler coupled ground clutter is possible and is included in the Appendix. The advantage of this alternative derivation is that the statistical properties of the random phase screen are explicitly incorporated in the observed mutual coherence function. Further, the alternative derivation hinges on a ground scatter coefficient that is impulsive in angle and thus provides an explanation of why angle-Doppler coupling is not observed as often as one might expect. A future area of exploration would be to assess the relationship between the random screen parameters and the actual scale size of refractive index variations in the ionosphere through some independent method of measurement.

Finally, the practical implementation of MV-SAP requires refinement in order to achieve the theoretical performance of the technique. An obvious method of refinement would be to investigate alternative methods of estimating the interference steering vector during the generation of clutter only samples. Another area of exploration is to assess the performance differential between MV-SAP and existing SAP techniques as a function of the ground clutter properties such as angle-Doppler spectrum widths and the amount of coupling between these domains. An analyis of this nature would be useful for determining under what conditions MV-SAP outperforms existing SAP techniques and how large of a benefit the method provides.

Appendix: Alternative Derivation of Ground Clutter MCF

The derivation of the mutual coherence function (MCF) of angle-Doppler coupled ground clutter in Chapter 3 is based on the assumption that the effects of diffuse scattering can be represented by a random phase screen moving transverse to the steer direction of the radar. However, no assumptions are made about the random phase screen other than that it imparts an angular specific Doppler shift. Here an alternative derivation is provided that explicitly incorporates a detailed description of the random phase screen.

Recall equation (3.15) re-stated below which expresses the electric field across the random phase screen due to backscatter from the ground:

$$E(x) = \int \sigma'(\phi) F_{s_f}(\phi) e^{-jk'x\phi} d\phi \qquad (A.1)$$

Suppose the ground scatter is dominated by a single specular component at angle ϕ_r. The backscatter coefficient $\sigma'(\phi)$ is then $\sigma'(\phi) \simeq \delta(\phi - \phi_r)$, and (A.1) reduces to,

$$E(x) = F_{s_f}(\phi_r) e^{-jk'x\phi_r} \qquad (A.2)$$

In (A.2), note $F_{s_f}(\phi_r)$ is a scalar and recall that $k' = |\vec{k}| \cos\theta_0$ where θ_0 is the elevation angle of the scattered plane wave. Thus, the electric field across the phase screen in (A.2) is that given by a plane wave of amplitude $F_{s_f}(\phi_r)$ and wave vector $\vec{k}$ where $\vec{k} \cdot \hat{x} = |\vec{k}| \cos\theta_0 \sin\phi_r x \sim k'x\phi_r$. Omitted from (A.2) are the $\hat{z}$ and $\hat{y}$ components of the phase term which are $|\vec{k}| \cos\theta_0 \cos\phi_r z \sim k'z$ and $|\vec{k}| \sin\theta_0 y$ respectively where (y, z) are evaluated at the coordinates of the phase screen. These terms are omitted as they are constant across the phase screen and will not contribute to the observed MCF.

If the random screen imparts a phase shift of $k'f(x, t)$ at the point x and time t then

(A.2) can be expressed as,

$$E(x) = F_{s_f}(\phi_r)e^{-jk'x\phi_r}e^{jk'f(x,t)} \tag{A.3}$$

The MCF of the electric field can now be written as,

$$\Gamma(\xi,\tau) = \iint E(x,t)E^*(x+\xi,t+\tau)dxdt$$
$$= |F_{s_f}|^2 e^{jk'\xi\phi_r} \iint e^{-jk'(f(x+\xi,t+\tau)-f(x,t))}dxdt \tag{A.4}$$

The phase difference $f(x+\xi,t+\tau) - f(x,t)$ appearing in the exponential in the integrand is a random quantity whose variations will be assumed to be homogeneous and stationary, i.e. independent of the (x,t) origin. In this case (A.4) is equivalent to,

$$\Gamma(\xi,\tau) = |F_{s_f}|^2 e^{jk'\xi\phi_r} \int e^{-jk'\delta_{\xi,\tau}} p(\delta_{\xi,\tau})d\delta_{\xi,\tau} \tag{A.5}$$

where $\delta_{\xi,\tau} = f(x+\xi,t+\tau) - f(x,t)$ is the random phase displacement and $p(\delta_{\xi,\tau})$ is the probability distribution of $\delta_{\xi,\tau}$. Note that $|F_{s_f}(\phi_r)|^2$ is a scale factor while $e^{jk'\xi\phi_r}$ is the linear phase expected from a wave arriving at the angle ϕ_r. Dropping these terms, the normalized MCF can be expressed solely in terms of the statistical properties of the random screen as,

$$\Gamma(\xi,\tau) = \int e^{-jk'\delta_{\xi,\tau}} p(\delta_{\xi,\tau})d\delta_{\xi,\tau} \tag{A.6}$$

Now the measured ground clutter MCF's in Chapter 3 have elliptical contours which provides a clue as to what form the distribution $p(\delta_{\xi,\tau})$ must have. Let $p(\delta_\xi)$ be the probability density of observing phase difference δ_ξ between two points separated by ξ. Assume that $p(\delta_\xi)$ is a zero mean Gaussian distribution with variance,

$$\sigma_\xi^2 = D_\xi\xi^2 \tag{A.7}$$

so that the variance of the distribution is proportional to the square of the spatial displacement along the screen. Similarly, let $p(\delta_\tau)$ be the probability density of observing phase difference δ_τ at two times separated by τ. Again, let $p(\delta_\tau)$ be normally distributed with a variance σ_τ^2 given by,

$$\sigma_\tau^2 = D_\tau \tau^2 \tag{A.8}$$

The joint probability density function $p(\delta_\xi, \delta_\tau)$ is simply,

$$p(\delta_\xi, \delta_\tau) = \frac{1}{2\pi \sigma_\xi \sigma_\tau \sqrt{1-\rho^2}} e^{\frac{-1}{2(1-\rho^2)}\left(\frac{\delta_\tau^2}{\sigma_\tau^2} + \frac{\delta_\xi^2}{\sigma_\xi^2} - \frac{2\rho\delta_\xi\delta_\tau}{\sigma_\xi\sigma_\tau}\right)} \tag{A.9}$$

where ρ is the correlation between δ_ξ and δ_τ. Note that the correlation ρ captures the motion of the random screen. Namely, in the absence of any motion $\rho = 0$ while values of $\rho > 0$ imply a net velocity along the x-axis. The phase displacement $\delta_{\xi,\tau}$ in (A.6) is $\delta_{\xi,\tau} = \delta_\tau + \delta_\xi$ with a probability distribution given by,

$$p(\delta_{\xi,\tau}) = \frac{1}{\sqrt{2\pi\sigma_{\xi,\tau}^2}} e^{-\frac{1}{2}\left(\frac{\delta_{\xi,\tau}^2}{\sigma_{\xi,\tau}^2}\right)} \tag{A.10}$$

where the variance $\sigma_{\xi,\tau}^2$ is,

$$\sigma_{\xi,\tau}^2 = \sigma_\xi^2 + \sigma_\tau^2 - 2\rho\sigma_\xi\sigma_\tau \tag{A.11}$$

Substituting (A.10) into (A.6) yields the MCF,

$$\begin{aligned}
\Gamma(\xi, \tau) &= e^{-\frac{k'^2}{2}\sigma_{\xi,\tau}^2} \\
&= e^{-\frac{k'^2}{2}\left(\sigma_\xi^2 + \sigma_\tau^2 - 2\rho\sigma_\xi\sigma_\tau\right)} \\
&= e^{-\frac{k'^2}{2}\left(D_\xi\xi^2 + D_\tau\tau^2 - 2\rho\sqrt{D_\xi D_\tau}\tau\xi\right)} \\
&= e^{A\xi^2 + B\xi\tau + C\tau^2} \tag{A.12}
\end{aligned}$$

Note that (A.12) clearly has the desired rotated ellyptical contours in the (ξ, τ) plane and
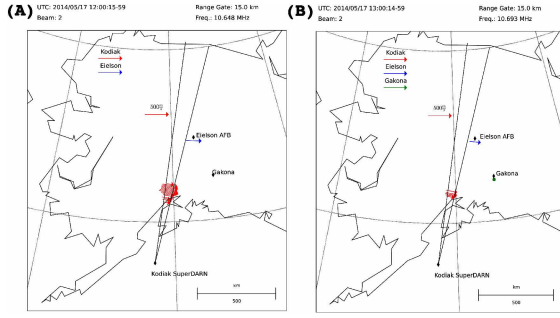
(a) Figure 3.14 depicting ionospheric drift measurements.

(b) Topographic map of Alaska provided by https://pacific-map.com/topographical-map-of-alaska-state.html

Figure A.1: Comparison of Figure 3.14 with topographic map of Alaska demonstrating that regions where significant ionospheric drift was measured correspond roughly to the location of the Alaska Range.

that the quadratic parameters (A, B, C) are simply related to the random screen parameters (D_ξ, D_τ, ρ).

The derivation presented here that culminated in (A.12) was obtained by assuming that backscatter from the ground is dominated by a single specular component. In other words the assumption is that at some particular angle ϕ_r there is a particularly strong return compared to all other angles ϕ in the illuminated area. A particularly strong return could be expected when the surface normal at the ground is parallel to the wave vector so that most of the signal is scattered directly back towards the radar. For typical ground clutter elevation angles θ_0 this requires a surface with a steep slope such as a mountain. Figure (A.1) above depicts a comparison of the ionospheric drift map in Figure 3.14 with a topographic map of Alaska.

Note that areas of significant ionospheric drift velocities in Figure (A.1a) correspond to range cells where significant angle-Doppler coupling was present in the clutter return. Inspection of the topographic map above in Figure (A.1b) demonstrates that the region of significant ionospheric drift velocity corresponds roughly to the location of the Alaska Range in the radar field of view. Thus, the assumption made in the derivation here is consistent with the measurements made in Chapter 3.

References

Abramovich, Y., C. Demeure, and A. Gorokhov (1996), Experimental verification of a generalized multivariate propagation model for ionospheric hf signals, in *1996 8th European Signal Processing Conference (EUSIPCO 1996)*, pp. 1–4.

Abramovich, Y. I., A. Y. Gorokhov, V. N. Mikhaylyukov, and I. P. Malyavin (1994), Exterior noise adaptive rejection for oth radar implementations, in *Proceedings of ICASSP '94. IEEE International Conference on Acoustics, Speech and Signal Processing*, vol. vi, pp. VI/105–VI/107 vol.6, doi:10.1109/ICASSP.1994.389928.

Abramovich, Y. I., N. K. Spencer, S. J. Anderson, and A. Y. Gorokhov (1998), Stochastic-constraints method in nonstationary hot-clutter cancellation. i. fundamentals and supervised training applications, *IEEE Transactions on Aerospace and Electronic Systems*, *34*(4), 1271–1292, doi:10.1109/7.722714.

Attia, E. H., and B. D. Steinberg (1989), Self-cohering large antenna arrays using the spatial correlation properties of radar clutter, *IEEE Transactions on Antennas and Propagation*, *37*(1), 30–38, doi:10.1109/8.192160.

Aubrun, J. ., K. Lorell, T. Mast, and J. Nelson (1987), Dynamic analysis of the activley controlled segmented mirror of the w. m. keck ten-meter telescope, *IEEE Control Systems Magazine*, *7*(6), 3–10, doi:10.1109/MCS.1987.1105386.

Briggs, B. H. (1968), On the analysis of moving patterns in geophysics - i. correlation analysis, *Journal of Atmospheric and Terrestrial Physics*, *30*(10), 1777 – 1788, doi:https://doi.org/10.1016/0021-9169(68)90097-4.

Briggs, B. H., G. J. Phillips, and D. H. Shinn (1950), The analysis of observations on spaced receivers of the fading of radio signals, *Proceedings of the Physical Society. Section B*, *63*(2), 106–121, doi:10.1088/0370-1301/63/2/305.

Bristow, W. A., and R. A. Greenwald (1995), Estimating gravity wave parameters from oblique high-frequency backscatter: Modeling and analysis, *Journal of Geophysical Research: Space Physics*, *100*(A3), 3639–3648, doi:10.1029/94JA02704.

Budden, K. G. (1985), *The Propagation of Radio Waves: The Theory of Radio Waves of Low Power in the Ionosphere and Magnetosphere*, Cambridge University Press, doi: 10.1017/CBO9780511564321.

Carlson, B. A., P. B. Crilly, and J. C. Rutledge (2002), *Communication Systems*, McGraw-Hill.

Choi, D. S., B. Weijers, R. J. Norris, and N. B. Myers (1991), Preliminary analysis of hf auroral backscatter data observed using verona ava linear array radar, in *MILCOM 91 - Conference record*, pp. 233–237 vol.1, doi:10.1109/MILCOM.1991.258242.

Doviak, R. J., R. J. Lataitis, and C. L. Holloway (1996), Cross correlations and cross spectra for spaced antenna wind profilers 1. theoretical analysis, *Radio Science*, *31*(1), 157–180, doi:10.1029/95RS02318.

Fabrizio, G. (2013), *High-Frequency Over-The-Horizon Radar: Fundamental Principles, Signal Processing, and Practical Applications*, McGraw Hill Professional.

Fabrizio, G. A., Y. I. Abramovich, S. J. Anderson, D. A. Gray, and M. D. Turley (1998), Adaptive cancellation of nonstationary interference in hf antenna arrays, *IEE Proceedings - Radar, Sonar and Navigation*, *145*(1), 19–24, doi:10.1049/ip-rsn:19981779.

Fabrizio, G. A., A. B. Gershman, and M. D. Turley (2004), Robust adaptive beamforming for hf surface wave over-the-horizon radar, *IEEE Transactions on Aerospace and Electronic Systems*, *40*(2), 510–525, doi:10.1109/TAES.2004.1310001.

Goodman, J. W. (1985), *Statistical Optics*, John Wiley.

Goodman, J. W. (2005), *Introduction to Fourier Optics*, Roberts and Company.

Greenwald, R. A., K. B. Baker, R. A. Hutchins, and C. Hanuise (1985), An hf phased-array radar for studying small-scale structure in the high-latitude ionosphere, *Radio Science*, *20*(01), 63–79, doi:10.1029/RS020i001p00063.

Holdsworth, D. A. (1999), Spatial correlation analysis revisited: Theory, and application to radar backscatter model data, *Radio Science*, *34*(3), 629–641, doi:10.1029/1998RS900019.

Holloway, C. L., R. J. Doviak, and S. A. Cohn (1997a), Cross correlations of fields scattered by horizontally anisotropic refractive index irregularities, *Radio Science*, *32*(5), 1911–1920, doi:10.1029/97RS00715.

Holloway, C. L., R. J. Doviak, S. A. Cohn, R. J. Lataitis, and J. S. V. Baelen (1997b), Cross correlations and cross spectra for spaced antenna wind profilers: 2. algorithms to estimate wind and turbulence, *Radio Science*, *32*(3), 967–982, doi:10.1029/96RS03885.

Knepp, D. L. (1983), Analytic solution for the two-frequency mutual coherence function for spherical wave propagation, *Radio Science*, *18*(04), 535–549, doi:10.1029/ RS018i004p00535.

Krim, H., and M. Viberg (1996), Two decades of array signal processing research: the parametric approach, *IEEE Signal Processing Magazine*, *13*(4), 67–94, doi:10.1109/79. 526899.

Leong, H. W. H. (1999), Adaptive suppression of skywave interference in hf surface wave radar using auxiliary horizontal dipole antennas, in *1999 IEEE Pacific Rim Conference on Communications, Computers and Signal Processing (PACRIM 1999). Conference Proceedings (Cat. No.99CH36368)*, pp. 128–132, doi:10.1109/PACRIM.1999.799494.

Liang, J., D. R. Williams, and D. T. Miller (1997), Supernormal vision and high-resolution retinal imaging through adaptive optics, *J. Opt. Soc. Am. A*, *14*(11), 2884–2892, doi: 10.1364/JOSAA.14.002884.

Marple, S. L. (1986), *Digital Spectral Analysis: With Applications*, Prentice-Hall, Inc., Upper Saddle River, NJ, USA.

Mitra, S. (2010), *Digital Signal Processing*, McGraw-Hill.

Mitra, S. N. (1949), A radio method of measuring winds in the ionosphere, *Journal of the Institution of Electrical Engineers*, *1949*(11), 277, doi:10.1049/jiee-2.1949.0129.

Ng, G. C., P. D. Freiburger, W. F. Walker, and G. E. Trahey (1997), A speckle target adaptive imaging technique in the presence of distributed aberrations, *IEEE Transactions on Ultrasonics, Ferroelectrics, and Frequency Control*, *44*(1), 140–151, doi:10.1109/58.585209.

Nickisch, L. J. (1992), Non-uniform motion and extended media effects on the mutual coherence function: An analytic solution for spaced frequency, position, and time, *Radio Science*, *27*(01), 9–22, doi:10.1029/91RS02356.

Nickisch, L. J., and P. M. Franke (2001), Finite difference time domain tests of random media propagation theory: 2. signal correlation length and channel bandwidth, *Radio Science*, *36*(2), 371–378, doi:10.1029/1999RS002416.

Nuttall, A. H. (1976), Multivariate linear predictive spectral analysis, employing forward and backward averaging: A generalization of burg's algorithm, *Tech. Rep. 5501*, Naval Underwater Systems Center, New London, Conn.

Papoulis, A. (1984), *Probability, Random Variables, and Stochastic Processes*, McGraw-Hill.

Peebles, P. Z. (1998), *Radar Principles*, John Wiley.

Proakis, G. J., and M. Salehi (2008), *Digital Signal Processing*, McGraw-Hill.

Ratcliffe, J. A. (1956), Some aspects of diffraction theory and their application to the ionosphere, *Reports on Progress in Physics*, *19*(1), 188–267, doi:10.1088/0034-4885/19/1/306.

Ravan, M., and R. S. Adve (2013), Modeling the received signal for the canadian over-the-horizon-radar, in *2013 IEEE Radar Conference (RadarCon13)*, pp. 1–6, doi:10.1109/RADAR.2013.6586093.

Ravan, M., R. S. Adve, and R. J. Riddolls (2011), Mimo fast fully adaptive processing in over-the-horizon radar, in *2011 IEEE RadarCon (RADAR)*, pp. 538–542, doi:10.1109/RADAR.2011.5960595.

Ravan, M., R. J. Riddolls, and R. S. Adve (2012), Ionospheric and auroral clutter models for hf surface wave and over-the-horizon radar systems, *Radio Science*, *47*(3), doi:10.1029/2011RS004944.

Reed, I. S., J. D. Mallett, and L. E. Brennan (1974), Rapid convergence rate in adaptive arrays, *IEEE Transactions on Aerospace and Electronic Systems*, *AES-10*(6), 853–863, doi:10.1109/TAES.1974.307893.

Reinisch, B. W., and I. A. Galkin (2011), Global ionospheric radio observatory (giro), *Earth, Planets and Space*, *63*(4), 377–381, doi:10.5047/eps.2011.03.001.

Riddolls, R. J. (2014), Auroral clutter observations with a three-dimensional over-the-horizon radar, in *2014 IEEE Radar Conference*, pp. 0387–0390, doi:10.1109/RADAR.2014.6875620.

Ruohoniemi, J. M., and K. B. Baker (1998), Large-scale imaging of high-latitude convection with super dual auroral radar network hf radar observations, *Journal of Geophysical Research: Space Physics*, *103*(A9), 20,797–20,811, doi:10.1029/98JA01288.

Saleh, O., M. Ravan, R. Riddolls, and R. Adve (2016), Fast fully adaptive processing: a multistage stap approach, *IEEE Transactions on Aerospace and Electronic Systems*, *52*(5), 2168–2183, doi:10.1109/TAES.2016.150366.

Schmidt, R. (1986), Multiple emitter location and signal parameter estimation, *IEEE Transactions on Antennas and Propagation*, *34*(3), 276–280, doi:10.1109/TAP.1986.1143830.

Shnidman, D. A. (2002), Determination of required snr values [radar detection], *IEEE Transactions on Aerospace and Electronic Systems*, *38*(3), 1059–1064, doi:10.1109/TAES.2002.1039422.

Skolnik, M. I. (2008), *Radar Handbook, Third Edition*, McGraw-Hill Education, New York, NY, USA.

Steinberg, B. (1981), Radar imaging from a distorted array: The radio camera algorithm and experiments, *IEEE Transactions on Antennas and Propagation*, *29*(5), 740–748, doi:10.1109/TAP.1981.1142652.

Stoica, P., and R. Moses (2005), *Spectral Analysis of Signals*, Pearson Prentice Hall, Upper Saddle River, NJ, USA.

Theurer, T. E., and W. A. Bristow (2012), Observations and effects of artificial density layers on oblique high-frequency backscatter, *Radio Science*, *47*(02), 1–14, doi:10.1029/2011RS004861.

Theurer, T. E., and W. A. Bristow (2017), High-frequency radar ground clutter spatial correlation analysis: Transverse ionospheric drift velocity, *Radio Science*, *52*(4), 461–478, doi:10.1002/2016RS006162.

Vallières, X., J.-P. Villain, C. Hanuise, and R. André (2004), Ionospheric propagation effects on spectral widths measured by superdarn hf radars, *Annales Geophysicae*, *22*(6), 2023–2031, doi:10.5194/angeo-22-2023-2004.

Ward, J. (1994), Space-time adaptive processing for airborne radar, *Tech. Rep. F19628-95-C-002*, MIT Lincoln Laboratory.